

JAANA LILLOJA

Transition metal and nitrogen doped
nanocarbon cathode catalysts for anion
exchange membrane fuel cells



DISSERTATIONES CHIMICAE UNIVERSITATIS TARTUENSIS

213

DISSERTATIONES CHIMICAE UNIVERSITATIS TARTUENSIS

213

JAANA LILLOJA

Transition metal and nitrogen doped
nanocarbon cathode catalysts for anion
exchange membrane fuel cells



UNIVERSITY OF TARTU

Press

1632

Institute of Chemistry, Faculty of Science and Technology, University of Tartu,
Estonia

The dissertation is accepted for the commencement of the degree of *Doctor Philosophiae* in Chemistry on June 17th, 2022 by the Council of Institute of Chemistry, Faculty of Science and Technology, University of Tartu.

Supervisors: Prof. Kaido Tammeveski
Institute of Chemistry, University of Tartu, Estonia

PhD Ave Sarapuu
Institute of Chemistry, University of Tartu, Estonia

PhD Elo Kibena-Põldsepp
Institute of Chemistry, University of Tartu, Estonia

Opponent: PhD Juan Herranz
Paul Scherrer Institute, Switzerland

Commencement: August 23rd, 2022 at 14.15, Ravila 14A–1020, Tartu
(Chemicum) and Microsoft Teams (online)

This work has been partially supported by ASTRA project PER ASPERA Graduate School of Functional Materials and Technologies receiving funding from the European Regional Development Fund under project in University of Tartu, Estonia



European Union
European Regional
Development Fund



Investing
in your future

ISSN 1406-0299
ISBN 978-9949-03-961-6 (print)
ISBN 978-9949-03-962-3 (pdf)

Copyright: Jaana Lilloja, 2022

University of Tartu Press
www.tyk.ee

TABLE OF CONTENTS

1. LIST OF ORIGINAL PUBLICATIONS	7
2. ABBREVIATIONS AND SYMBOLS	9
3. INTRODUCTION	11
4. LITERATURE OVERVIEW	12
4.1 Polymer electrolyte membrane fuel cells	12
4.2 Oxygen reduction reaction	14
4.3 Non-precious metal catalysts for oxygen reduction	15
4.3.1 Metal-free electrocatalysts	15
4.3.2 Metal-nitrogen-carbon (M-N-C) catalysts	17
4.4 Carbon nanomaterials	18
4.5 Performance of anion exchange membrane fuel cells	20
5. EXPERIMENTAL	24
5.1 Pretreatment and preparation of carbon nanomaterials	24
5.2 Synthesis of nitrogen and/or transition metal doped nanocarbons ...	25
5.2.1 Nitrogen and/or cobalt doped CDC/CNT composites	25
5.2.2 Transition metal and nitrogen doped graphene/CNT composites	25
5.2.3 Transition metal and nitrogen doped CDC/CNT composites ..	25
5.2.4 Transition metal and nitrogen doped mesoporous carbon	26
5.2.5 Transition metal and nitrogen doped OMC-based materials ...	26
5.3 Physico-chemical characterisation methods	27
5.4 Electrode preparation and electrochemical measurements	28
5.5 Anion exchange membrane fuel cell tests	30
6. RESULTS AND DISCUSSION	33
6.1 Nitrogen and/or cobalt doped CDC/CNT composites as catalysts for oxygen reduction	33
6.1.1 Physico-chemical characterisation of N-CDC/CNT and Co- N-CDC/CNT materials	33
6.1.2 Oxygen reduction reaction on N-CDC/CNT and Co-N- CDC/CNT catalysts	38
6.1.3 Anion exchange membrane fuel cell test with N-CDC/CNT and Co-N-CDC/CNT catalysts	41
6.2 Transition metal and nitrogen doped graphene/CNT composites as catalysts	42
6.2.1 Physico-chemical characterisation of M-N-Gra/CNT materials	42
6.2.2 Oxygen reduction reaction on M-N-Gra/CNT catalysts	45
6.2.3 Anion exchange membrane fuel cell test with M-N-Gra/CNT catalysts	47

6.3	Transition metal and nitrogen doped CDC/CNT composites as catalysts	48
6.3.1	Physico-chemical characterisation of M-N-CDC/CNT materials	48
6.3.2	Oxygen reduction reaction on M-N-CDC/CNT catalysts	51
6.3.3	Anion exchange membrane fuel cell test with M-N-CDC/CNT catalysts	53
6.4	Transition metal and nitrogen doped mesoporous carbons as catalysts	55
6.4.1	Physico-chemical characterisation of M-N-MPC materials	55
6.4.2	Oxygen reduction reaction on M-N-MPC catalysts	60
6.4.3	Anion exchange membrane fuel cell test with M-N-MPC catalysts	62
6.5	Cobalt-, iron- and nitrogen-doped ordered mesoporous carbon-based catalysts	63
6.5.1	Physico-chemical characterisation of OMC-based materials ..	63
6.5.2	Oxygen reduction reaction on OMC-based catalysts	67
6.5.3	Anion exchange membrane fuel cell test with OMC-based catalysts	68
7.	SUMMARY	70
8.	REFERENCES	72
9.	SUMMARY IN ESTONIAN	86
10.	ACKNOWLEDGEMENTS	88
	PUBLICATIONS	89
	CURRICULUM VITAE	188
	ELULOOKIRJELDUS	190

1. LIST OF ORIGINAL PUBLICATIONS

This thesis consists of six original articles listed below. The articles are referred in the text by Roman numerals I–VI.

- I **J. Lilloja**, E. Kibena-Pöldsepp, A. Sarapuu, A. Kikas, V. Kisand, M. Käärik, M. Merisalu, A. Treshchalov, J. Leis, V. Sammelselg, Q. Wei, S. Holdcroft, K. Tammeveski, Nitrogen-doped carbide-derived carbon/carbon nanotube composites as cathode catalysts for anion exchange membrane fuel cell application, *Applied Catalysis B: Environmental* 272 (2020) 119012.
- II **J. Lilloja**, E. Kibena-Pöldsepp, A. Sarapuu, M. Kodali, Y. Chen, T. Asset, M. Käärik, M. Merisalu, P. Paiste, J. Aruväli, A. Treshchalov, M. Rähn, J. Leis, V. Sammelselg, S. Holdcroft, P. Atanassov, K. Tammeveski, Cathode catalysts based on cobalt- and nitrogen-doped nanocarbon composites for anion exchange membrane fuel cells, *ACS Applied Energy Materials* 3 (2020) 5375–5384.
- III **J. Lilloja**, E. Kibena-Pöldsepp, A. Sarapuu, A. Konovalova, M. Käärik, J. Kozlova, P. Paiste, A. Kikas, A. Treshchalov, J. Aruväli, J. Leis, A. Tamm, V. Kisand, S. Holdcroft, K. Tammeveski, Transition metal and nitrogen-doped carbon nanotube/graphene composites as cathode catalysts for anion-exchange membrane fuel cells (manuscript).
- IV **J. Lilloja**, E. Kibena-Pöldsepp, A. Sarapuu, J. C. Douglin, M. Käärik, J. Kozlova, P. Paiste, A. Kikas, J. Aruväli, J. Leis, V. Sammelselg, D.R. Dekel, K. Tammeveski, Transition-Metal- and nitrogen-doped carbide-derived carbon/carbon nanotube composites as cathode catalysts for anion-exchange membrane fuel cells, *ACS Catalysis* 11 (2021) 1920–1931.
- V **J. Lilloja**, E. Kibena-Pöldsepp, A. Sarapuu, M. Käärik, J. Kozlova, P. Paiste, A. Kikas, A. Treshchalov, J. Leis, A. Tamm, V. Kisand, S. Holdcroft, K. Tammeveski, Transition metal and nitrogen-doped mesoporous carbons as cathode catalysts for anion-exchange membrane fuel cells, *Applied Catalysis B: Environmental* 306 (2022) 121113.
- VI **J. Lilloja**, M. Mooste, E. Kibena-Pöldsepp, A. Sarapuu, A. Kikas, V. Kisand, M. Käärik, J. Kozlova, A. Treshchalov, P. Paiste, J. Leis, A. Tamm, S. Holdcroft, K. Tammeveski, Cobalt-, iron- and nitrogen-containing ordered mesoporous carbon-based catalysts for anion-exchange membrane fuel cell cathode (manuscript).

Author's contributions:

- Paper I The author was responsible for the synthesis of all of the catalysts, performed all electrochemical measurements (except fuel cell testing) and data analysis. The author is responsible for the interpretations of electrochemical results and primarily responsible for writing the manuscript.
- Paper II The author was responsible for the synthesis of all of the catalysts, performed all electrochemical measurements and data analysis. The author is responsible for the interpretations of electrochemical results and primarily responsible for writing the manuscript.
- Paper III The author was responsible for the synthesis of all of the catalysts, performed all electrochemical measurements (except fuel cell testing) and data analysis. The author is responsible for the interpretations of electrochemical results and primarily responsible for writing the manuscript.
- Paper IV The author was responsible for the synthesis of all of the catalysts, performed all electrochemical measurements (except fuel cell testing) and data analysis. The author is responsible for the interpretations of electrochemical results and primarily responsible for writing the manuscript.
- Paper V The author was responsible for the synthesis of all of the catalysts, performed all electrochemical measurements and data analysis. The author is responsible for the interpretations of electrochemical results and primarily responsible for writing the manuscript.
- Paper VI The author was responsible for the synthesis of all of the catalysts, performed all electrochemical measurements (except fuel cell testing) and data analysis. The author is responsible for the interpretations of electrochemical results and primarily responsible for writing the manuscript.

2. ABBREVIATIONS AND SYMBOLS

A	geometric surface area of an electrode
AEM	anion exchange membrane
AEMFC	anion exchange membrane fuel cell
BF	bright field
CCM	catalyst-coated membrane
CDC	carbide-derived carbon
CM	cyanamide
CNTs	carbon nanotubes
$C_{O_2}^b$	concentration of oxygen in the bulk solution
D_{O_2}	diffusion coefficient of oxygen
DCDA	dicyandiamide
DFT	density functional theory
E	electrode potential
E^0	standard potential
$E_{1/2}$	half-wave potential
E_{onset}	onset potential
EDX	energy-dispersive X-ray spectroscopy
ETFE	poly(ethylene-co-tetrafluoroethene)
F	Faraday constant
GC	glassy carbon
GDL	gas diffusion layer
HAADF	high-angle annular dark field
HMT-PMBI	hexamethyl-p-terphenyl poly(benzimidazolium)
HOR	hydrogen oxidation reaction
I	current
I_d	disc current
I_D	intensity of D peak
I_G	intensity of G peak
I_r	ring current
ICP-MS	inductively coupled plasma mass spectrometry
j	current density
j_d	diffusion-limited current density
j_k	kinetic current density
k	electrochemical rate constant for O_2 reduction
M- N_x	metal-coordinated to nitrogen
M-N-C	metal-nitrogen-carbon
MEA	membrane electrode assembly
mel	melamine
MP-AES	microwave plasma atomic emission spectroscopy
MPC	mesoporous carbon
MWCNT	multi-walled carbon nanotube
N	collection efficiency of the ring electrode

n	number of electrons transferred per O ₂ molecule
OMC	ordered mesoporous carbon
ORR	oxygen reduction reaction
P_{\max}	peak power density
PEM	proton exchange membrane
PEMFC	proton exchange membrane fuel cell
PGM	platinum-group metals
PSD	pore size distribution
PVP	polyvinylpyrrolidone
RDE	rotating disc electrode
RH	relative humidity
RHE	reversible hydrogen electrode
RRDE	rotating ring-disc electrode
SAC	single-atom catalyst
SCE	saturated calomel electrode
SEM	scanning electron microscopy
SHE	standard hydrogen electrode
SSA	specific surface area
STEM	scanning transmission electron microscopy
V_{micro}	micropore volume
V_{tot}	total pore volume
XPS	X-ray photoelectron spectroscopy
XRD	X-ray diffraction
ν	kinematic viscosity of the solution
ω	rotation rate of the electrode

3. INTRODUCTION

Energy is vitally important for our everyday lives and together with the improvement in the living standard, the need for energy is gradually increasing. While it is necessary, it is still taken for granted, leading to a possible energy crisis as well as damage to the environment, as over 80% of consumed energy is produced from non-sustainable fossil fuels (oil, natural gas and coal) [1]. For the clean and sustainable future, hydrogen is considered to play a vital role in the energy system. Hydrogen is an ideal energy carrier as it has high gravimetric energy density, it is non-toxic and non-polluting at conversion to energy. While hydrogen can be produced from non-renewable sources, its production is more and more leaning towards utilizing renewable ways, such as wind or solar energy applied for water electrolysis [1, 2].

Hydrogen has gained the most interest in the transport sector, where a lot of research has been done for around two decades already [3]. Today we can see that this has paid off as several automotive companies are producing low-temperature polymer electrolyte fuel cell electric vehicles [4, 5]. However, there is still a problem with the fuel cells, namely the need for scarce and expensive platinum-group metals (PGM) as electrocatalysts to speed up the anodic hydrogen oxidation reaction and cathodic oxygen reduction reaction [4, 6, 7]. This could be resolved, at least on the cathode side of the fuel cell, by changing the present acidic medium with alkaline as such less-corrosive environment offers a better opportunity to replace Pt-based materials with PGM-free ones [8]. As possible replacements, transition metal-nitrogen-carbon (M-N-C) type catalysts have shown performance comparable to Pt-based materials in alkaline conditions [9, 10].

The aim of the research presented in this PhD thesis was to develop PGM-free electrocatalysts for the oxygen reduction reaction occurring on the cathode of an anion exchange membrane fuel cell. To prepare the catalysts, nanocarbon support materials with varying textural and morphological properties were investigated, including composite of carbide-derived carbon/carbon nanotubes [I,II,IV], composite of graphene/carbon nanotubes [III] and commercially available [V] or self-made [VI] mesoporous carbon. The support materials were doped with nitrogen [I–VI] and transition metals (iron, cobalt, manganese) [II–VI] via high-temperature pyrolysis. The effect of different dopants as well as the structure of the support materials on the oxygen reduction activity was studied in half-cell tests via rotating disc electrode or rotating ring-disc electrode methods and also by using the synthesised materials as cathode catalysts in the anion exchange membrane fuel cell.

4. LITERATURE OVERVIEW

4.1 Polymer electrolyte membrane fuel cells

A fuel cell is a device that generates electricity by electrochemical reactions, namely by electrochemical oxidation of fuel, most commonly hydrogen, and reduction of oxygen. These reactions occur on the anode and the cathode, which are separated via electrolyte that carries the charged species. Based on the choice of fuel and electrolyte, fuel cells are divided into (i) alkaline fuel cell, (ii) phosphoric acid fuel cell, (iii) solid oxide fuel cell, (iv) molten carbonate fuel cell and (v) polymer electrolyte fuel cell. The latter type of fuel cells is most attractive for transportation applications, as they operate at low temperatures (<100 °C) and do not need possibly dangerous corrosive chemicals [11]. In such type of a fuel cell, electricity is produced by the electro-oxidation of hydrogen and electroreduction of oxygen, where the only by-products are water and heat. An automotive fuel cell stack (Figure 1) is made up of identical unit cells containing membrane electrode assembly (MEA). The MEA itself is comprised of (i) anode, where the hydrogen gas is oxidised, (ii) cathode, where the oxygen gas is reduced and (iii) a solid proton exchange membrane (PEM) separating the two sides (Figure 1). Both the anode and the cathode side are made of porous gas diffusion layers (GDLs), which transport reactants and products (water) to and from the catalyst layers. The MEA is sandwiched between the bi-polar plates through which the gaseous reactants are supplied, and the obtained electric current is collected [6].

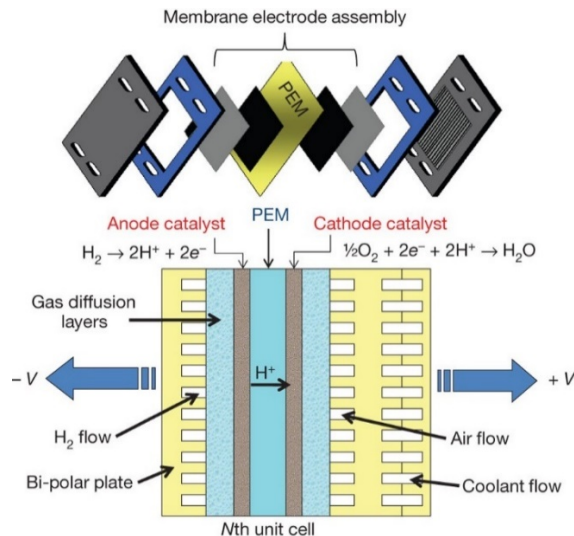


Figure 1. Unit cell cross-section in a fuel-cell stack and the components of an expanded MEA [6].

The proton exchange membrane fuel cells (PEMFCs) were already developed for the space missions in the 1960s by Willard Thomas Grubb and Leonard Niedrach. These first fuel cells utilised platinum-based catalysts to speed up the hydrogen oxidation reaction (HOR) and the oxygen reduction reaction (ORR), while already acknowledging that the commercialisation of PEMFCs would be problematic due to a large amount of Pt needed [12]. When looking at the current status, now around 60 years later, the PEMFCs are still using Pt-based catalysts, indeed the loading has been lowered, however, it is still not low enough. The US Department of Energy has set a target for year 2025 to decrease the platinum-group metal (PGM) usage to less than 0.10 g kW^{-1} ; the current status is around 0.125 g kW^{-1} [13], so improvements are needed, but it gets more and more difficult to reach the goal.

As the PGM-based catalysts impose limitations on the further commercialisation of PEMFCs, then there is a lot of research done and in progress to find replacements to these materials [14, 15], however, so far the Pt-based catalysts still remain the most active and most stable in acidic environment [6, 16]. In addition to problems with PGM catalysts, the acidic working conditions of PEMFC cause durability problems to the fuel cell components, as they degrade in such a harsh environment [17]. To avoid these limitations, an option is to switch to alkaline media and start using anion exchange membrane fuel cells (AEMFCs) instead. The higher pH is less harsh, so there is no need for expensive acid-resistant stack hardware, which is then reducing the price of fuel cells [8]. Additionally, the anion exchange membranes (AEMs) can be prepared from rather cheap polymer precursors, while costly fluorinated raw materials are needed for Nafion PEM [18]. The alkaline medium also offers another benefit as the kinetics of the ORR is faster in alkaline than in acidic medium, then non-precious metal-based materials are viable alternatives to the PGM-based catalysts [8, 17, 18].

The main principle and structure of the anion exchange membrane fuel cell is the same as for PEMFC – the MEA consists of anode, cathode and solid electrolyte (Figure 2). However, instead of protons, anions need to move through the membrane, thus instead of proton exchange membrane it uses anion exchange membrane (AEM) [19, 20].

During operation, humidified hydrogen gas is fed to anode, where it reacts with hydroxide anion with water and electrons being produced:



Humidified oxygen gas is fed to the cathode side, where the oxygen then reduces in the presence of water with hydroxide anion being formed:



which are then conducted through the AEM to participate in the hydrogen oxidation reaction. The overall reaction is:



so as in the PEMFC, only water and heat are also produced in the AEMFC [19].

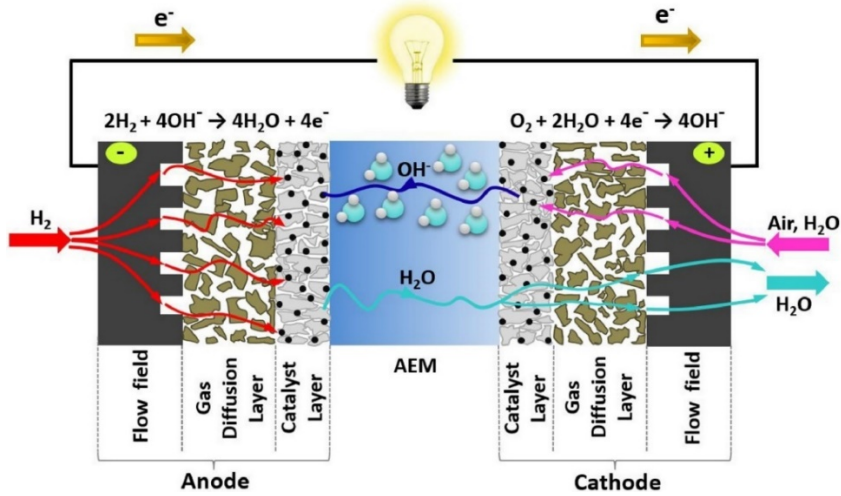


Figure 2. Schematic of the AEMFC together with illustrated water transport [20].

While AEMFCs are currently gaining popularity and there is a hope for a commercialisation, it was not the case even a few years back, as the performance of AEMFC was significantly worse than that of PEMFC. The remarkable increase in the AEMFC performance is a combination of several important factors: (i) development of better AEMs, (ii) operational changes made and (iii) improvement of catalyst materials [20]. These are discussed more in subsection 4.5.

4.2 Oxygen reduction reaction

Oxygen reduction reaction plays a vital role in the AEMFC as indicated above. In order to prepare suitable cathode catalysts, it is important to know how the ORR proceeds on these materials. In the alkaline conditions, the ORR can follow either direct 4-electron pathway,



two-electron pathway,



or $2 \times 2e^-$ pathway, in which hydroperoxide anion is further reduced:



or disproportionated:



All the standard potential (E_0) values are given versus the standard hydrogen electrode (SHE) at 25 °C [21].

The more detailed scheme of the ORR in alkaline media, which shows multiple possible oxygen-containing intermediates on catalyst surface and solution, is given in Figure 3. The first step of the ORR involves the adsorption of molecular O_2 (O_2^*). The transformation of O_2^- to $^*\text{OH}$ goes through bifurcation process via chemical (iii, v) or electrochemical (iv, vi) way [22].

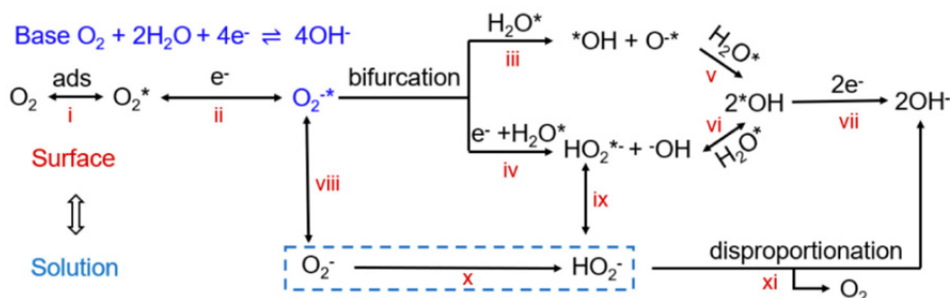


Figure 3. General mechanisms proposed for ORR in alkaline media [22].

While the ORR process is rather complex in alkaline media, then for the AEMFC application it is important that the cathode catalyst promotes the $4e^-$ or $2 \times 2e^-$ reduction pathway. With the two-electron pathway, the formed hydroperoxide ions are unwanted products as they damage the fuel cell components, including the catalysts and ever-important membrane.

4.3 Non-precious metal catalysts for oxygen reduction

4.3.1 Metal-free electrocatalysts

As a replacement for Pt-based catalysts for the ORR, an appealing approach would be to make entirely metal-free catalyst materials taking carbon as the basis. Carbon nanomaterials come in different forms and shapes, thus have gained much interest as ORR electrocatalysts. Among those are graphene,

carbon nanotubes, carbon nanofibers, carbide-derived carbon to name the least, however, all these pristine nanocarbons have shown only a moderate electrocatalytic activity towards the ORR while promoting primarily 2-electron reduction pathway [23–27]. Three strategies have been proposed to make inactive sp^2 carbon materials more active: (i) chemical doping by incorporating additional elements to the matrix of sp^2 carbon; (ii) physical intermolecular charge transfer via adsorption of polyelectrolyte chains; (iii) adding structural defects (like zigzag edges) [28]. Most promising of these approaches has been the chemical doping. Different heteroatoms have been widely used as dopants to improve the ORR activity of carbon materials, these include N [29–35], S [36–38], P [39, 40], B [41], F [42], I [43] as well as their combinations [44–47]. The addition of heteroatoms induces the charge density and/or spin density redistribution on the adjacent carbon atoms, making it thus favourable for O_2 adsorption, leading to enhanced ORR activity [34, 48, 49].

While several heteroatoms have shown great promise, then nitrogen is the most abundant and environmentally friendly compared to the others [21, 34]. Nitrogen has an extra electron and higher electronegativity than carbon. According to the density functional theory (DFT) calculations, the carbon atoms adjacent to the nitrogen dopants become positively charged [34]. This charge delocalisation influences the chemisorption of oxygen, so the usual end-on adsorption through a single bond (according to Pauling model) could be changed to bridge-like adsorption through two bonds (Yeager model) [34, 50]. This parallel or bridge-like adsorption of O_2 effectively weakens the O–O bond, finally leading to its breaking, which then facilitates the ORR [34].

The nitrogen atoms in carbon matrix form various moieties according to their specific location. Regarding the ORR, three have gained the most interest: pyridinic-N, graphitic-N and pyrrolic-N (Figure 4) [51–53], but there are still varying opinions, which is the most active centre. Rather unanimous opinion is that pyridinic-N is active N-species in alkaline media [33, 51, 54, 55], however, the other mentioned centres have been also reported to be ORR-active [56–59]. As the N-doped carbon nanomaterials usually contain several nitrogen moieties, then there are opinions that actually the coexistence of multiple N species is even more beneficial. For instance, Kabir *et al.* have claimed that in the first step of the ORR HO_2^- is formed on graphitic-N, followed by the OH^- production in the second step on pyridinic-N, and the hydrogenated nitrogen (including pyrrolic-N) most probably catalyses the full $2 \times 2e^-$ reduction of oxygen [60]. Additionally, Lai *et al.* have suggested that the ORR activity of electrocatalysts depends on their graphitic-N and pyridinic-N content with the first one having an effect on the diffusion-limited currents and the latter enhancing the onset potential of the ORR [61].

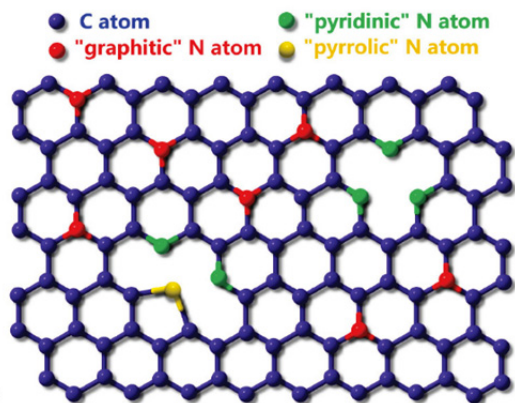


Figure 4. Different types of active sites in nitrogen-doped carbon catalysts [62].

4.3.2 Metal-nitrogen-carbon (M-N-C) catalysts

Although the metal-free catalyst materials have shown high ORR activity [28, 53, 63], the most promising non-precious metal catalysts are transition-metal and nitrogen-doped carbon (M-N-C) materials, which have already shown comparable or sometimes even exceeding performance as compared to Pt/C catalysts [9, 10, 64–66]. Such good ORR electrocatalytic activity of M-N-C materials is thought to come from the combination of different active sites, which involve (i) nitrogen moieties, like pyridinic-N (discussed in chapter 4.3.1), (ii) metallic nanoparticles or metal carbides covered with thin carbon layer (preferably nitrogen-doped), and (iii) transition metal-coordinated to nitrogen species (M-N_x) [64, 67, 68]. It has been suggested that on metallic particles covered with carbon, the ORR proceeds via $2 \times 2e^-$ pathway, while on M-N_x sites both the direct $4e^-$ and $2 \times 2e^-$ mechanisms occur [69–71]. As the origin of the ORR activity of M-N_x moieties, it has been proposed that these species are covalently bonded into the carbon basal plane, resulting in delocalized π -electron system in carbon support, which promotes the chemisorption of oxygen or reaction intermediates on metal centre [72].

There are two main approaches to obtain such beneficial M-N_x sites: (i) using precursors with the inner N₄ coordination around the transition metal centre (metal phthalocyanines and porphyrins) [73–76] or (ii) by creating them by combining metal and nitrogen-containing precursors via high-temperature pyrolysis. For the latter, different cheap transition metal salts and simple nitrogen-rich sources (*e.g.* dicyandiamide, melamine, urea) can be used [9, 64, 65]. An option is also to use precursors which are known to form complexes with metal-coordinated to nitrogen centre, such as 1,10-phenanthroline as nitrogen source together with transition metal acetates [77, 78].

It is evident that the transition metal in M-N-C catalysts plays a critical role in the ORR process. As metals in M-N-C type catalysts, iron and cobalt have been studied most extensively [79–85]. Both have indeed demonstrated

excellent results, however, come with some problems. Cobalt-based materials have often shown considerable peroxide production during the ORR process [80, 86]. This has been explained by the fact that on Co-N-C catalyst materials the kinetics of peroxide desorption is considered to be faster than the kinetics of four-electron reduction of oxygen [86]. Iron-based catalysts have usually lower peroxide production [86, 87], but are known to be subject to Fenton's reaction (especially at low pH) [88, 89]. To tackle the issues with monometallic catalysts, an option is to prepare bimetallic ones. The combination of both cobalt and iron in one catalyst material has shown good results for the ORR, even surpassing the activity of single metal materials [65, 90, 91]. This is thought to originate from the synergetic effects of Fe-N₄ and Co-N₄ active centres [91, 92], as the DFT calculations have indicated that Fe and Co in neighbouring Fe-N₄ and Co-N₄ active sites have higher ORR activity than in monometallic Fe-N₄ and Co-N₄, respectively [92]. In addition to making Co and Fe bimetallic materials, incorporating manganese could be also beneficial. It has been reported that combining manganese with iron or cobalt increases the ORR activity as well as improves stability [89, 93–95].

To utilise the metal additive to the maximum efficiency while maintaining the high selectivity and stability during the ORR, preparation of single-atom catalysts (SACs) with atomically distributed active sites anchored on the carbon matrix could be the key. In M-N-C type SAC materials, the afore-mentioned M-N_x moieties are considered as the main active sites as well. While symmetrical x=4 configuration is deemed the most active species [96], then asymmetrical M-N_x have also proven to be beneficial [97, 98]. In M-N_x moieties, in addition to the central metal atom [96], the type of nitrogen configuration could also be important. For instance, according to the DFT calculations, in Fe-pyrrolic-N₄ formation, a stronger electron depletion around iron atom is observed than in Fe-pyridinic-N₄, thus causing a more positive oxidation state of Fe centre in the pyrrole-type configuration than in pyridine-type one [97]. As part of rational design of SACs, the porous structure is also important. In order to obtain good distribution of active sites, the microporous nature (pore diameter <2 nm) with high specific surface area could be beneficial [87], however, mesopores (diameter 2 to 50 nm) and macropores (>50 nm) enable the exposure of metal-based active sites and improve the mass transfer due to the larger pore size [99]. So, to prepare ORR-active SACs, the design of active sites as well as support material is important.

4.4 Carbon nanomaterials

For the preparation of nitrogen-doped or M-N-C type catalysts, the chosen carbon substrate is the basis for all. A suitable catalyst support should (i) provide good electrical conductivity, (ii) offer corrosion stability under harsh conditions as well as (iii) have high surface area with feasible porous structure [100]. The latter is important in the fuel cell application and suitable materials

should have mesopores present, which enhance the mass transport in the catalyst layer, especially as micropores and any active sites located there could be covered with ionomer during the operation [87, 101]. Carbon nanomaterials come in various forms, so the selection for potential support materials is rather wide [9, 53, 100].

Carbide-derived carbon (CDC) is a nanocarbon material made by removing the metal or semi-metal atoms from the lattice of a respective carbide, thus leaving behind a porous carbon. The CDCs have a very high specific surface area (up to over $2000 \text{ m}^2 \text{ g}^{-1}$) and very good stability, which is why they are employed in electrochemical capacitors mostly [102–105]. The CDCs can be produced from numerous carbides, like SiC, TiC, ZrC, B₄C and Mo₂C. To remove the metal/semi-metal from the carbide lattice, chlorination is the most common method used, and by varying the conditions (*e.g.* chlorination temperature), the porous structure of final CDC can be modified and easily reproduced in large quantities. Depending on the starting carbide and chosen synthesis parameters, CDCs with pores ranging from $<1 \text{ nm}$ to *ca.* 4 nm can be produced [102, 106, 107].

Carbon nanotubes (CNTs) are carbon allotropes with cylindrical structure. They consist of either one rolled-up graphitic sheet, namely single-walled carbon nanotube, with a diameter of *ca.* 1.4 nm , or several coaxial ones, namely multi-walled carbon nanotube (MWCNT), with an interlayer spacing of 3.4 \AA and a diameter of $10\text{--}20 \text{ nm}$ usually. The length of CNTs can be up to hundreds of microns or even centimetres [108]. The CNTs are commonly made using catalyst assisted chemical vapour deposition technique from hydrocarbon-based gaseous precursors, like methane, acetylene, propylene, and others [108]. The CNTs have unique tubular structure, excellent resistance to corrosion, relatively large accessible surface area, and excellent electrical conductivity, which makes them attractive to be used as electrocatalysts or catalyst supports [100, 109].

Graphene is a nanomaterial comprised of a single layer of sp^2 carbon. Graphene has high surface area (the theoretical specific surface area of single layer graphene is $2630 \text{ m}^2 \text{ g}^{-1}$), good electrical conductivity and mechanical strength [110–112]. Chemical vapour deposition technique is one of the most popular methods for large-scale production of mono- or few-layer graphene films [111]. The single-layer graphene is very difficult to synthesise in large quantities, meaning it is not well suitable for application purposes, like making fuel cell catalysts. For that purpose, other graphene-based materials, such as graphene comprised of multiple layers, graphene oxide or reduced graphene oxide is often used [100, 113].

Mesoporous carbons have often uniform and interconnected porous network, predominantly comprising of only mesopores. The pore size and shape can be tuned by varying synthesis methods. In addition, such carbon materials have good electrical conductivity and high surface area [114–116]. Mesoporous carbons are typically synthesised using either hard- or soft-templating approach [116]. Hard-templating uses pre-formed rigid mesoporous materials, such as silica, zeolite, or other colloidal crystals, which are combined with carbon

precursor, followed by carbonisation. The used template is removed via chemical etching in harsh acidic or alkaline conditions (*e.g.* HF, NaOH) [116–118]. Soft-templating is based on the self-assembling of carbon precursors with a block copolymer through hydrogen bonding and/or covalent bonding in alkaline or acidic environment, followed by thermopolymerisation and carbonisation, during which template is removed [115, 116, 118]. The soft-templating of phenolic resins with triblock copolymers (*e.g.* Pluronic F127) is a rather simple procedure to produce nanocarbon materials with narrow size distribution of mesopores [119].

4.5 Performance of anion exchange membrane fuel cells

The AEMFC performance is impacted by the anion exchange membrane, HOR and ORR catalyst materials as well as operation parameters [18, 20]. As the AEM plays a critical role in the AEMFC, it is important that it has the needed characteristics, like OH⁻ conductivity, chemical and thermal stability, low gas permeability, feasible mechanical properties (good strength, flexibility) and low cost [120]. The AEM generally comprises of a polymer backbone and functional groups or side chains, which provide hydroxide transportation pathways [120, 121]. The main concern for the AEM from the beginning has been the OH⁻ conductivity, which in first years was around 5 to 20 mS cm⁻¹, so nowhere near to compete with H⁺ conductivity of PEMs. This was explained to be due to the four times higher diffusion coefficient of H⁺ than of OH⁻ and to overcome it, AEMs would need to have significantly higher ion exchange capacity. Lately, however, the best-performing AEMs have shown conductivities from 60 to 132 mS cm⁻¹, meaning significant improvements have been done [18]. Some of the noteworthy early developments include radiation-grafted poly(ethylene-co-tetrafluoroethylene) (ETFE) based AEM by Varcoe *et al.* in 2007 with peak power density (P_{\max}) of 130 mW cm⁻² achieved in an AEMFC [122], phosphonium-functionalised polysulfone AEM by Yan *et al.* in 2010 (P_{\max} of 260 mW cm⁻²) [123] and a quaternized poly(phenylene) AEM with a hydrophobic perfluorinated ionomeric binder by Kim *et al.* in 2013 (P_{\max} of 580 mW cm⁻²) [124]. An improvement in the AEMFC results (P_{\max} of 600 mW cm⁻² with Pt/C anode) with lower PGM usage was reported by Zhuang *et al.* by using quaternized polysulfone AEM and ion-aggregated polysulfone binder in 2015 [125]. The same year, a commercially available Tokuyama A901 AEM showed high P_{\max} of 780 mW cm⁻² [126]. It should be noted that all of them incorporated PGM-based catalysts on the cathode and anode. The significant improvement of AEMFC performance in latter three reports comes from the understanding that the key to the better performance seems to be reducing the water uptake of the AEM and the ionomeric binder, while not losing hydroxide conductivity [8]. Following the footsteps of these works has led to the excellent performance AEMs and AEMFCs we are seeing today.

As is evident from the AEM development, then water plays an important role in the AEMFC. While AEMFC and PEMFC are schematically very similar, their operation fundamentally differs. In the PEMFC, water is just a product, however, in the AEMFC it is both a product as well as a reactant – two water molecules are used up during the reduction of one O₂ molecule on the cathode, while four molecules are produced on the anode (Figure 2). Additionally, during the AEMFC operation, every hydroxide anion moving from cathode to anode brings around eight water molecules with it via electro-osmotic drag [20]. This can easily lead to anode flooding and the excess liquid water on the cathode can also cause mass-transport limitations during the AEMFC operation, both of which are detrimental to the performance. This means that in addition to the high stability and hydroxide conductivity of AEMs, they should also have high water permeability to allow the back diffusion of water from anode to the cathode [18, 20, 127]. The water imbalance can also be somewhat controlled by optimising the AEMFC working conditions as well. As shown by Omasta *et al.*, changing the flow rate and humidity of incoming gases can improve the AEMFC performance noticeably [128, 129]. Additionally, changing the hydrophilicity of the used gas diffusion layers has shown to improve the AEM fuel cell results [126, 128]. The water balancing in an AEMFC is a difficult task, but choosing the feasible operation conditions is at utmost importance to obtain high performance.

In addition to AEM and water balancing, the used electrocatalysts are equally if not more important. One of the reason why AEMFC performance significantly improved circa 2015 is due to the change in the HOR electrocatalyst, as for instance, Zhuang *et al.* showed a jump from peak power density from 600 to 1000 mW cm⁻² by replacing the Pt/C anode catalyst with PtRu/C one [125]. Since then PtRu/C has been widely used as anode catalyst in the AEMFC, however, there is still a controversy over where such improvement originates [20]. One suggestion is that as ruthenium is more oxophilic than platinum, then its addition to the anode facilitates the adsorption of OH_{ad} species, which then react with the hydrogen intermediates (H_{ad}) that are adsorbed on the Pt surface sites [130]. Another option is that the alloying with ruthenium shifts the Pt-H binding energy to a positive direction, thus leading to enhanced HOR activity [131]. One thing is certain though, the fundamental HOR kinetics is improved with PtRu-based catalysts in comparison to just Pt-based. However, as the kinetics of the ORR is still significantly more sluggish than HOR, then the performance of the cathode catalyst is expected to have a large impact on the overall AEMFC behaviour [20]. All the results mentioned above were based on Pt/C cathode catalysts. However, cheaper replacements are needed, so great efforts are made to find suitable non-precious metal-based alternatives to the Pt/C, while still obtaining good ORR and AEMFC performance.

As prospective alternatives to the Pt-based catalysts for ORR, different non-precious metal-based materials indeed have shown potential as was discussed in subsection 4.3. Such PGM-free materials have been already tested in AEMFCs and selection of the results reported in the literature on non-precious metal cathode catalysts is shown in Table 1. It can be seen that the peak power density

values range from about 30 to $>1000 \text{ mW cm}^{-2}$, the latter values are also among the best overall performances achieved with Pt-free cathode catalysts. It is also evident that the AEM used plays a crucial role in the fuel cell performance, for example several high-performing MEAs use the radiation-grafted poly(ethylene-cotetrafluoroethylene)-based (ETFE) AEMs developed by Prof. John Varcoe [132]. With the commercially available AEMs from Tokuyama (not in production any longer) and Fumatech (FAA series) the obtained power maxima are not that high. A rather good performing AEM is also hexamethyl-p-terphenyl poly(benzimidazolium) (HMT-PMBI)-based AEM (developed by Prof. Steven Holdcroft [133]), which seems to be working well with wide range of non-precious metal catalysts. The HMT-PMBI-based AEM is also mostly used in this work [I-III, V, VI] apart from [IV], where ETFE-based AEM was employed.

As can be seen in Table 1, a wide selection of catalysts has been used in the AEMFC with varying dopants and carbon supports [9, 134, 135]. In case of transition metals, no metal seems to be superior, however, several bimetallic catalysts have shown rather impressive AEMFC performance. While the choice of AEM is important, equally important are the preparation of the MEA and the test parameters, such as gas flow rates, backpressure, humidity of gases and temperature of a fuel cell, that affect the AEMFC performance [20, 128, 136, 137].

Table 1. Comparison of H_2/O_2 AEMFC results using Pt-free cathode catalysts.

Cathode catalyst	Cathode loading (mg cm^{-2})	Membrane	T ($^{\circ}\text{C}$)	P_{max} (mW cm^{-2})	Ref.
F,S,N-rGO	1.5	HMT-PMBI	85	46	[138]
N-CNT	5	FAA, Fumatech	50	37.3	[139]
NHCS-W	4	Tokuyama A201	60	109	[140]
CNT/HDC-1000	2	In-house AEM	50	280	[141]
NHC	1	FAA-3, Fumatech	70	228	[142]
Co/N/MWCNT	0.6	A201, Tokuyama	50	120	[143]
Co/N/CDC	1.5	A201, Tokuyama	50	78	[144]
N-C-CoO _x	2.4	LDPE-BTMA	65	1050	[145]
Co@G/C 600	$0.4 \text{ mg}_{\text{Co}} \text{ cm}^{-2}$	A201, Tokuyama	60	412	[146]
MCS (Mn-Co spinel)	$0.58 \text{ mg}_{\text{metal}} \text{ cm}^{-2}$	<i>a</i> QAPS-S ₈	60	1100	[147]
SiCDC/CNT(1:3)/CoPc	0.69	ETFE	60	470	[79]
Fe/Co/IL-CNF-800b	2	HMT-PMBI	60	195	[148]
0.14Co0.01Fe-CB	1.28	ETFE	60	304	[90]
Fe-N-Gra	2	HMT-PMBI	60	243	[82]
FeCoN-MWCNT	0.745	FAA-3-05-rf	60	692	[75]
FeCoNC	2	HMT-PMBI	60	415	[65]
Fe/N/C	2	<i>a</i> QAPS-S ₈	60	450	[149]
CoFe/VC	2.4	ETFE	70	1350	[150]
Fe _{0.5} -NH ₃	1.5	ETFE	60	1100	[88]
$\alpha\text{-Mn}_2\text{O}_3/\text{Fe}_{0.5}\text{-NH}_3$	1.2 (FeNC)	ETFE	60	1000	[88]
Fe-N-C	2	HMT-PMBI	60	220	[151]

For practical application, the AEMFCs have to show excellent performance as well as high durability. The U.S. Department of Energy targets for 2022 are that H₂/O₂ fed AEMFCs should reach 1000 mA cm⁻² at 0.65 V and show less than 10% voltage decay over 1000 h at 0.6 mA cm⁻² with overall PGM loading being ≤0.2 mg cm⁻² [152]. While such initial performance has been obtained [153], the durability is still an issue. The AEMFC performance losses can come from improper water management, carbonation when exposed to CO₂ and degradation of components (electrocatalysts, AEM and ionomeric binder) [154]. Water management has been discussed before, however, in terms of durability, the intrinsic water imbalance hinders the long-term performance as the low water content in the cell leads to poor ionic conductivity or even degradation of the AEM, but high water content could lead to flooding of the electrodes and subsequent mass transport issues [121]. The swelling of AEM due to water is also an issue, as a higher number of functionalised cationic groups, which are needed for high anionic conductivity, leads to the higher swelling ratio and reduced mechanical strength. This means the challenge in designing the AEM is finding the optimal anionic conductivity while maintaining feasible mechanical properties [155]. The alkaline environment also can chemically degrade the AEM, as the OH⁻ anions can act as nucleophiles and attack the cationic functional groups leading to their splitting [155, 156]. For practical application air should be used instead of pure oxygen on the cathode of the AEMFC, then it raises the issue of carbonation due to the CO₂ as the latter reacts with OH⁻, leading to (bi)carbonate formation [154]. This (bi)carbonate build-up reduces the OH⁻ anions mobility and increases the ohmic resistance as well as could lead to pH drop on the anode, reducing the overall cell voltage [154]. In order to have feasible AEMFC durability, all the prior mentioned issues need attention and feasible strategies to mitigate the effect and in addition, the chosen electrocatalysts need to possess excellent stability in alkaline media, so that they would not cause extra problems during the fuel cell operation.

5. EXPERIMENTAL

5.1 Pretreatment and preparation of carbon nanomaterials

Multi-walled carbon nanotubes (CNT, diameter of 30 ± 15 nm, length of 5–20 μm and purity $>95\%$, purchased from NanoLab Inc., USA) were acid-treated before usage. For the acid treatment, 25 mL of concentrated H_2SO_4 and 25 mL of concentrated HNO_3 was added to 500 mg of CNTs in a 500 mL three-necked reactor. The mixture was heated on a magnetic stirrer for 2 h at 55°C and for 3 h at 80°C . After cooling, the CNTs were filtered on a vacuum filter, washed with Milli-Q water and dried at 60°C [I,II].

Carbide-derived carbon (CDC) synthesised from silicon carbide via chlorination (SiC_HiB [I,II] or SiC_LoB [IV,VI]) was purchased from Skeleton Technologies (Estonia). To obtain more uniform size distribution of grains, the CDC material was ball-milled at 400 rpm for 2 h (4 \times 30 min, 5 min cooling breaks). For the dry ball-milling 200 mg of CDC and 50 ZrO_2 balls with 5 mm in diameter were added into the ZrO_2 grinding bowl [I,II]. For the wet ball-milling, 200 mg of CDC, 20 mg of polyvinylpyrrolidone (PVP, molecular weight = 40,000; Sigma-Aldrich), 3 mL ethanol, and 20 g of ZrO_2 balls (diameter 0.5 mm) were added to the grinding bowl [IV,VI].

For the ordered mesoporous carbon (OMC) synthesis, the protocol by Ghimbeu *et al.* [115] was adopted. In a typical synthesis, 0.41 g phloroglucinol (98%, Alfa Aesar), 0.305 g of glyoxylic acid monohydrate (98%, Acros Organics) and 0.805 g of Pluronic F27 (Sigma-Aldrich) were dissolved in 20 mL of ethanol under magnetic stirring at room temperature for 30 min. Then the mixture was transferred to a Petri dish and kept at room temperature for 8 h in order to evaporate ethanol. This was followed by thermopolymerisation at 80°C for 12 h. The resultant amber-like substance was scraped from the Petri dish and pyrolysed using a small tube furnace (MTF 250/400/850 mm, Carbolite Ltd.) in flowing N_2 (99.999%, Linde Gas) atmosphere at 850°C for 2 h, at a heating rate of 3°C min^{-1} . After cooling down slowly to room temperature, the prepared carbon material was collected and ball-milled (200 mg at a time) for 30 min at 400 rpm, together with six zirconium dioxide balls (1 cm in diameter) in the grinding bowl [VI].

Multi-walled carbon nanotubes (NC3150; purity $>95\%$) from Nanocyl S.A. (Belgium) [III,IV,VI], graphene nanoplatelet aggregates (sub-micron particles, specific surface area of $750\text{ m}^2\text{ g}^{-1}$ according to the specification sheet) from Strem Chemicals (USA) [III], and Mesoporous Engineered Catalyst Support based on carbon (MPC) from Pajarito Powder, LLC (USA), product code: ECS-004601 [V] were used without any pretreatment.

5.2 Synthesis of nitrogen and/or transition metal doped nanocarbons

5.2.1 Nitrogen and/or cobalt doped CDC/CNT composites

15 mg of ball-milled CDC and 15 mg CNTs were dispersed in ethanol. 3 mg of PVP was added as a dispersing agent. In case of metal doping, 3.7 mg of $\text{Co}(\text{NO}_3)_2 \times 6\text{H}_2\text{O}$ (purity $\geq 98\%$, Sigma-Aldrich) was added as well [II]. Then the mixture was treated in an ultrasonic bath (Branson 1510E-MTH; frequency: 40 kHz, power output: 70 W, Branson®) for 30 min to disperse the nanocarbon materials. Then 0.6 g of nitrogen precursor was added. Used nitrogen precursors were urea, melamine (mel), dicyandiamide (DCDA) [I,II] and cyanamide (CM) [II] (all purchased from Sigma-Aldrich). This mixture was treated in the ultrasonic bath for 2 h until uniform dispersion was achieved. The prepared liquid dispersion was allowed to dry in an oven at 60 °C. The obtained dry blackish powder was then pyrolysed in N_2 atmosphere at 800 °C for 1 h, using a heating rate of 10 °C min^{-1} . The obtained catalyst materials are designated as N-CDC/CNT_urea, N-CDC/CNT_mel, N-CDC/CNT_DCDA, N-CDC/CNT_CM [I], Co-N-CDC/CNT_urea, Co-N-CDC/CNT_mel, Co-N-CDC/CNT_DCDA [II].

5.2.2 Transition metal and nitrogen doped graphene/CNT composites

50 mg of graphene nanoplatelets (Gra), 50 mg of CNTs, 10 mg of PVP, and either 12.4 mg of cobalt salt ($\text{Co}(\text{NO}_3)_2 \times 6\text{H}_2\text{O}$, Sigma-Aldrich) or 8.9 mg of iron salt ($\text{FeCl}_2 \times 4\text{H}_2\text{O}$, Sigma-Aldrich) or 6.2 mg Co and 4.45 mg Fe salts were mixed in ethanol. The mixture was treated for 30 min in the ultrasonic bath. After that, 2 g of melamine was added, and the mixture was sonicated again until a uniform dispersion was achieved (at least 60 min). The prepared mixture was dried at 60 °C and pyrolysed in N_2 atmosphere. The precursor mixture was inserted to the heating zone after 800 °C was reached (ramping rate: 50 °C min^{-1}), kept there for 1 h, and then quickly removed. The obtained catalyst materials are designated as Co-N-Gra/CNT, Fe-N-Gra/CNT, CoFe-N-Gra/CNT [III].

5.2.3 Transition metal and nitrogen doped CDC/CNT composites

As nitrogen source 1,10-phenanthroline (purity $>99\%$, Acros Organics) and as metal precursors iron(II) acetate (purity 95%, Sigma-Aldrich) and cobalt(II) acetate (purity $>98\%$, Alfa Aesar) were used. Firstly, metal acetates together with 1,10-phenanthroline (molar ratio 1:6) were dissolved in ethanol. The transition metal acetates were taken in such amount that the mass of the metals (Fe or Co) would correspond to 1 wt% of the carbon materials (CDC and CNT) and in case of dual doping to 0.5 wt% Fe and 0.5 wt% Co. This solution of

metal acetate(s) and 1,10-phenanthroline was treated in an ultrasonic bath for 30 min. After that, CDC:CNT (1:1 weight ratio) and PVP (1/10 of CNTs weight) were added to the mixture and sonicated for at least 60 min until a uniform dispersion was achieved. The prepared liquid dispersion was dried at 60 °C and pyrolysed in N₂ atmosphere. The precursor mixture was inserted to the heating zone at 800 °C, kept there for 60 min and then quickly removed. The catalyst materials are designated as Fe-N-CDC/CNT, Co-N-CDC/CNT, and CoFe-N-CDC/CNT [IV].

5.2.4 Transition metal and nitrogen doped mesoporous carbon

Firstly, the transition metal acetates together with 1,10-phenanthroline were dissolved in ethanol. Typical amounts were: 12.5 mg of 1,10-phenanthroline, 1 or 2 mg of iron(II) and cobalt(II) acetate and 1.4 mg of manganese(II) acetate tetrahydrate (>99%, Sigma-Aldrich). The transition metal acetates were taken in such amount that the total mass of the metals would correspond to 1 wt% of the MPC, and in case of bimetallic materials the mass of both metals would be equal. This solution of metal acetate(s) and 1,10-phenanthroline was treated in an ultrasonic bath for 30 min, after which 50 mg of MPC was added and further sonicated for at least 60 min until a uniform dispersion was achieved. The prepared liquid mixture was dried at 60 °C and pyrolysed in N₂ atmosphere. The precursor mixture was inserted to the heating zone at 800 °C, kept there for 1 h and then quickly removed, thus obtaining the catalyst material.

According to the metal precursors used, the electrocatalyst materials are designated as follows: Fe-N-MPC, Co-N-MPC, CoFe-N-MPC, FeMn-N-MPC, and CoMn-N-MPC [V].

5.2.5 Transition metal and nitrogen doped OMC-based materials

Typically 12.5 mg of 1,10-phenanthroline, 1 mg of iron(II) acetate and 1 mg of cobalt(II) acetate were dissolved in ethanol utilising an ultrasonic bath for 30 min. After that, 50 mg of carbon material was added to the solution, followed by 1 h of sonication. As carbon support, OMC as well OMC/CDC and OMC/CNT composites were used; in composites the carbons were taken in equal amounts per weight. The obtained dispersion was dried at 60 °C and pyrolysed in N₂ atmosphere. The precursor mixture was inserted to the heating zone at 800 °C, kept there for 60 min and then quickly removed. The catalyst materials are designated according to the carbon support as CoFe-N-OMC, CoFe-N-OMC/CDC, CoFe-N-OMC/CNT [VI].

5.3 Physico-chemical characterisation methods

For the scanning electron microscopy (SEM) measurements, the materials were suspended in 2-propanol/Milli-Q water (Millipore, Inc.) (volume ratio 1:1) and then pipetted onto polished glassy carbon (GC) substrates and dried at 60 °C. A high-resolution scanning electron microscope Helios NanoLab 600 (FEI Company) was employed. The INCA Energy 350 energy-dispersive X-ray (EDX) spectrometer (Oxford Instruments) connected to the microscope was used to assess the elemental composition of the samples.

Scanning transmission electron microscopy (STEM) studies were carried out on a Titan Themis 200 (FEI) (S)TEM equipped with Cs-probe corrector at 200 kV. EDX mapping was conducted using the SuperX EDX system (Bruker) connected to the same microscope. The sample for STEM observation was prepared by drop-casting the dispersion of the catalyst material in isopropanol onto lacey carbon film-coated copper TEM grids.

N₂ adsorption/desorption isotherms of the catalyst materials were recorded at the boiling temperature of nitrogen using a NovaTouch LX2 analyser (Quantachrome). Prior to the measurements, the samples were degassed in vacuum at 300 °C and backfilled with N₂. The total pore volume (V_{tot}) was measured close to the saturation pressure ($P/P_0=0.97$). The specific parameters were calculated by applying quenched solid density functional theory equilibria model for slit-type [I-V] or slit/syl [VI] type pores, using the Brunauer-Emmett-Teller [I-IV] and Barrett, Joyner and Halenda models [V,VI].

For Micro-Raman spectroscopy studies, the materials were suspended in 2-propanol/Milli-Q water (volume ratio 1:1), pipetted onto Si wafers and dried at 60 °C. Raman spectra were recorded in the back-scattering geometry on an inVia Renishaw spectrometer together with an Olympus confocal microscope (50X objective) and an argon ion laser operated at 514.5 nm. A baseline correction was used to compensate for the small fluorescence background and multiple-peak fitting procedure was applied [157]. The intensities of I_{D1} and I_{G} (integrated areas under the bands) as well as their half widths were extracted from the fitting of the curves by Voigt functions.

The X-ray diffraction (XRD) analysis of catalyst powders was carried out using Bruker D8 Advance diffractometer with Ni-filtered Cu K α as a radiation source and LynxEye line detector. The diffraction patterns were collected using scanning step of 0.0183° 2 θ in a range of 5° to 90° and the counting time of 525 s per step. The diffraction patterns were analysed using the full-profile analysis software Topas 6 (Bruker).

For X-ray photoelectron spectroscopy (XPS) studies [I,III-VI], the catalyst materials were suspended in 2-propanol/Milli-Q water (volume ratio 1:1), pipetted onto GC plates and dried at 60 °C. The XPS measurements were conducted under ultra-high vacuum using a non-monochromatic twin anode X-ray tube (Thermo XR3E2) with the characteristic energy of 1253.6 eV (Mg K α) and an electron energy analyser SCIENTA SES 100. The survey scan was collected using the following parameters: energy range = 1000 to 0 eV, pass

energy = 200 eV, step size = 0.5 eV, step duration 0.2 s and number of scans 5. The following parameters for the detailed N1s spectra were used: energy range = 410–390 eV, pass energy = 200 eV, step size = 0.2 eV, step duration 0.2 s, and number of scans at least 50. The raw data were processed using the Casa XPS software and involved removal of X-ray satellites, peak fitting (using the Gauss-Lorentz hybrid function (GL 70, Gauss 30 %, Lorentz 70 %) and blend of linear and Shirley-type backgrounds). From the obtained peak areas the atomic concentrations were calculated using built into Casa XPS Scofield photo-absorption cross-sections and the electron effective attenuation lengths. The XPS spectra in article [II] were acquired using a Kratos Axis Supra spectrometer, equipped with a mono-chromatic Al K α source operating at 300 W. The survey spectra were acquired using 160 eV pass energy and step size of 1 eV with a dwell time of 100 ms averaged over number of scans. The high-resolution regional spectra of C1s and N1s were acquired using 20 eV pass energy and step size of 0.1 eV with a dwell time of 100 ms averaged over number of scans. The data analysis was performed using Casa XPS software and fitted with a 70% Gaussian/ 30% Lorentzian line shape with a fixed full-width at half maxima of 1.0–1.2 eV for C1s and of 1.3–1.5 eV for N1s peak.

The transition metal concentration in the catalyst materials was determined using microwave plasma atomic emission spectroscopy (MP-AES) [III-VI]. 10 mg of sample was dissolved with Anton Paar Multiwave PRO microwave digestion system in NXF100 vessels (PTFE/TFM liner) using an acid mixture of 4 mL of HNO $_3$ (65%; Carl Roth, ROTIPURAN[®] Supra) and 2 mL of H $_2$ O $_2$ (30%; Carl Roth, ROTIPURAN[®]). Samples were digested at 230 °C and at pressures between 45–50 bar. After dissolution, the samples were diluted with 2% HNO $_3$ solution to obtain metal concentrations of around 5 mg L $^{-1}$ and analysed using Agilent 4210 MP-AES.

The bulk concentration of metals in materials was determined by inductively coupled plasma mass spectrometry (ICP-MS) [II,IV]. The samples were dissolved with Anton Paar Multiwave PRO microwave digestion system using same digestion parameters that were used for catalyst materials. Analysis was performed using Agilent 8800 ICP-MS/MS in NoGas mode and H $_2$, N $_2$ O reaction modes.

5.4 Electrode preparation and electrochemical measurements

As a substrate material for the rotating disc electrode (RDE) measurements a glassy carbon (GC) disc (cut from a GC-20SS rod, Tokai Carbon Ltd., Japan) pressed into Teflon holder was used as. The electrode's geometric area was 0.196 cm 2 . The GC electrode was polished to a mirror finish using 1 and 0.3 μ m alumina slurries (Buehler) and the surface was cleaned via sonication in Milli-Q water and 2-propanol for 5 min in each solvent. For the rotating ring-disc electrode (RRDE) measurements, a fixed-disc tip of GC disc/Pt ring [I, III-V] or

fixed-disc tip of GC disc/Au ring [II] (Pine Research) was used. The geometric area of the GC disc was 0.164 cm². The surface of the electrode was polished using 1, 0.3 and 0.05 μm alumina powders (Buehler) and cleaned the same way as for the RDE experiments.

To make a catalyst suspension, 2 mg [I-III] or 5 mg [IV-VI] of catalyst material was dispersed in the mixture of 490 μL of 2-propanol and 490 μL of Milli-Q water or in 980 μL 2-propanol [VI]; 20 μL of Nafion ionomer solution (5 wt%, Sigma-Aldrich) was added. The suspensions were sonicated in an ultrasonic bath for at least 1 h until uniform dispersion was achieved. In order to obtain a catalyst loading of 0.1 [I], 0.2 [II,III] or 0.4 mg cm⁻² [IV-VI], a certain amount of catalyst suspension was pipetted onto the cleaned GC surface and allowed to dry at 60 °C.

All electrochemical measurements were performed in alkaline solution, 0.1 M KOH (purity ≥85%, Sigma-Aldrich), in a three-electrode glass cell. Ar (99.999%, Linde Gas) or O₂ (99.999%, Linde Gas) was used for saturating the electrolyte solution and a continuous flow of the corresponding gas was retained over the solution during the experiment. The GC disc coated with respective catalyst was the working electrode. A saturated calomel electrode (SCE) connected via a salt bridge was used as a reference electrode. The auxiliary electrode was a carbon rod, which was separated from the working electrode compartment by a glass frit. The current densities given in this work were calculated per geometric area of the GC electrode employed. All potentials presented were converted to the reversible hydrogen electrode (RHE) by applying an equation: $E_{\text{RHE}} = E_{\text{SCE}} + 0.241 \text{ V} + 0.059 \text{ V} \times \text{pH}$. The electrochemical experiments were conducted on PGSTAT30 Autolab potentiostat/galvanostat (Eco Chemie B.V., The Netherlands) controlled with General Purpose Electrochemical System (GPES) software. A CTV101 speed controller together with an EDI101 rotator (Radiometer) were used to conduct the RDE measurements. For the RRDE measurements, an AFMSRX rotator together with a MSRX speed controller (Pine Research, USA) were employed.

The electrode rotation rates (ω) applied during the RDE measurements were 360, 610, 960, 1900 and 3100 rpm. The obtained RDE polarisation data was analysed using the Koutecky-Levich (K-L) equation (8) [158]:

$$\frac{1}{j} = \frac{1}{j_k} + \frac{1}{j_d} = -\frac{1}{nFkC_{\text{O}_2}^b} - \frac{1}{0.62nFD_{\text{O}_2}^{2/3}\nu^{-1/6}C_{\text{O}_2}^b\omega^{1/2}} \quad (8)$$

where j is the measured current density, j_k and j_d are kinetic and diffusion-limited current densities, respectively, n is the number of electrons transferred per O₂ molecule, k is the electrochemical rate constant for O₂ reduction (cm s⁻¹), F is the Faraday constant (96,485 C mol⁻¹), ω is the rotation rate (rad s⁻¹), $C_{\text{O}_2}^b$ is the concentration of O₂ in the bulk (1.2×10⁻⁶ mol cm⁻³)[159], D_{O_2} is the diffusion coefficient of O₂ (1.9×10⁻⁵ cm² s⁻¹)[159] and ν is the kinematic viscosity of the electrolyte solution (0.01 cm² s⁻¹)[160].

For the detection of hydroperoxide anion (HO_2^-) formation during the RRDE measurements, the Pt ring electrode was kept at a constant potential of 1.55 V and Au ring at 1.05 V. The ring electrode was electrochemically cleaned before each measurement by applying at least three potential cycles from 0.05 to 1.65 V with Pt or -0.2 to 1.75 V with Au at 100 mV s^{-1} . The collection efficiency (N) of the Au ring was 0.22 [II], Pt ring had N of 0.22 [I,IV,V] or 0.25 [III]. It was determined using the hexacyanoferrate(III) reduction reaction [161].

The RRDE experimental data was used to calculate the peroxide yield and the n values. To calculate the percentage yield of peroxide formation at the disc electrode, Eq. (9) was used:

$$\% \text{HO}_2^- = \frac{\frac{2I_d}{N}}{I_d + \frac{I_r}{N}} \times 100\% \quad (9)$$

where I_d is the disc current, I_r is the ring current, and N is the collection efficiency of the ring electrode. The value of n was calculated from the RRDE results using Eq. (10):

$$n = \frac{4I_d}{I_d + \frac{I_r}{N}} \quad (10)$$

The short-term stability testing of catalyst materials using either RDE or RRDE was carried out by applying 10,000 potential cycles at 200 mV s^{-1} in O_2 -saturated 0.1 M KOH solution. Used potential window for cycling was 1 to 0.5 V [I], 1 to 0.6 V [II-IV] or 1.1 to 0.6 V [V,VI]. The ORR polarisation curves were recorded before and after potential cycling at an electrode rotation rate of 960 [III-V] or 1900 rpm [I,II,VI] from 1 [I-IV] or 1.1 [V,VI] to -0.2V at 10 mV s^{-1} .

5.5 Anion exchange membrane fuel cell tests

For AEMFC tests with N-CDC/CNT material [I], HMT-PMBI was used as both ionomer in the ink and the AEM [133]. The final catalyst loadings were 1.6 mg cm^{-2} for N-CDC/CNT or $0.4 \text{ mg}_{\text{Pt}} \text{ cm}^{-2}$ for Pt/C (weight ratio: 40/60, Fuel-CellStore) on the cathode and $0.6 \text{ mg}_{\text{PtRu}} \text{ cm}^{-2}$ for the PtRu/C (weight ratio: 33/17/50, Tanaka Kikinzoku Kogyo) anode. The area of the fuel cell electrode was 5 cm^2 . The catalyst-coated membranes (CCMs) were soaked in 3 M KOH solution for 2 days before testing. The single-cell fuel cell performance was evaluated using humidified (100% relative humidity (RH)) H_2 and O_2 gases at 60 and 70 °C using 850e Fuel Cell Test System (Scribner Associates Inc.). The flow rates for O_2 and H_2 were 1.0 L min^{-1} without or with 100 kPa back-pressure.

For AEMFC tests with Co-N-CDC/CNT [II], HMT-PMBI ionomer solution and AEM were used. Co-N-CDC/CNT cathode loading was 2 mg cm^{-2} . For comparison, a commercial Pt/C (46 wt%, Tanaka Kikinzoku Kogyo, Japan) was

applied as the cathode catalyst with a loading of $0.4 \text{ mg}_{\text{Pt}} \text{ cm}^{-2}$. Commercial PtRu/C (weight ratio: 50/25/25, Alfa Aesar) was applied as an anode catalyst with $0.6 \text{ mg}_{\text{PtRu}} \text{ cm}^{-2}$ loading. The electrodes together with the HMT-PMBI membrane were immersed in 1 M KOH solution for 24 h before testing. The electrodes and the membrane were pressed together into a 5 cm^2 cell. Greenlight Fuel Cell Test Station (G50 Fuel Cell System, Hydrogenics, Canada) was used to conduct the single-cell AEMFC test. Humidified (100% RH) O_2 (99.95%, Linde Gas) and H_2 (99.999%, Linde Gas) gases at $60 \text{ }^\circ\text{C}$ were fed to the system using a flow rate of 0.3 L min^{-1} . The applied backpressure was 200 kPa.

In the AEMFC tests with M-N-Gra/CNT catalysts [III], Aemion+ membrane (AF2-HLE8-10, Ionomr Innovations Inc., Canada) with $10 \text{ }\mu\text{m}$ thickness and polyimidazolium-based Aemion+ ionomer (Ionomr Innovations Inc., Canada) were employed. Loading of the M-N-Gra/CNT catalyst was 1 to 1.25 mg cm^{-2} . On the anode, loading of $0.5 \text{ mg}_{\text{Pt}} \text{ cm}^{-2}$ ($0.72 \text{ mg}_{\text{PtRu}} \text{ cm}^{-2}$) was used with PtRu/C (Pt = 32.7 wt%, Ru = 16.9 wt%, Tanaka Kikinzoku Kogyo). Comparison MEA had a $0.35 \text{ mg}_{\text{Pt}} \text{ cm}^{-2}$ loading on the cathode and $0.35 \text{ mg}_{\text{Pt}} \text{ cm}^{-2}$ ($0.53 \text{ mg}_{\text{PtRu}} \text{ cm}^{-2}$) on the anode. Prior to the AEMFC test, CCMs were submerged in 3 M KOH for 2 days with a daily refreshment of the solution. Test was performed in the 5 cm^2 cell using Scribner 850e Fuel Cell Test System. No backpressure was applied to the cell, the cell temperature was $70 \text{ }^\circ\text{C}$, RH was 92%, and 0.5 L min^{-1} flow rate was applied with both oxygen and hydrogen.

In the AEMFC tests with M-N-CDC/CNT catalysts [IV], ETFE-based AEM [132] was used. For the anode ink, PtRu/C catalyst (40% Pt and 20% Ru on carbon black, HiSPEC[®] 10000, Alfa Aesar) was combined with an anion exchange ionomer consisting of crosslinked polystyrene functionalized with trimethylbenzylamine groups (Fumatech) and carbon black (Vulcan XC-72) and obtained ionomer-to-catalyst ratio was 20:80. The anode loading was $0.7 \pm 0.05 \text{ mg}_{\text{PtRu}} \text{ cm}^{-2}$. For the cathode inks, the M-N-CDC/CNT catalysts were prepared similarly to the anode ink, but without the addition of carbon black, and with an ionomer-to-catalyst ratio of 30:70. Loading obtained with M-N-CDC/CNT catalysts was 0.71 to 0.75 mg cm^{-2} . The prepared electrodes and the AEM were immersed in 1 M KOH aqueous solution for 1 h, with solution changes after every 20 min. 5 cm^2 cells were tested in an 850E Scribner Associates Fuel Cell test station with hydrogen at the anode and oxygen at the cathode. The best performing cell was then subjected to further analysis by switching the oxidant to CO_2 -free air at the cathode. All the fuel cell tests were performed at a cell temperature of $60 \text{ }^\circ\text{C}$ under gas flows of 1 L min^{-1} and 100 kPa back-pressurisation on both anode and cathode.

In the AEMFC tests with M-N-MPC catalysts [V], the HMT-PMBI membrane with the thickness of $10 \text{ }\mu\text{m}$ and HMT-PMBI-based ionomer were used. The final catalyst loading on the cathode was 2 mg cm^{-2} or $0.4 \text{ mg}_{\text{Pt}} \text{ cm}^{-2}$ for Pt/C (46 wt%, Tanaka Kikinzoku Kogyo, Japan). On the anode, Pt-Ru/C catalyst (50:25:25, Alfa Aesar) loading of $0.8 \text{ mg}_{\text{PtRu}} \text{ cm}^{-2}$ was applied. The electrodes were immersed in 3 M KOH solution 24 h prior to testing. The HMT-PMBI membrane was immersed in 3 M KOH for 96 h before testing with

the fresh solution provided after every 24 h. Greenlight Fuel Cell Test Station was used to conduct the 5 cm² single-cell AEMFC test. Humidified (RH 50%) O₂ and H₂ gases at 60 °C were fed to the system using a flow rate of 1.0 L min⁻¹. The applied backpressure was 200 kPa.

In the AEMFC tests with OMC-based catalysts [VI], Aemion+ membrane (AF2-HLE8-10-X, Ionomr Innovations Inc.) with 10 μm thickness and HMT-PMBI ionomer were used, the cathode loading was 1 mg cm⁻². For the anode, Pt-Ru/C (50:25:25, Alfa Aesar) was combined with AP2-INN8-00-X (Ionomr Innovations Inc.) ionomer solution and used loading was 0.4 mg_{PtRu} cm⁻². Before use, the electrodes and the AEM were soaked in 3 M KOH for one and four days (changed daily), respectively. Greenlight Fuel Cell Test Station was used for AEMFC tests. The cell was fed using 1 L min⁻¹ gas flow rate at 65 °C with the backpressure set for 200 kPa. The relative humidity for O₂ and H₂ gases were optimised during the AEMFC testing with the corresponding values being 60, 75, and 71% RH for CoFe-N-OMC, CoFe-N-OMC/CDC, and CoFe-N-OMC/CNT, respectively.

6. RESULTS AND DISCUSSION

6.1 Nitrogen and/or cobalt doped CDC/CNT composites as catalysts for oxygen reduction

A combination of predominantly microporous CDC together with CNTs was employed as carbon support in articles [I] and [II] with an aim to obtain a novel and feasible porous structure in the catalyst materials. The beneficial properties of respective carbon materials are described in subsection 4.4. For nitrogen doping dicyandiamide (DCDA), melamine (mel), urea [I, II] and cyanamide (CM) [I] were used due to their high N content and wide availability. During the pyrolysis procedure, the exothermic dimerisation of cyanamide towards DCDA occurs at *ca.* 150 °C, followed by the exothermic reaction yielding melamine at 240 °C [162]. When the temperature is above 500 °C, the graphitic carbon nitride (g-C₃N₄) forms from melamine [162, 163]. When urea is heated to 350 °C it decomposes into a mixture of cyanuric acid, ammelide and melamine [164]. Similar to others at 550 °C g-C₃N₄ forms [63, 164, 165]. The graphitic carbon nitride decomposes at 700 °C [163]. During the decomposition of nitrogen precursors and g-C₃N₄, abundant NH₃ and different nitrogen-containing gases are released, which can dope nitrogen into carbon network [165]. As metal precursor, cobalt nitrate was employed [II]. The doping was done via pyrolysis at 800 °C.

6.1.1 Physico-chemical characterisation of N-CDC/CNT and Co-N-CDC/CNT materials

SEM method was employed for the characterisation of the prepared catalyst materials' morphology and the obtained micrographs are presented in Figure 5. From the large-scale micrographs (Figures 5a and 5c) it is visible that just nitrogen doped as well as cobalt and nitrogen doped materials exhibit similar structure with carbon nanotubes surrounding the CDC grains. The CDC grains in the composite vary in size from few hundred nanometres up to several micrometres, and the smaller ones are well wrapped with CNTs. Higher magnification SEM micrographs (Figures 5b and 5d) show that the CNTs in the composite materials vary in diameter and are aligned in different directions with some of them curled or bundled up. The CNT bundles between larger CDC grains create a network of meso- and macroporous areas connecting the microporous CDC. That kind of formation of larger pores is beneficial for the mass transport in the catalyst layer for the AEMFC application. According to the SEM micrographs, the as prepared CDC/CNT-based catalyst materials do not have any noticeable differences, which suggests that the surface morphology does not depend essentially on the nitrogen precursor (urea, melamine, DCDA or cyanamide) used.

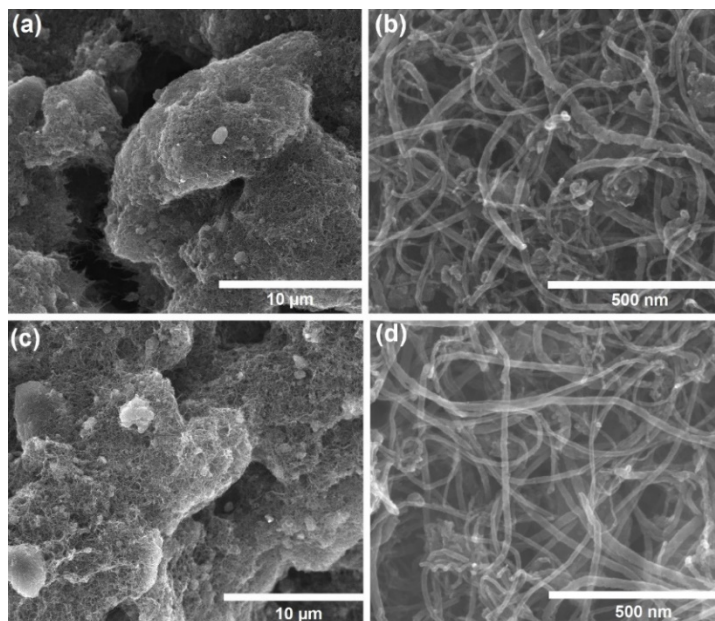


Figure 5. SEM micrographs with lower (a, c) and higher magnification (b, d) for N-CDC/CNT_DCDA (a, c) and Co-N-CDC/CNT_mel (c, d).

The structure of the Co-N-CDC/CNT materials was further investigated by STEM. The results presented in Figure 6 confirm the SEM observations, *i.e.* that the materials consist of a mix of CDC grains and CNTs. Both cobalt and nitrogen were well dispersed in the material. The presence of atomically dispersed cobalt was identified by STEM, as shown in Figure 6c (examples showcased inside the squares).

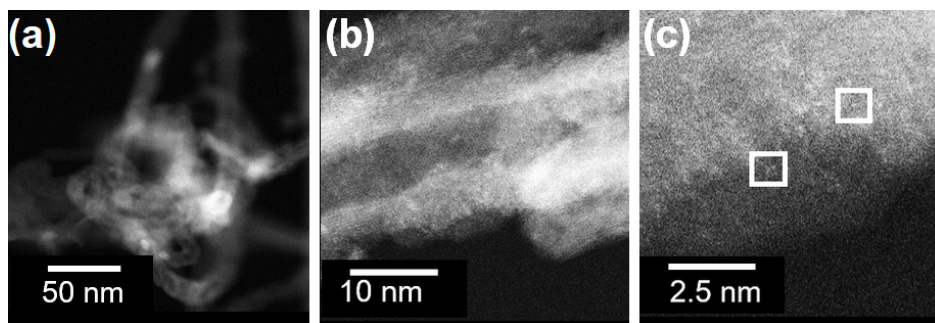


Figure 6. STEM micrographs at different magnifications for Co-N-CDC/CNT_mel.

The textural properties of the CDC/CNT, N-CDC/CNT and Co-N-CDC/CNT catalysts are given in Table 2. The specific surface area (SSA) of N-doped catalysts was around 400–500 m² g⁻¹ with N-CDC/CNT_urea having the highest (470 m² g⁻¹) and N-CDC/CNT_DCDA the lowest SSA value (392 m² g⁻¹). The nondoped CDC/CNT material had a SSA of 322 m² g⁻¹; it should be noted that the initial CDC had a SSA of 1420 m² g⁻¹ (prior to ball-milling) and the SSA of CNTs was about 200 to 400 m² g⁻¹ (according to the data provided by the producer). These results show that ball-milling reduces the SSA of CDC greatly, whereas doping with nitrogen increased the specific surface area of the CDC/CNT catalysts. Similar tendencies to the SSA values can also be seen with total pore volume (V_{tot}) and micropore volume (V_{micro}). After doping with both cobalt and nitrogen (Table 2), the SSA of the catalysts decreased in comparison to just nitrogen-doped material. When melamine or DCDA was used as N precursor, the SSA decreased, but when urea was used, the SSA increased in comparison to CDC/CNT. The differences are not large, which shows that doping with nitrogen and cobalt does not have a big effect on the total SSA. The division of SSA to micro- and mesoporous SSA shows that during the doping new mesopores were formed, especially in case of Co-N-CDC/CNT_mel, which owns its SSA half and half to micro- and mesopores, respectively. For the other two Co-N-CDC/CNT catalysts, the SSA of micropores dominates. The total pore volume slightly increased for all doped composites as compared to the nondoped CDC/CNT material.

Table 2. Textural properties of CDC/CNT, N-CDC/CNT and Co-N-CDC/CNT materials: specific surface area (SSA), micro- and mesoporous SSA (SSA_{micro} , SSA_{meso}), total pore volume (V_{tot}) and micro-pore volume (V_{micro}).

Catalyst	SSA (m ² g ⁻¹)	SSA _{micro} (m ² g ⁻¹)	SSA _{meso} (m ² g ⁻¹)	V_{tot} (cm ³ g ⁻¹)	V_{micro} (cm ³ g ⁻¹)
CDC/CNT	322	243	79	0.37	0.12
N-CDC/CNT_CM	405	300	105	0.46	0.14
N-CDC/CNT_DCDA	392	305	87	0.38	0.14
N-CDC/CNT_urea	470	338	132	0.54	0.16
N-CDC/CNT_mel	408	288	120	0.50	0.14
Co-N-CDC/CNT_DCDA	287	183	104	0.39	0.10
Co-N-CDC/CNT_urea	331	223	108	0.42	0.12
Co-N-CDC/CNT_mel	276	134	142	0.44	0.09

Figure 7a presents the first-order Raman spectra of the Co-N-CDC/CNT catalyst materials. The Raman spectra of all three materials show the presence of two wide bands, which are characteristic to the carbon-based materials. These are the graphitic carbon (G) and disordered carbon (D) peaks located at ~ 1580 and ~ 1350 cm^{-1} , respectively. It should be considered that the spectra are composed of superposition from two different components: relatively narrow G and D peaks from CNTs and much broader G and D bands from CDCs [II]. The G peak is related to the in-plane stretching of the C–C bonds at sp^2 sites and is characteristic for carbon materials. The D peak however becomes visible when there is a disorder in the structure demonstrating that the prepared materials are fairly amorphous [166]. For the quantitative analysis the integrated areas under the D and G peaks were found (I_D and I_G). The I_D/I_G ratios for Co-N-CDC/CNT_urea, Co-N-CDC/CNT_mel and Co-N-CDC/CNT_DCDA samples were 1.25, 1.35 and 1.29, respectively. High I_D/I_G values indicate that there is a significant level of disorder together with defects present in the prepared composite catalyst materials. Similar Raman spectra as well as almost the same I_D/I_G ratios were also obtained for N-CDC/CNT materials [I].

XRD analysis was applied to study the composition and crystallographic structure of the Co-N-CDC/CNT catalysts. The obtained diffraction patterns can be seen in Figure 7b. The largest peak observed at *ca.* $26.5^\circ(2\theta)$ corresponds to the graphitic carbon (002), consisting of a wide 2H and narrow 3R graphite peaks. 2H and 3R are used to characterize the stacking sequence of graphene layers [167]. Additional peaks around 40 to $46^\circ(2\theta)$ can be assigned to graphite, cobalt and cobalt oxide. Thus, the XRD studies suggest the presence of Co-containing nanoparticles in the materials. In addition, traces of ZrO_2 from ball-milling and SiC from the starting carbide were detected. To evaluate the amount of defects in the carbon materials, the ratio of 3R:2H graphite can be used [168]. The 3R:2H ratios of the synthesized catalyst materials were 1:1, 3:2 and 3:2 for Co-N-CDC/CNT_DCDA, Co-N-CDC/CNT_urea and Co-N-CDC/CNT_mel, respectively, which shows that these catalyst materials have a rather high density of structural defects. For all three electrocatalysts, the size of graphite crystallites is below 8 nm and up to a fifth of the carbon mass consists of structurally unlinked graphite layers. By using the half-width of the carbon (002) peak and the Scherrer's method [169], the average thickness of graphite crystallites was found to be 4.9 nm in Co-N-CDC/CNT_DCDA material and 5.2 nm in both Co-N-CDC/CNT_urea and Co-N-CDC/CNT_mel catalysts.

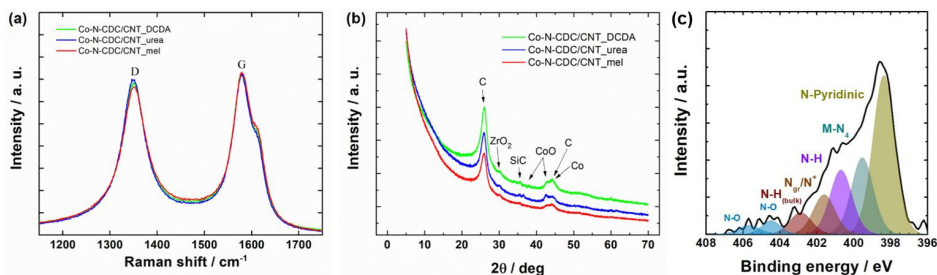


Figure 7. (a) Raman spectra and (b) XRD patterns for Co-N-CDC/CNT catalysts; (c) N1s high-resolution XPS spectra for Co-N-CDC/CNT_mel sample.

XPS analysis was applied in order to examine the surface elemental composition of the catalyst samples. According to the XPS, the unmodified CDC/CNT material consists of carbon and oxygen as expected [I]. The XPS survey spectra for the N-CDC/CNT materials reveal three distinct peaks at 284.8, 532.1 and 400 eV, attributed to the binding energies of C1s, O1s and N1s, respectively, thus indicating that the N-doping of the CDC/CNT composite materials has been successful. The nitrogen content on the surface of N-CDC/CNT materials was around 3 at% [I]. In Co-N-CDC/CNT samples, the nitrogen content was around 2 to 3 at% and the cobalt content was around 0.1 at% [II]. After deconvoluting the N1s peaks of high-resolution XPS spectra into components (example in Figure 7c), it was revealed that in N-CDC/CNT and Co-N-CDC/CNT materials the pyridinic-N is the most prominent N-species present (relative content *ca.* 40%), followed by pyrrolic-N (*ca.* 20%). Such results are expected, as the nitrogen precursors and the pyrolysis conditions were the same with N-CDC/CNT and Co-N-CDC/CNT materials. A major difference, however, is that the metal-doped materials also contain around 20% of metal coordinated to nitrogen (M-N_x) moieties. As discussed in subsection 4.3 then pyridinic-N and M-N_x moieties are deemed to be the most active species towards the oxygen reduction reaction.

Since the XPS method only studies the elemental composition of the surface of the materials, the bulk cobalt content in Co-N-CDC/CNT materials was determined by ICP-MS. According to the ICP-MS results, the cobalt content was in the range from 2.4 to 3.1 wt% in all Co-N-CDC/CNT catalyst materials. The bulk Co content is also close to the nominal value calculated from the amount of Co salt added in the synthesis. In addition to cobalt, 0.5 wt% of zirconium was also detected in all three samples, which is a residue from the ball-milling procedure, where ZrO₂ balls were used.

6.1.2 Oxygen reduction reaction on N-CDC/CNT and Co-N-CDC/CNT catalysts

Firstly, the electrocatalytic activity of the N-CDC/CNT catalysts towards the ORR was studied in 0.1 M KOH solution (Figure 8, Table 3). The undoped reference material CDC/CNT showed the lowest ORR activity with the onset potential of O₂ reduction (E_{onset} , defined as the potential at which the ORR current density reaches -0.1 mA cm^{-2}) being 0.80 V vs RHE and the polarisation curve exhibited two reduction waves. The shape of the RDE polarisation curves for oxygen reduction was rather similar for all four nitrogen-doped composite catalysts and only a single reduction wave was observed. The onset potential of N-CDC/CNT_CM was slightly more negative ($E_{\text{onset}}=0.87 \text{ V}$) compared to N-CDC/CNT_DCDA, N-CDC/CNT_mel and N-CDC/CNT_urea with all three having the same E_{onset} value of 0.90 V. The half-wave potential ($E_{1/2}$) values for the catalysts were between 0.74 and 0.77 V (Table 3). These results show that the prepared N-CDC/CNT catalysts have a rather high electrocatalytic activity towards the ORR, but are slightly inferior to commercial Pt/C ($E_{\text{onset}}=0.96 \text{ V}$; $E_{1/2}=0.82 \text{ V}$).

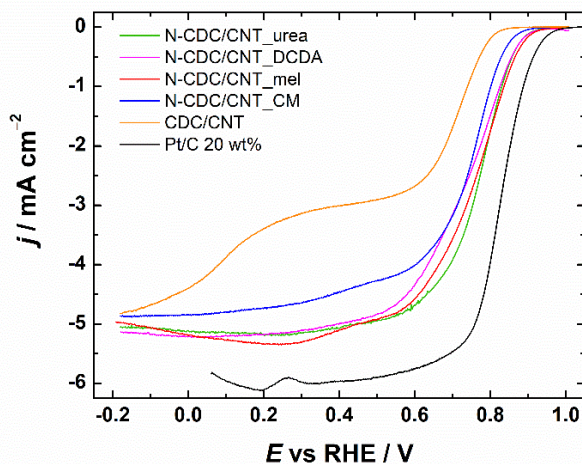


Figure 8. RDE voltammetry curves for ORR on CDC/CNT, N-CDC/CNT catalysts and commercial Pt/C in O₂-saturated 0.1 M KOH solution ($\omega=1900 \text{ rpm}$, $\nu=10 \text{ mV s}^{-1}$, catalyst loading 0.1 mg cm^{-2}).

Similarly to the N-CDC/CNT materials, the initial assessment of the ORR activity of Co-N-CDC/CNT materials was done using the RDE method in 0.1 M KOH solution with the results shown in Figure 9 and Table 3. The shape of the RDE polarisation curves for oxygen reduction was rather similar for all Co-N-CDC/CNT catalysts and only a single reduction wave was observed with a

clearly defined diffusion-limited current plateau formed (Figure 9a). The ORR onset potential of Co-N-CDC/CNT_DCDA was slightly more negative compared to those of Co-N-CDC/CNT_mel and Co-N-CDC/CNT_urea both having the same E_{onset} value of 0.95 V. The half-wave potential for O₂ reduction on Co-N-CDC/CNT catalysts was 0.82 V. These results were comparable to that of commercial Pt/C and superior when compared to N-CDC/CNT materials (Figure 8, Table 3), which suggests that adding transition metal, herein cobalt, indeed improves the electrocatalytic activity of materials.

To study the ORR pathway on the N-CDC/CNT and Co-N-CDC/CNT catalyst materials, the RDE polarisation curves were recorded at different electrode rotation rates (example in Figure 9b) and the data was analysed using Koutecky-Levich (K-L) equation (Eq. 8). The K-L plots together with the potential dependence of the n value is shown in Figure 9c. The intercept of extrapolated K-L lines (Figure 9c, [I,II]) is near zero, thus indicating that the electroreduction of O₂ is under diffusion control in a broad range of potentials for doped CDC/CNT materials. The value of n is four for Co-N-CDC/CNT_mel and Co-N-CDC/CNT_DCDA electrocatalysts, but slightly lower in case of Co-N-CDC/CNT_urea and N-CDC/CNT materials. These results show that the electroreduction of O₂ proceeds predominantly via direct 4e⁻ pathway or 2-step 2e⁻ pathway.

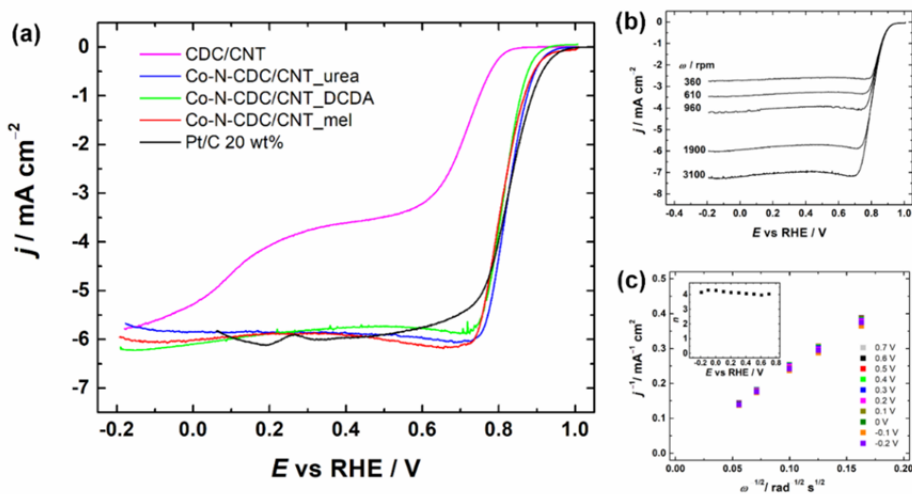


Figure 9. (a) Comparison of ORR polarisation curves recorded in O₂ saturated 0.1 M KOH solution on Co-N-CDC/CNT, CDC/CNT, and Pt/C catalysts ($v=10 \text{ mV s}^{-1}$, $\omega=1900 \text{ rpm}$, catalyst loading 0.2 mg cm^{-2}). (b) RDE voltammetry curves for the ORR on Co-N-CDC/CNT_mel catalyst at various rotation rates ($v=10 \text{ mV s}^{-1}$). (c) Koutecky-Levich plots for the ORR derived from the RDE data in (b) and the n value as a function of potential is given in the inset.

Table 3. The ORR parameters determined from RDE data for CDC/CNT, N-CDC/CNT (loading 0.1 mg cm^{-2}) and Co-N-CDC/CNT (loading 0.2 mg cm^{-2}) electrocatalyst materials in 0.1 M KOH solution.

Catalyst	$E_{\text{onset}}/\text{V}$	$E_{1/2}/\text{V}$	n
CDC/CNT	0.80	<i>n.d.</i>	2.5–3.5
N-CDC/CNT_urea	0.90	0.77	3.4–3.9
N-CDC/CNT_DCDA	0.90	0.74	3.6–3.9
N-CDC/CNT_mel	0.90	0.76	3.7–4.0
N-CDC/CNT_CM	0.87	0.74	3.4–4.0
Co-N-CDC/CNT_urea	0.95	0.82	3.7–3.9
Co-N-CDC/CNT_DCDA	0.91	0.82	4.0
Co-N-CDC/CNT_mel	0.95	0.82	4.0

For practical applications it is important that the properties of the catalyst remain stable for a long time period. A short-term stability test in alkaline media was conducted using N-CDC/CNT_mel and Co-N-CDC/CNT_mel catalyst and the results can be seen in Figure 10. After 10,000 potential cycles, the ORR performance remained virtually the same for both materials. Similar good stability is expected also for the other prepared catalyst materials in alkaline media due to their similar morphologies and compositions.

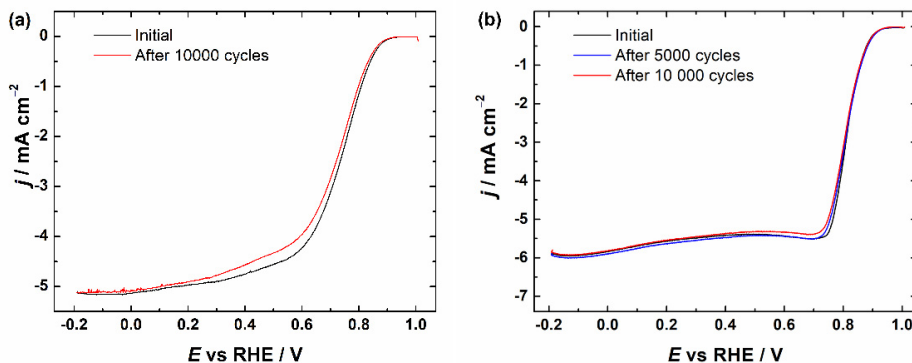


Figure 10. RDE voltammetry curves for ORR on (a) N-CDC/CNT_mel and (b) Co-N-CDC/CNT_mel catalyst materials in O_2 -saturated 0.1 M KOH solution before and after 10,000 potential cycles ($\omega=1900 \text{ rpm}$, $\nu=10 \text{ mV s}^{-1}$).

6.1.3 Anion exchange membrane fuel cell test with N-CDC/CNT and Co-N-CDC/CNT catalysts

As N-CDC/CNT_mel and Co-N-CDC/CNT_mel exhibited very good ORR activity as well as excellent stability, then they were employed as cathode catalysts in the AEMFC together with PtRu/C anode and HMT-PMBI anion exchange membrane [133]. The single-cell AEMFC performance of N-CDC/CNT_mel is shown in Figure 11a and it shows good performance by obtaining a peak power density (P_{\max}) of 260 mW cm^{-2} at $60 \text{ }^\circ\text{C}$ and 310 mW cm^{-2} at $70 \text{ }^\circ\text{C}$, which is among the highest AEMFC power densities for MEAs using metal-free cathode catalysts (Table 1). The single-cell AEMFC performance with Co-N-CDC/CNT_mel on the cathode is shown in Figure 11b and that catalyst exhibits impressive AEMFC performance by obtaining current density of 206 mA cm^{-2} at 0.8 V and the peak power density of 577 mW cm^{-2} at $60 \text{ }^\circ\text{C}$. This shows that the Co-N-CDC/CNT material surpasses the electrocatalytic activity of N-CDC/CNT material quite significantly, thus proving that in order to obtain excellent and Pt-like performance in the AEMFC, the incorporation of transition metal is crucial in addition to the nitrogen doping. The P_{\max} value places the Co-N-CDC/CNT_mel catalyst among the best cobalt-based cathode catalysts to date used in an AEMFC (Table 1). The excellent performance of Co-N-CDC/CNT_mel can be attributed to the presence of ORR-active sites (pyridinic-N, M-N_x) as well as feasible porous structure, as it exhibits relatively large mesoporous network in addition to the micropores, which is important for the AEMFC application [170].

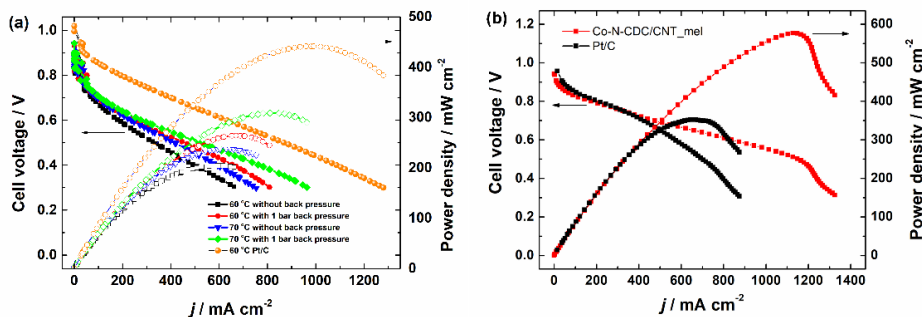


Figure 11. Polarisation and power density curves for H₂/O₂ AEMFCs using the HMT-PMBI anion exchange membrane and ionomer. Anode catalyst: PtRu/C and cathode catalyst (a) N-CDC/CNT_mel or (b) Co-N-CDC/CNT (60 °C, 200 kPa backpressure).

6.2 Transition metal and nitrogen doped graphene/CNT composites as catalysts

As the cobalt and nitrogen doped CDC/CNT composites showed excellent performance, described in subsection 6.1, then this doping method with melamine as nitrogen source was utilised for incorporating nitrogen into graphene-like material and carbon nanotubes composite (Gra/CNT) [III]. This support should similarly to CDC/CNT give a novel and possibly beneficial porous structure to the final catalyst materials. In addition to nitrogen doping with melamine as precursor, transition metals were also added as they were proven to be useful in subsection 6.1 and [II]. As dopants, cobalt, iron and both of them were incorporated to study the effect of different metal additives on the ORR performance. The synthesis was done via pyrolysis, yielding three catalyst materials: Co-N-Gra/CNT, Fe-N-Gra/CNT and CoFe-N-Gra/CNT.

6.2.1 Physico-chemical characterisation of M-N-Gra/CNT materials

The morphology of three prepared catalyst materials was studied using scanning electron microscopy (SEM) with obtained micrographs shown in Figure 12. Lower magnification images (Figure 12a, [III]) indicate that all three materials exhibit very similar structures with CNTs surrounding and connecting the graphene nanoplatelet agglomerates, which seem to be varied in size. Higher magnification images (Figure 12b, [III]) give a better overview of the carbon composite network: the CNTs are aligned in different directions with the formation of clusters; the graphene-like material however remains in the agglomerate form and is covered well with the CNTs. All-in-all, no noticeable differences in the morphology of the materials prepared using different transition metals can be seen. The morphology seems also somewhat similar to that of CDC/CNT composite described in subsection 6.1 (Figure 5).

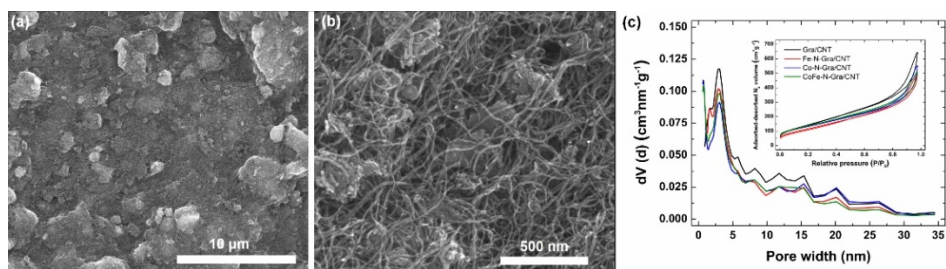


Figure 12. (a, b) SEM micrographs of CoFe-N-Gra/CNT material; (c) pore size distributions and N₂ adsorption-desorption isotherms (the inset) for Gra/CNT and M-N-Gra/CNT materials.

N_2 physisorption studies were conducted to analyse the textural properties of the prepared catalyst materials with the results shown in Figure 12c and Table 4. All materials had similarly shaped isotherms (Figure 12c inset), which corresponds to a combination of type I and III with H3 hysteresis according to IUPAC [171]. Such N_2 adsorption-desorption isotherms are characteristic of micro-mesoporous materials with a relatively small proportion of micropores. The Gra/CNT composite material had a specific surface area of $511 \text{ m}^2 \text{ g}^{-1}$, which is expected as the SSAs of pure graphene nanoplatelets and CNTs are 750 and $200\text{--}400 \text{ m}^2 \text{ g}^{-1}$, respectively (according to the product specification sheets). Overall, after the doping, a slight decrease in the SSA can be observed. With cobalt incorporation, new values calculated are $470 \text{ m}^2 \text{ g}^{-1}$ and $484 \text{ m}^2 \text{ g}^{-1}$. At the same time, a larger decrease to $415 \text{ m}^2 \text{ g}^{-1}$ occurred for Fe-N-Gra/CNT catalyst. The latter also exhibited a slightly lower overall pore volume (V_{tot}) and micropore volume (V_{micro}) than the other two catalyst materials. In general, all three M-N-C type materials have rather similar textural properties, especially considering the pore size distributions (Figure 12c), which indicates the presence of a significant amount of smaller mesopores (maximum peak at *ca.* 3 nm), but also a notable amount of larger mesopores in the catalyst materials. This highly porous structure with pores of various sizes could be beneficial in the fuel cell application.

Table 4. Specific surface area (SSA), total pore volume (V_{tot}), and micropore volume (V_{micro}) for Gra/CNT and M-N-Gra/CNT samples.

Catalyst material	SSA ($\text{m}^2 \text{ g}^{-1}$)	V_{tot} ($\text{cm}^3 \text{ g}^{-1}$)	V_{micro} ($\text{cm}^3 \text{ g}^{-1}$)
Gra/CNT	511	0.87	0.10
Fe-N-Gra/CNT	415	0.67	0.07
Co-N-Gra/CNT	470	0.74	0.11
CoFe-N-Gra/CNT	484	0.72	0.12

The structure of the prepared catalyst materials was further investigated using Raman spectroscopy and XRD. The Raman spectra (Figure 13a) of Gra/CNT and M-N-Gra/CNT catalyst materials are similar and typical of carbon materials with a presence of broadened graphitic carbon (G, $\sim 1590 \text{ cm}^{-1}$) and disordered carbon (D1, $\sim 1350 \text{ cm}^{-1}$) peaks. The width of D1 and G bands, which increase with the degree of disorder in the graphitic lattice [172], were more or less the same in all samples with a value of 66 and 76 cm^{-1} , respectively. Rather narrow peaks suggest that materials have graphitic domains, while the high D1 peak indicates the presence of disorder and defects [166]. The latter is also proved by the relatively high $I_{\text{D1}}/I_{\text{G}}$ ratios of 1.32, 1.25, 1.33, and 1.5 for Gra/CNT, Fe-N-Gra/CNT, Co-N-Gra/CNT, and CoFe-N-Gra/CNT, respectively.

The crystallographic structure as well as the composition of the catalyst materials were studied using the XRD analysis (Figure 13b). Among collected XRD patterns, the most prominent peaks are graphitic carbon peaks at $26.2\text{--}26.6^\circ$ (20) and at $41\text{--}46^\circ$ (20), consisting of wide 2H and narrow 3R graphite

peaks, which characterise the different stacking sequences of graphene layers [167]. In all samples the content of 3R carbons was higher than that of 2H and this high 3R content in a combination with a wide first peak (26.2–26.6°) with a visible shoulder at lower angles suggests that materials have a disordered structure with some unlinked graphitic layers [168]. In addition to the graphitic carbon, small peaks corresponding to the transition metals (Fe, Co, and CoFe alloy) can be seen around 40–46° (2 θ) on M-N-Gra/CNT patterns, however, the determination of specific metal compounds is difficult due to the overlap with the second carbon peak as well as a low content.

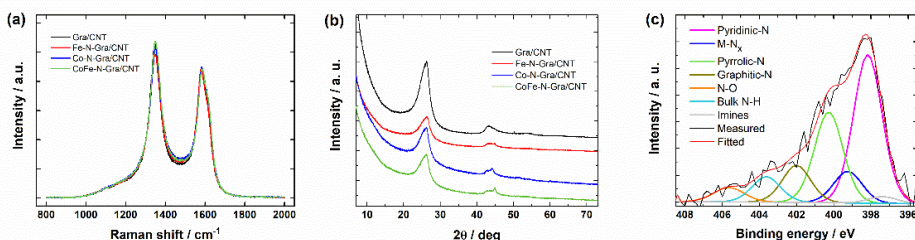


Figure 13. (a) Raman spectra and (b) XRD patterns for Gra/CNT and M-N-Gra/CNT materials; (c) N1s high-resolution XPS spectra for CoFe-N-Gra/CNT sample.

The chemical composition of the materials was studied using the XPS, SEM-EDX and MP-AES techniques. According to the XPS results [III], the M-N-Gra/CNT catalysts contain C, O, N, and the added metals (Fe, Co, or both) with the surface nitrogen content being between 1.5 and 1.9 at%. The transition metal signal in the XPS analysis is rather weak, however, according to the SEM-EDX all three M-N-Gra/CNT materials contain around 5 wt% of nitrogen and *ca.* 2.5 wt% of transition metal(s) as was also intended from the catalyst synthesis. Similar metal contents were also found in bulk materials using the MP-AES method. Overall, the process of doping with nitrogen and transition metal(s) via pyrolysis has been a success with all of the M-N-Gra/CNT materials having a similar content of dopants.

In addition to knowing the contents of dopants, it is important to know in what form they are, especially nitrogen. For the latter, the high-resolution XPS spectra in the N1s region were collected for M-N-Gra/CNT materials and then deconvoluted into seven peaks as shown in Figure 13c. The nitrogen configuration in all three M-N-Gra/CNT materials is very similar, meaning that the doping with melamine has had a similar effect and it does not depend on the transition metal employed. The most prominent N-species in M-N-Gra/CNT materials was pyridinic-N with relative content above 40%, followed by N-H (includes pyrrolic-N and hydrogenated pyridine) at *ca.* 25%, graphitic-N and metal-coordinated N-species (M-N_x) both took up *ca.* 10%. Similar high contents of pyridinic-N and pyrrolic-N were also obtained in N-CDC/CNT and Co-N-CDC/CNT materials [I,II] in subsection 6.1, which also showed high ORR activity.

6.2.2 Oxygen reduction reaction on M-N-Gra/CNT catalysts

For the assessment of ORR activity of the catalysts, the RDE method was used in 0.1 M KOH solution, the results are presented in Figure 14a and Table 5. The undoped Gra/CNT material has the lowest electrocatalytic activity, while the nitrogen and transition metal doped M-N-Gra/CNT materials exhibit significantly improved electrocatalytic properties, close to that of state-of-the-art Pt/C ($40 \mu\text{g}_{\text{Pt}} \text{cm}^{-2}$) catalyst. All three M-N-Gra/CNT materials had the same $E_{1/2}$ values of 0.81 V, which is only 2 mV lower than that of Pt/C ($E_{1/2}=0.83 \text{ V}$; $E_{\text{onset}}=0.98 \text{ V}$). The onset potentials were also very similar for all M-N-Gra/CNT materials.

The obtained K-L plots from series of RDE polarisation curves (Figure 14b) together with the dependence of n on the potential are shown in Figure 14c. The intercept of extrapolated K-L lines is close to zero for M-N-Gra/CNT materials, but slightly off zero for Gra/CNT [III]. This indicates that the electroreduction of O_2 on M-N-Gra/CNT catalysts is predominantly under diffusion control in a broad range of potentials and that the kinetic limitations are reduced via doping the Gra/CNT composite material. The value of n was 4 for all three M-N-Gra/CNT materials, but ranged from 3.2 to 3.9 for Gra/CNT (Table 5).

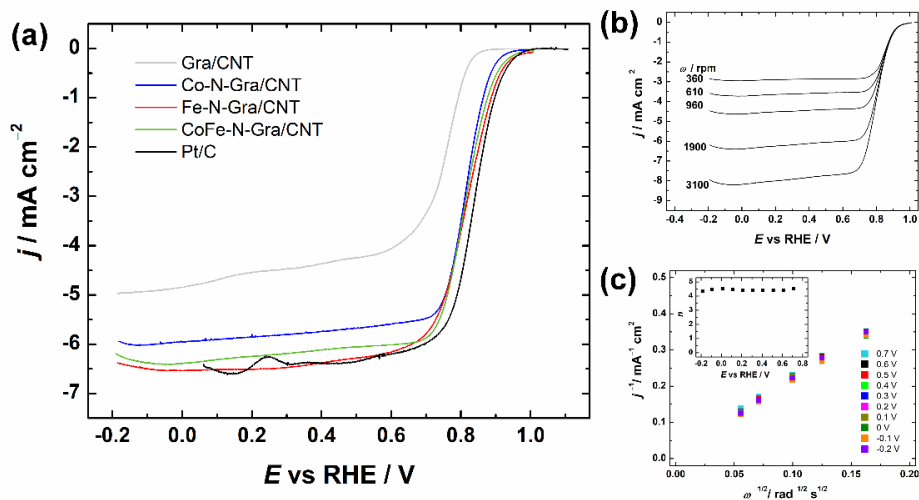


Figure 14. (a) Comparison of the ORR polarisation curves recorded in O_2 -saturated 0.1 M KOH solution on Gra/CNT, M-N-Gra/CNT, and Pt/C catalysts ($v=10 \text{ mV s}^{-1}$, $\omega=1900 \text{ rpm}$). (b) RDE voltammetry curves for the ORR on CoFe-N-Gra/CNT catalyst at various rotation rates ($v=10 \text{ mV s}^{-1}$). (c) Koutecky–Levich plots for the ORR derived from the RDE data in (b) and the n value as a function of potential is given in the inset.

Table 5. The ORR parameters determined from RDE data for Gra/CNT and M-N-Gra/CNT (loading 0.2 mg cm⁻²) electrocatalyst materials in 0.1 M KOH solution.

Catalyst	$E_{\text{onset}}/\text{V}$	$E_{1/2}/\text{V}$	n
Gra/CNT	0.85	0.75	3.2–3.9
Co-N-Gra/CNT	0.93	0.81	4.0
Fe-N-Gra/CNT	0.98	0.81	4.0
CoFe-N-Gra/CNT	0.96	0.81	4.0

As all three M-N-Gra/CNT materials exhibited high ORR activity, then they all underwent a short-term stability test by applying 10,000 potential cycles between 1.0 and 0.6 V at 200 mV s⁻¹ and recording the ORR polarisation curve before and after the cycling at 960 rpm. For a better assessment of the possible changes in the material during stability testing, the rotating ring-disc electrode (RRDE) method was employed herein – in addition to changes within the polarisation curve, changes in a peroxide yield can be discovered with this method. The stability test results (Figure 15a–c) indicate that all M-N-Gra/CNT materials exhibit excellent stability with no changes of the onset and half-wave potentials after 10,000 potential cycles. The respective yield of hydroperoxide anion (HO₂⁻) formation and the number of electrons transferred per O₂ molecule are shown in Figures 15d–f. The yield of HO₂⁻ increased only by up to 5% after potential cycling for Fe-N-Gra/CNT and Co-N-Gra/CNT materials at potentials higher than 0.5 V.

While the Fe-N-Gra/CNT, Co-N-Gra/CNT, and CoFe-N-Gra/CNT catalysts all exhibited a desirable ORR activity and stability after potential cycling, the most significant differences came from the yield of HO₂⁻ and corresponding n values. Initially, Fe-N-Gra/CNT had the lowest %HO₂⁻ of 6 to 10%, followed by CoFe-N-Gra/CNT at 9 to 18%, and lastly Co-N-Gra/CNT with 16 to 25%. The corresponding n values were 3.8–3.9, 3.5–3.7, and 3.6–3.8 for Fe-N-Gra/CNT, Co-N-Gra/CNT, and CoFe-N-Gra/CNT, respectively. These results suggest that the ORR on M-N-Gra/CNT electrocatalysts proceeds most probably via a 2×2e⁻ pathway, where hydroperoxide anions are formed as an intermediate and then further reduced to OH⁻. It is also evident that the HO₂⁻ yield depends on the metal additive used – cobalt has the highest yield and iron the lowest, which was also discussed in subsection 4.3.2.

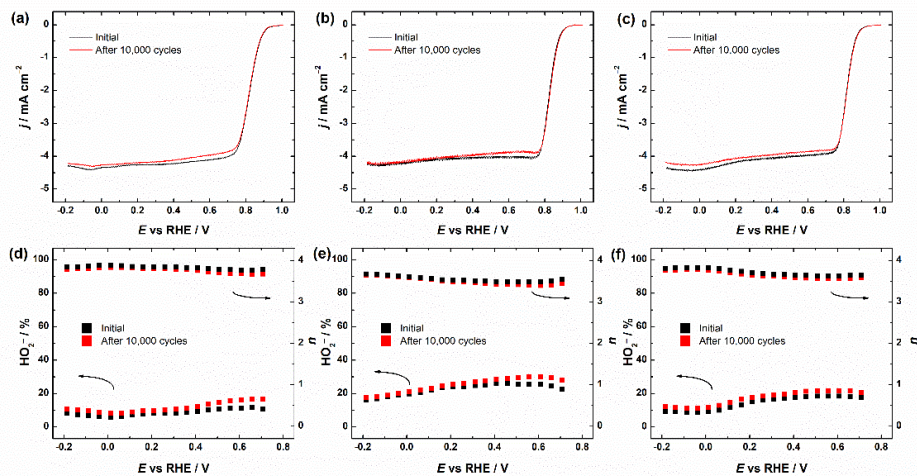


Figure 15. (a–c) ORR polarisation curves and (d–f) the percentage yield of HO_2^- formation and the value of n as a function of potential for (a, d) Fe-N-Gra/CNT, (b, e) Co-N-Gra/CNT, and (c, f) CoFe-N-Gra/CNT catalyst materials in O_2 -saturated 0.1 M KOH solution before and after 10,000 potential cycles ($\omega=960$ rpm, $v=10$ mV s^{-1}).

6.2.3 Anion exchange membrane fuel cell test with M-N-Gra/CNT catalysts

Since prepared M-N-Gra/CNT materials exhibited excellent electrocatalytic activity toward the ORR, the single-cell AEMFC tests were conducted (Figure 16) to evaluate their potential as a cathode catalyst in the fuel cell as well as to see whether the difference in metal additive has an effect on the AEMFC performance. As can be seen from Figure 16a, the CoFe-N-Gra/CNT material as the cathode catalyst displayed superior performance among all non-PGM catalysts tested as well as almost identical performance to the commercially utilised Pt/C. The CoFe-N-Gra/CNT catalyst reached a current density of 830 mA cm^{-2} at 0.6 V, which is only about 10% lower than that of Pt/C. Cathodes containing Fe-N-Gra/CNT and Co-N-Gra/CNT showcased a satisfactory performance with current density being *ca.* 570 mA cm^{-2} at 0.6 V, however mass transfer regions at a higher current density are different for them as Fe-N-Gra/CNT exhibits a sharp decrease. The AEMFC with CoFe-N-Gra/CNT and Pt/C cathodes achieved almost equal maximum power densities of 638 and 640 mW cm^{-2} , respectively. With Fe-N-Gra/CNT based cathode the P_{max} value was 364 mW cm^{-2} and with Co-N-Gra/CNT 447 mW cm^{-2} . Such peak power density values indicate that the M-N-Gra/CNT materials are rather active cathode catalysts in the AEMFC (Table 1). When comparing these results to those described in subsection 6.1, then Co-N-CDC/CNT outperforms Co-N-Gra/CNT, however, it should be noted that herein [III] lower loading was employed and the membrane was different (Aemion+ [III], further development of HMT-PMBI [I, II]). However, the performance of CoFe-N-Gra/CNT material

indicates that bimetallic composition is beneficial for the ORR as suggested in subsection 4.3.2.

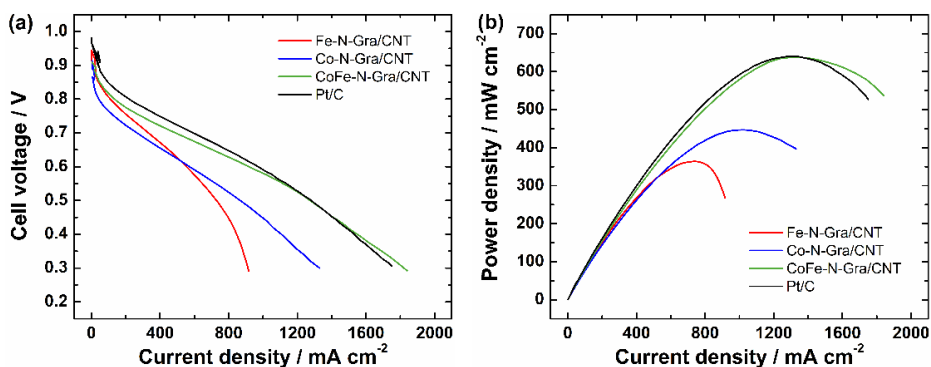


Figure 16. (a) Polarisation and (b) power density curves for H₂/O₂ AEMFCs. Cathode catalyst: M-N-Gra/CNT or Pt/C; anode catalyst: Pt-Ru/C and AEM: Aemion+. T=70 °C.

6.3 Transition metal and nitrogen doped CDC/CNT composites as catalysts

As in articles [I] and [II] the CDC/CNT composites showed feasible porous structure, resulting in very good ORR activity and AEMFC performance (subsection 6.1), then this composite was chosen as carbon support for this work as well. Similarly as in article [III] described in subsection 6.2, the effect of different transition metal additives was studied herein as well [IV], so materials containing iron, cobalt or both were prepared. In this work, the metal content was lowered to *ca.* 1 wt% to make catalysts more sustainable. Metal acetates together with 1,10-phenanthroline as nitrogen source were used as dopants for the CDC/CNT composites as these precursor materials are known to form complexes, thus potentially leading to the formation of M-N_x species in the final catalyst materials [77, 78]. The resulting catalysts are Fe-N-CDC/CNT, Co-N-CDC/CNT and CoFe-N-CDC/CNT [IV].

6.3.1 Physico-chemical characterisation of M-N-CDC/CNT materials

According to the SEM micrographs shown in Figure 17, the morphology is very similar to that of the materials characterised in subsection 6.1 with CDC/CNT composites (Figure 5). Materials have rather homogenous distribution of CNTs and CDC grains, which vary in size. The CNTs have formed a network between the microporous CDC grains and thus give the material both meso- and macropores. Additionally, the CNTs are covering the CDC particles and are

themselves aligned in different directions, with some of them being bundled or curled up (Figure 17d–f). As expected, no noticeable differences in the morphology of the materials prepared using different transition metals can be seen.

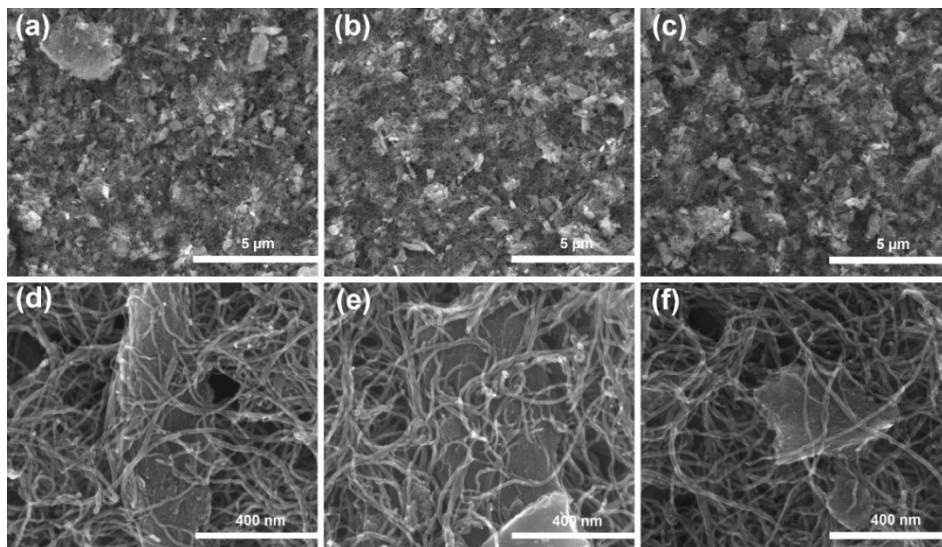


Figure 17. SEM micrographs with lower (a–c) and higher magnification (d–f) for Fe-N-CDC/CNT (a, d), Co-N-CDC/CNT (b, e) and CoFe-N-CDC/CNT (c, f).

The results of N_2 physisorption studies of prepared M-N-CDC/CNT materials are summarised in Table 6. The SSA of all catalyst materials was around $400 \text{ m}^2 \text{ g}^{-1}$. All three M-N-CDC/CNT catalyst materials exhibit similar porous structure with the total pore volume being $0.5\text{--}0.6 \text{ cm}^3 \text{ g}^{-1}$ and micropore volume around $0.1 \text{ cm}^3 \text{ g}^{-1}$, which means that different metal dopants have a similar effect on the textural properties of the CDC/CNT-based materials. The N_2 physisorption results indicate that the M-N-CDC/CNT materials have both micro- and mesopores present, which could be beneficial in the AEMFC application [170].

Table 6. Specific surface area (SSA), total pore volume (V_{tot}) and micropore volume (V_{micro}) for M-N-CDC/CNT samples.

Catalyst material	SSA ($\text{m}^2 \text{ g}^{-1}$)	V_{tot} ($\text{cm}^3 \text{ g}^{-1}$)	V_{micro} ($\text{cm}^3 \text{ g}^{-1}$)
Fe-N-CDC/CNT	404	0.58	0.11
Co-N-CDC/CNT	393	0.53	0.09
CoFe-N-CDC/CNT	399	0.58	0.12

The elemental composition of the M-N-CDC/CNT materials was studied using MP-AES and XPS methods. The results are presented in Table 7. According to MP-AES, the overall metal content (Fe or Co) was in the range of 1.0–1.2 wt% in all three materials, which is close to the expected value calculated from the amount of metal acetates added in the synthesis of the catalysts. It should be noted that the catalyst materials also had some residual metals (not from doping), which originate from the CNTs' growing substrates and are located mainly inside the carbon nanotubes. The XPS results (Table 7) indicate that in the case of all three samples C, N, O, and Zr, as well as the added respective metals (Fe, Co, or both), are present on the surface. The nitrogen content was 1.1 at% for Fe-N-CDC/CNT and 1.4 at% for Co-N-CDC/CNT and CoFe-N-CDC/CNT, indicating that the doping with nitrogen has been successful for all the prepared catalyst materials.

Table 7. Surface elemental composition of M-N-CDC/CNT materials as determined by XPS and bulk metal composition as determined by MP-AES.

Catalyst	Surface elemental composition (at%)						Bulk metal composition (wt%)	
	C	O	N	Zr	Fe	Co	Fe	Co
Fe-N-CDC/CNT	96.1	2.7	1.1	0.1	0.1	-	0.981±0.008	0.049±0.001
Co-N-CDC/CNT	95.9	2.4	1.4	0.1	-	0.2	0.146±0.004	1.084±0.012
CoFe-N-CDC/CNT	95.5	2.6	1.4	0.1	0.1	0.1	0.620±0.017	0.608±0.008

To determine the type of N centres, detailed XPS spectra in the N1s region were deconvoluted into six peaks corresponding to various N species (Figure 18), the relative concentrations of these are shown in Table 8. In all three samples, hydrogenated-N (N-H; includes pyrrolic-N and hydrogenated pyridine), pyridinic-N and metal-coordinated N (M-N_x) were the most prominent species.

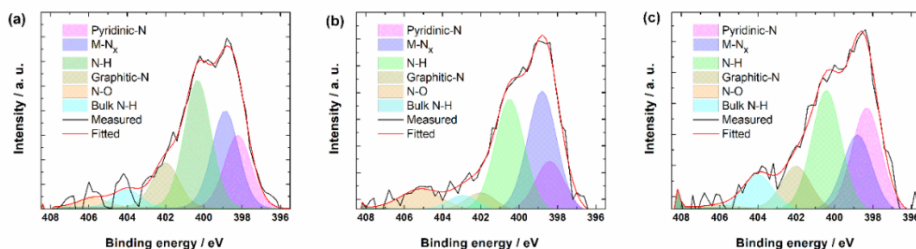


Figure 18. N1s high-resolution X-ray photoelectron spectra for (a) Fe-N-CDC/CNT, (b) Co-N-CDC/CNT and (c) CoFe-N-CDC/CNT samples.

Table 8. Relative concentration (%) of N species on M-N-CDC/CNT materials by XPS analysis.

N species	Fe-N-CDC/CNT	Co-N-CDC/CNT	CoFe-N-CDC/CNT
Pyridinic-N	20.0	14.6	27.1
M-N _x	25.7	35.0	20.0
N-H	34.3	32.8	31.4
Graphitic-N	12.4	5.1	11.4
N-O	2.9	8.0	0.7
Bulk N-H	4.8	4.4	9.3

6.3.2 Oxygen reduction reaction on M-N-CDC/CNT catalysts

In order to give an initial assessment of the prepared catalyst materials' electro-catalytic activity towards the ORR, the RRDE method was employed in O₂-saturated 0.1 M KOH aqueous solution at 960 rpm with results shown in Figure 19–20, and Table 9. For all three M-N-CDC/CNT catalyst materials, the shape of the polarisation curve was similar: a single oxygen reduction wave along with a clearly defined diffusion-limited current plateau (Figure 19a). The E_{onset} and $E_{1/2}$ values of O₂ reduction were high while showing slight dependence on the metal additive and increased in order of Co-N-CDC/CNT, CoFe-N-CDC/CNT and Fe-N-CDC/CNT (Table 9). As reference catalysts, both undoped CDC/CNT materials and commercial Pt/C were also tested. It is clear that doping with nitrogen and transition metals is useful, since the CDC/CNT composite exhibits two O₂ reduction waves and lower E_{onset} of 0.80 V. The commercial Pt/C catalyst (loading of 0.08 mg_{Pt} cm⁻²), showed slightly better ORR performance with the E_{onset} and $E_{1/2}$ values being 1.00 and 0.89 V, respectively.

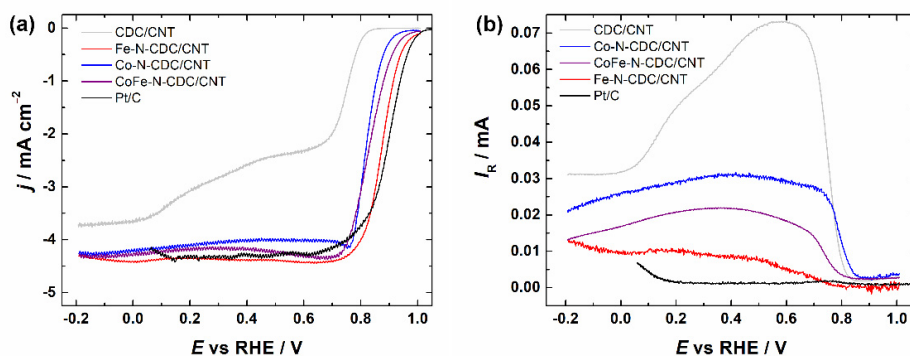


Figure 19. RRDE results for the ORR in O₂-saturated 0.1 M KOH solution on CDC/CNT, M-N-CDC/CNT, and Pt/C catalysts. (a) disc current densities and (b) ring currents. $\omega=960$ rpm, $\nu=10$ mV s⁻¹.

These results show that the catalyst of low cobalt content, Co-N-CDC/CNT, has the lowest electrocatalytic activity and the addition of iron (CoFe-N-CDC/CNT) improves the onset potential. The Fe-N-CDC/CNT material itself showed the best performance in terms of both E_{onset} and $E_{1/2}$.

To study the ORR pathway, the respective ring currents were also collected (Figure 19b). The yield of HO_2^- formation and n as a function of potential are presented in Figure 20 and Table 9. The results show that the undoped CDC/CNT material has the highest peroxide formation, which reaches 90% at higher potentials and decreases to 40% at lower potentials. The commercial Pt/C catalyst has the lowest HO_2^- yield of around 2%, which suggests a $4e^-$ ORR pathway to occur. In case of M-N-CDC/CNT materials, as expected, the cobalt-based material (Co-N-CDC/CNT) produced the highest amount of HO_2^- (20–30%), which further confirms that indeed cobalt facilitates peroxide production [86]. The RRDE results also show that the aim of reducing the peroxide production of cobalt-based materials by making bimetallic catalysts has been successful with the HO_2^- yield being 15–20% in case of CoFe-N-CDC/CNT. The Fe-N-CDC/CNT catalyst showed the smallest peroxide formation (around 10%). The n values were around 3.5, 3.7, and 3.9 for Co-N-CDC/CNT, CoFe-N-CDC/CNT, and Fe-N-CDC/CNT, respectively. These results indicate that the electroreduction of O_2 on M-N-CDC/CNT catalyst materials proceeds mostly via a $2 \times 2e^-$ pathway, where peroxide forms as an intermediate, which is then further reduced to OH^- [173].

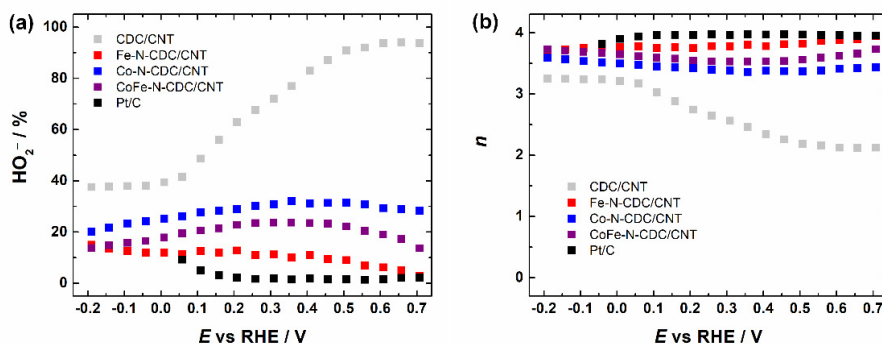


Figure 20. (a) The yield of HO_2^- formation and (b) the value of n as a function of potential for oxygen reduction on CDC/CNT, M-N-CDC/CNT, and Pt/C catalysts in O_2 -saturated 0.1 M KOH solution. Data derived from Fig. 19.

Table 9. The ORR parameters determined from RRDE results for M-N-CDC/CNT (loading 0.4 mg cm^{-2}) electrocatalyst materials in 0.1 M KOH solution.

Catalyst	$E_{\text{onset}}/\text{V}$	$E_{1/2}/\text{V}$	% HO_2^-	n
CDC/CNT	0.80	<i>n.d.</i>	37–94	2.1–3.2
Fe-N-CDC/CNT	0.99	0.86	2–15	3.8–4.0
Co-N-CDC/CNT	0.93	0.82	20–32	3.4–3.6
CoFe-N-CDC/CNT	0.96	0.83	13–24	3.5–3.7

Short-term stability tests were conducted with all M-N-CDC/CNT catalysts by applying 10,000 potential cycles in O₂-saturated 0.1 M KOH solution. The results are shown in Figure 21. For all the three electrocatalysts, the ORR polarisation curves remain similar after potential cycling, suggesting that the catalysts are highly stable in the alkaline medium. The Co-N-CDC/CNT catalyst had the largest shifts with ΔE_{onset} and $\Delta E_{1/2}$ being 18 and 12 mV, respectively. Fe-N-CDC/CNT and CoFe-N-CDC/CNT, however, showed excellent stability with very small ΔE_{onset} (2 mV and 6 mV) and $\Delta E_{1/2}$ (6 mV and 8 mV) values.

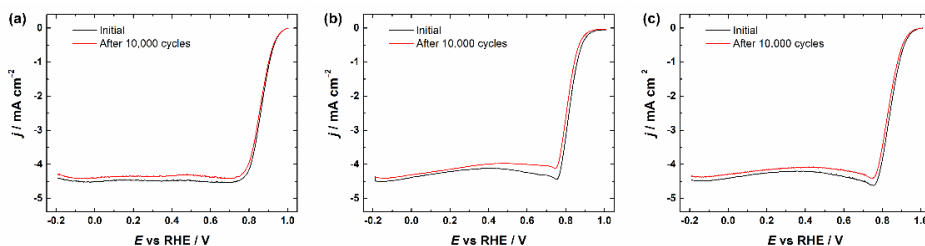


Figure 21. RDE voltammetry curves for ORR on (a) Fe-N-CDC/CNT, (b) Co-N-CDC/CNT, and (c) CoFe-N-CDC/CNT catalyst materials in O₂-saturated 0.1 M KOH solution before and after 10,000 potential cycles ($\omega=960$ rpm, $\nu=10$ mV s⁻¹).

6.3.3 Anion exchange membrane fuel cell test with M-N-CDC/CNT catalysts

As the M-N-CDC/CNT materials showed excellent electrocatalytic activity towards the ORR, then all three were employed as cathode catalysts in the AEMFC together with ETFE anion exchange membrane. The H₂/O₂ AEMFC polarisation curves are shown in Figure 22a. It can be clearly seen that the high catalytic activity of CoFe-N-CDC/CNT transferred to very good AEMFC performances. Under the same conditions, at a cell temperature of 60 °C, the AEMFC with CoFe-N-CDC/CNT cathode reached a peak power density of 1.12 W cm⁻² and a current density of 0.47 A cm⁻² at 0.75 V. Despite the RRDE results showing that the Fe-N-CDC/CNT catalyst had the highest ORR activity, it is known from the literature that RRDE results are not always an accurate predictor of fuel cell results, mainly due to the differences in current densities the RRDE and fuel cells are operated, as well as the mass-transfer-related limitations of fuel cells, which are avoided in the RRDE ideal tests [174]. To our knowledge, these values for the CoFe-N-CDC/CNT cathode AEMFC are among the highest reported in the literature for precious metal-free cathode catalysts (Table 1). For comparison, a MEA based on 40 wt% Pt/C cathode catalyst (loading: 0.70 mg_{Pt} cm⁻²) tested under similar conditions is included. Each of the precious metal-free cathode catalyst shows impressive AEMFC per-

formance with the Co-N-CDC/CNT and CoFe-N-CDC/CNT catalysts even approaching that of the MEA using Pt/C ($P_{\max}=1365 \text{ mW cm}^{-2}$). After acquiring the polarisation curves, the current density was held constant at 0.6 A cm^{-2} for 20 h to evaluate the voltage stability under the same conditions used to acquire the polarisation curve. To the best of our knowledge, the longevity data for the CoFe-N-CDC/CNT in Figure 22b exhibits one of the most stable precious metal-free cathode catalyst data for AEMFCs to date, with a peak-to-peak loss of 0.03 V after 20 h (1.5 mV h^{-1}). Bearing in mind that the current focus of PGM-free ORR catalysts is to replace PGM catalysts, this stability is encouraging and a step in the direction of ultimately achieving significantly lower voltage degradation rates comparable to PGM-catalysed AEMFCs such as $32 \text{ } \mu\text{V h}^{-1}$ and $15 \text{ } \mu\text{V h}^{-1}$, achieved by Peng *et al.* [175] and Hassan *et al.* [176], respectively.

Given the good performance of the CoFe-N-CDC/CNT with H_2/O_2 , following the 20 h of longevity, the cathode oxidant was switched to CO_2 -free air, and additional polarisation curves were captured. As shown in Figure 23a, the CoFe-N-CDC/CNT cell continued to perform well, reaching a P_{\max} value of 0.80 W cm^{-2} . A similar current density holds at 0.6 A cm^{-2} for an additional 20 h was performed under H_2 -air for the CoFe-N-CDC/CNT cell, as shown in Figure 23b. The performance after 20 h was still relatively high, with a peak-to-peak loss of 0.06 V (3 mV h^{-1}).

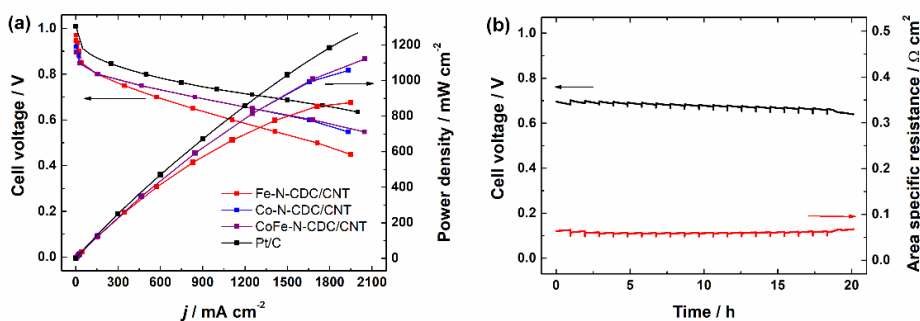


Figure 22. (a) Polarisation and power density curves using various cathode catalysts shown in the legend and (b) CoFe-N-CDC/CNT AEMFC *in-situ* stability operation at a constant current density of 0.6 A cm^{-2} . $T=60 \text{ }^\circ\text{C}$; H_2/O_2 flows 1 L min^{-1} and 100 kPa back-pressurisation on both anode and cathode.

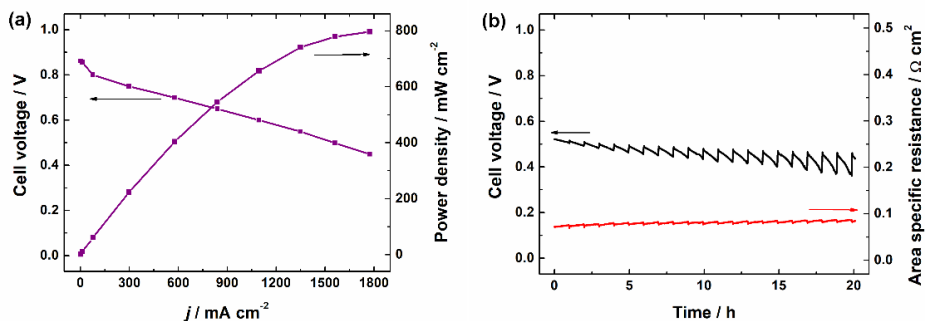


Figure 23. (a) Polarisation and power density curves and (b) *in-situ* stability operation at a constant current density load of 0.6 A cm^{-2} using CoFe-N-CDC/CNT as cathode catalyst. The cathode oxidant is CO_2 -free air; the rest is same as in Figure 22.

6.4 Transition metal and nitrogen doped mesoporous carbons as catalysts

Based on the literature and from the results described in subsections 6.1 to 6.3 it seems that the presence of mesopores seems to be beneficial in the AEMFC application [99, 101, 170]. So herein [V] a commercially available material from Pajarito Powder based on mesoporous carbon (MPC) was chosen as a support. Doping of this MPC was done in the same way as for the materials described in subsection 6.3 by using transition metal acetates and 1,10-phenanthroline as precursors [IV]. In addition to using cobalt and iron, manganese was introduced as it could be beneficial as discussed in subsection 4.3.2. A total of five M-N-C catalysts were prepared, tested and compared, which are Fe-N-MPC, Co-N-MPC, CoFe-N-MPC, FeMn-N-MPC, and CoMn-N-MPC.

6.4.1 Physico-chemical characterisation of M-N-MPC materials

SEM micrographs of starting MPC as well as doped material are shown in Figure 24. The MPC support material (Figure 24a–c) has a rather homogeneous morphology with high roughness and highly porous nature. After doping the material using different metal compositions (Figure 24d–f, [V]), no noticeable differences can be seen from SEM images as the M-N-MPC materials were also mostly homogeneous and had a high roughness at different scales. From the lower magnification images, some larger particles with smoother surface were visible in case of all samples. These results show that doping with metals using high-temperature pyrolysis has not changed the carbon morphology much, suggesting that the feasible structure of starting engineered catalyst support is still present.

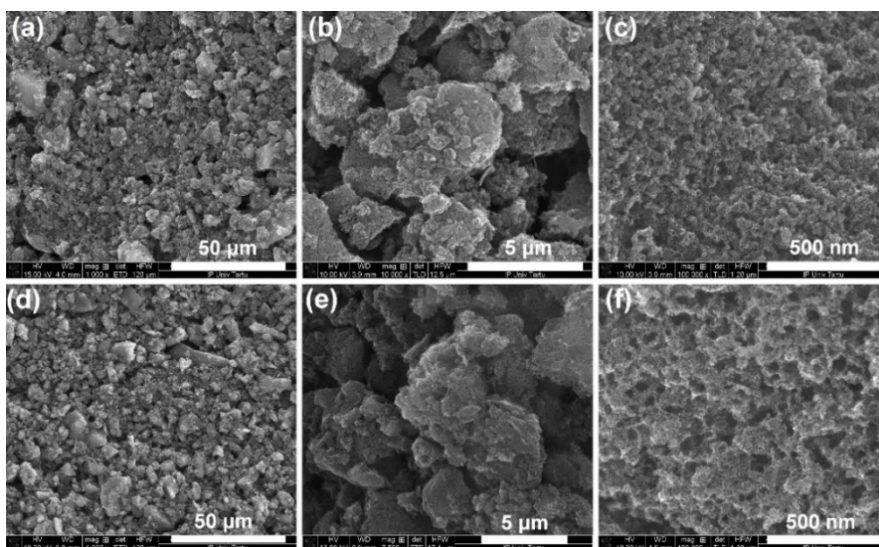


Figure 24. SEM micrographs for MPC (a–c), and FeMn-N-MPC material (d–f).

The morphology of three iron-based materials was further studied using STEM technique with bright field (BF) and high-angle annular dark field (HAADF) images together with EDX mapping (Figure 25, [V]). From the STEM images it is visible that the materials are indeed highly porous and rather homogeneous. Some graphitic carbon structures comprising of approximately 3–4 graphene-like layers can be seen in Figure 25c.

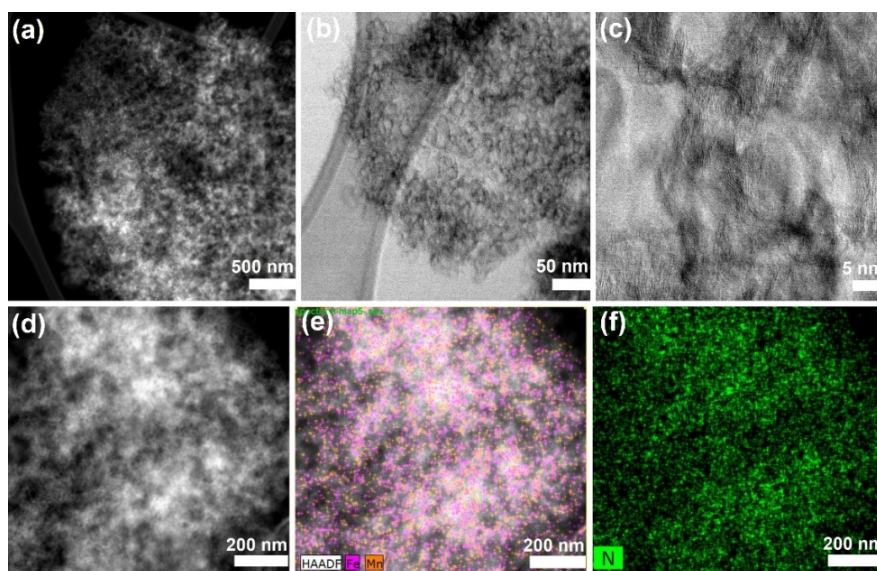


Figure 25. (a, d) HAADF-STEM images, (b–c) BF-STEM images, (e) EDX mapping (HAADF-EDX) for iron and manganese and (f) EDX map of nitrogen of FeMn-N-MPC.

The EDX mapping (Figures 25e,f) shows that the nitrogen and corresponding metals are uniformly distributed in the catalyst materials and no large particles are visible, which suggests that metals can be atomically dispersed in the M-N-MPC materials. This is also supported by the higher magnification HAADF-STEM images of FeMn-N-MPC (Figure 26) where well-distributed brighter spots correspond to transition metal atoms.

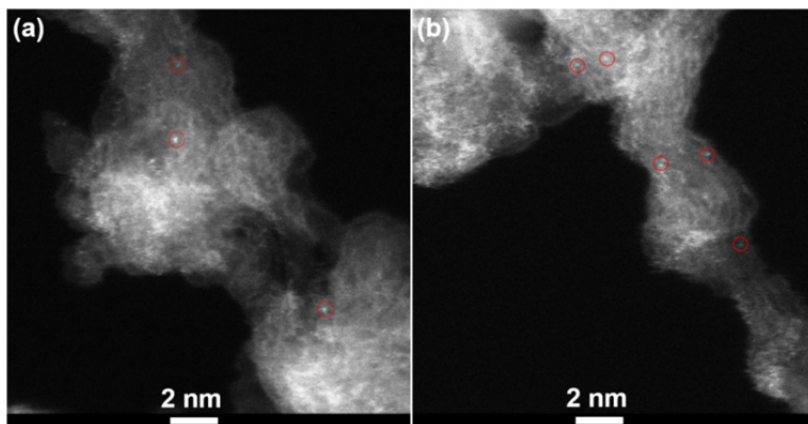


Figure 26. (a, b) HAADF-STEM images of FeMn-N-MPC with some of the discerned metal atoms showcased inside the rings.

The results of N_2 physisorption studies conducted are summarised in Table 10 and Figure 27a. The SSA of starting MPC material was $814 \text{ m}^2 \text{ g}^{-1}$ and decreased to around 500 to $600 \text{ m}^2 \text{ g}^{-1}$ in M-N-MPC catalyst materials, meaning that during the doping process some of the existing pores were blocked. Similarly, the total pore volume decreased from $1.51 \text{ cm}^3 \text{ g}^{-1}$ in MPC to 1.22 – $1.35 \text{ cm}^3 \text{ g}^{-1}$ in M-N-MPC samples. There are two distinct maxima in all pore-size distribution graphs (Figure 27a) corresponding to the smaller and larger mesopores in the diameter range of 7 – 8 nm and 25 – 35 nm , respectively. This means the prepared catalysts herein have a bimodal mesoporous structure that can be useful in AEMFC performance [170].

Table 10. Specific surface area (SSA) and total pore volume (V_{tot}) for MPC and M-N-MPC samples.

	MPC	Fe-N-MPC	Co-N-MPC	CoFe-N-MPC	FeMn-N-MPC	CoMn-N-MPC
SSA ($\text{m}^2 \text{ g}^{-1}$)	814	584	535	571	583	613
V_{tot} ($\text{cm}^3 \text{ g}^{-1}$)	1.51	1.33	1.24	1.22	1.24	1.35

The first-order Raman spectra of the MPC and M-N-MPC catalyst materials are presented in Figure 27b. The Raman spectra of all the materials are very similar and characteristic to that of carbon materials. The ratio of the integrated areas of D1 and G peaks, I_{D1}/I_G , was 1.34 for MPC and increased to 1.43 in all other samples. The widths of D1 and G bands, which increase with the degree of disorder in the graphitic lattice [172], were more or less the same in all samples being 130 and 81 cm^{-1} , respectively. High I_{D1}/I_G values as well as wide D1 and G bands indicate that there is a significant level of disorder together with defects present in the prepared catalyst materials.

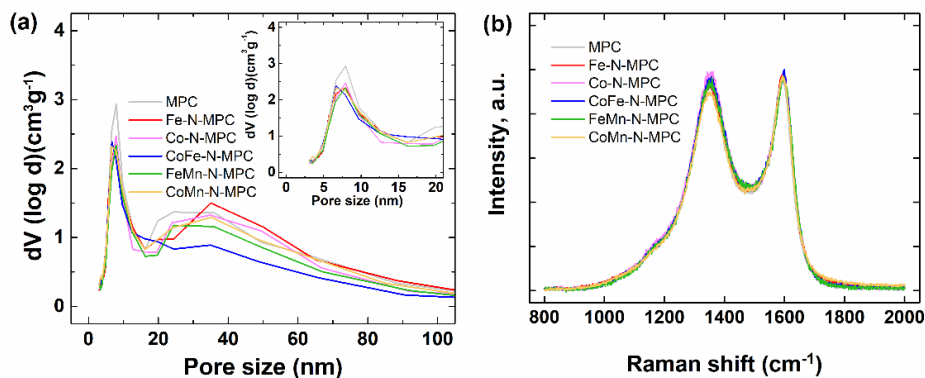


Figure 27. (a) Pore size distributions and (b) Raman spectra for MPC and M-N-MPC materials.

According to the XPS spectra (Figure 28), in case of all five samples C, N, O as well as the added respective metals (Fe, Co, Mn or two of them) are present on the surface of the catalyst materials. The overall surface nitrogen content was almost the same in all M-N-MPC materials and ranged from 2.2 to 2.4 at%. For determination of the type of N species present in the prepared catalysts, the N1s region of the detailed XPS spectra was deconvoluted into seven peaks with the results shown in Figure 28b and Table 11. Pyridinic-N, pyrrolic-N and graphitic-N were present in the highest amounts, but there was also a noticeable concentration of metal-coordinated nitrogen species ($M-N_x$). This coexistence of different moieties, which is common in materials synthesised using high-temperature pyrolysis, could be beneficial, as each of them is responsible for certain steps in the ORR, as discussed in subsection 4.3.

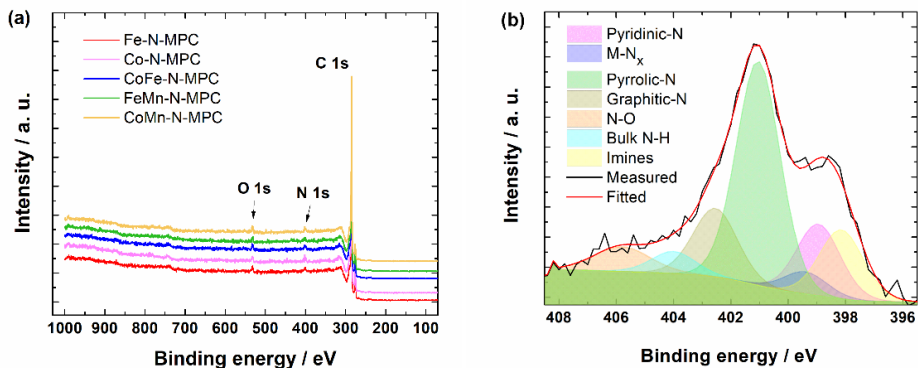


Figure 28. (a) XPS survey spectra for M-N-MPC materials. (b) N1s high resolution XPS spectra for FeMn-N-MPC.

Table 11. Relative concentration (%) of N species on M-N-MPC materials by XPS analysis.

N species	Fe-N-MPC	Co-N-MPC	CoFe-N-MPC	FeMn-N-MPC	CoMn-N-MPC
Pyridinic-N	16.5	17.5	15.6	16.9	17.0
M-N _x	7.8	11.5	12.2	9.1	9.2
Pyrrolic-N	22.2	23.8	22.8	22.1	24.9
Graphitic-N	30.0	29.4	29.1	29.9	28.6
N-O	10.4	5.5	7.6	8.2	8.8
Bulk N-H	10.0	10.2	10.6	10.4	9.2
Imine	3.1	2.1	2.1	3.4	2.3

As per MP-AES results in Table 12, the bulk transition metal content is close to 1 wt% in all M-N-MPC materials, and in bimetallic materials, both added transition metals constitute to around the half of the overall metal content, which together with similar N-contents in the XPS suggest that doping has been successful with all transition metal compositions.

Table 12. Bulk transition metal composition (wt%) of M-N-MPC materials determined by MP-AES.

	Fe-N-MPC	Co-N-MPC	CoFe-N-MPC	FeMn-N-MPC	CoMn-N-MPC
Fe	0.821±0.004	-	0.656±0.010	0.663±0.009	-
Co	-	1.098±0.011	0.497±0.003	-	0.519±0.002
Mn	-	-	-	0.583±0.003	0.538±0.004

6.4.2 Oxygen reduction reaction on M-N-MPC catalysts

The initial assessment of the prepared catalyst materials' activity towards the ORR was done using the RRDE method in O₂-saturated 0.1 M KOH aqueous solution at 960 rpm. The obtained disc current densities and ring currents are shown in Figure 29 with the results compiled as well in Table 13. The starting MPC material had the lowest ORR performance with the onset potential for O₂ reduction being 0.90 V, the half-wave potential being 0.80 V, and the lowest diffusion-limited current value. All five prepared catalyst materials showed better performance than the pristine MPC. Among them, the Co-N-MPC and CoMn-N-MPC catalysts had somewhat inferior performance while exhibiting $E_{1/2}$ of 0.84 V. On the other hand, the materials containing iron, namely Fe-N-MPC, CoFe-N-MPC, and FeMn-N-MPC all showed impressive ORR activity similar to that of the commercial Pt/C (20 wt%) with E_{onset} and $E_{1/2}$ of around 1.0 and 0.9 V, respectively.

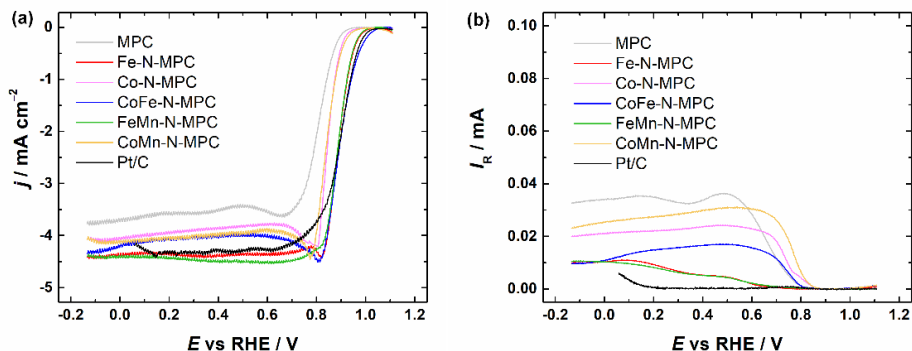


Figure 29. RRDE results for the ORR in O₂-saturated 0.1 M KOH solution on MPC, M-N-MPC, and Pt/C catalysts. (a) disc current densities, (b) ring currents. $\omega=960$ rpm, $\nu=10$ mV s⁻¹.

To obtain more information on the ORR pathway, the respective ring currents were also collected (Figure 29b), and by using the data given in Figure 29, the yield of HO₂⁻ formation and the number of electrons transferred were calculated with results presented in Table 13. Some of the same tendencies that were visible from the ORR polarisation curves are applicable herein: the MPC had the poorest performance by having the HO₂⁻ formation of around 40% in a wide range of potentials, followed by Co-N-MPC and CoMn-N-MPC with 21 to 36%. While the remaining three catalysts showed almost identical values of E_{onset} and $E_{1/2}$, the CoFe-N-MPC material had higher yield of hydroperoxide anions (11 to 21%) than Fe-N-MPC and FeMn-N-MPC, which both had low %HO₂⁻ of 1 to 12%. The latter two were also closest to the Pt/C in that sense and the n value was close to four for these catalysts, being less than four for other materials.

Table 13. The ORR parameters determined from RRDE results for MPC and M-N-MPC (loading 0.4 mg cm⁻²) electrocatalyst materials in 0.1 M KOH solution.

Catalyst	$E_{\text{onset}}/\text{V}$	$E_{1/2}/\text{V}$	%HO ₂ ⁻	n
MPC	0.90	0.80	24–46	3.0–3.5
Fe-N-MPC	0.99	0.89	1–12	3.8–4.0
Co-N-MPC	0.92	0.84	21–30	3.4–3.6
CoFe-N-MPC	1.00	0.90	11–21	3.5–3.7
FeMn-N-MPC	0.98	0.89	1–12	3.8–4.0
CoMn-N-MPC	0.94	0.84	28–36	3.3–3.5
Pt/C (20 wt%)	1.00	0.90	0–8	3.9–4.0

The short-term stability test was done with three best-performing catalyst materials and involved potential cycling for 10,000 times with the ORR polarisation curves as well as respective ring currents in RRDE were recorded before and after (Figure 30). In case of all three materials, namely Fe-N-MPC, CoFe-N-MPC, and FeMn-N-MPC, the electrocatalytic activity remained virtually the same as no significant differences can be seen between the initial ORR polarisation curve and the one obtained after 10,000 potential cycles. Both the Fe-N-MPC and FeMn-N-MPC catalysts had a negative shift of 6 mV in terms of half-wave potential, while CoFe-N-MPC had $\Delta E_{1/2}$ of 8 mV. Additionally, the yield of HO₂⁻ can also be compared before and after short-term stability test (Figure 30d–f). A slight increase in the HO₂⁻ yield was observed with Fe-N-MPC and CoFe-N-MPC catalysts while for the FeMn-N-MPC material it remained practically the same.

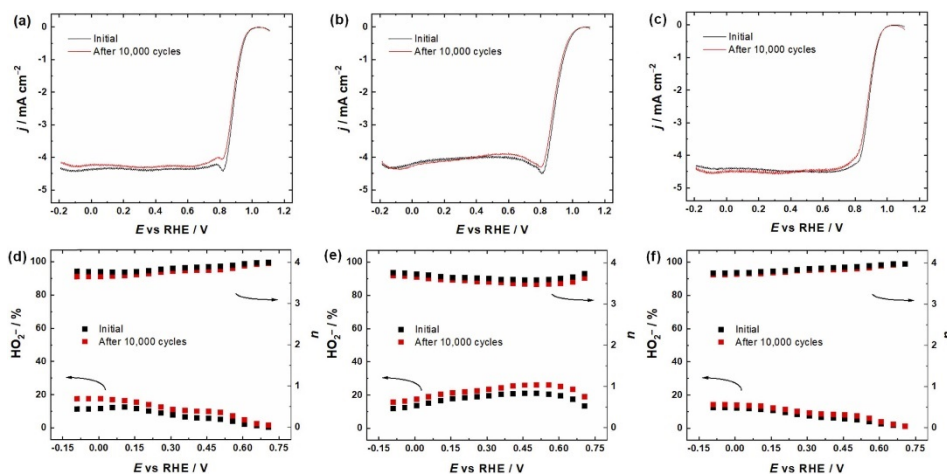


Figure 30. (a–c) ORR polarisation curves and (d–f) the percentage yield of HO₂⁻ formation and the value of n as a function of potential for (a, d) Fe-N-MPC, (b, e) CoFe-N-MPC and (c, f) FeMn-N-MPC catalyst materials in O₂-saturated 0.1 M KOH solution before and after 10,000 potential cycles ($\omega=960$ rpm, $\nu=10$ mV s⁻¹).

6.4.3 Anion exchange membrane fuel cell test with M-N-MPC catalysts

An aspect to consider in the AEMFC application viewpoint is the formation of HO_2^- during the ORR, since it can poison the metal-containing active sites as well as lowers the fuel cell's efficiency and power [88]. The results obtained herein indeed proved that cobalt-based catalyst materials facilitate peroxide production, whilst iron-based ones show significantly lower HO_2^- yields (also in combination with manganese) [86]. Due to this reason, the Fe-N-MPC and FeMn-N-MPC materials were chosen to be employed as cathode catalysts in AEMFC together with HMT-PMBI AEM. The AEMFC testing results are shown in Figure 31. For comparison, commercial Pt/C (46 wt%) catalyst was also used on the cathode side. Similarly to the RRDE results, both Fe-N-MPC and FeMn-N-MPC showed almost identical behaviour and impressive performance as the obtained peak power densities were 473 and 474 mW cm^{-2} , and current densities at 0.75 V were 391 and 372 mA cm^{-2} , respectively. Both of these performances were superior to the MEA applying Pt/C cathode catalyst and tested under same conditions.

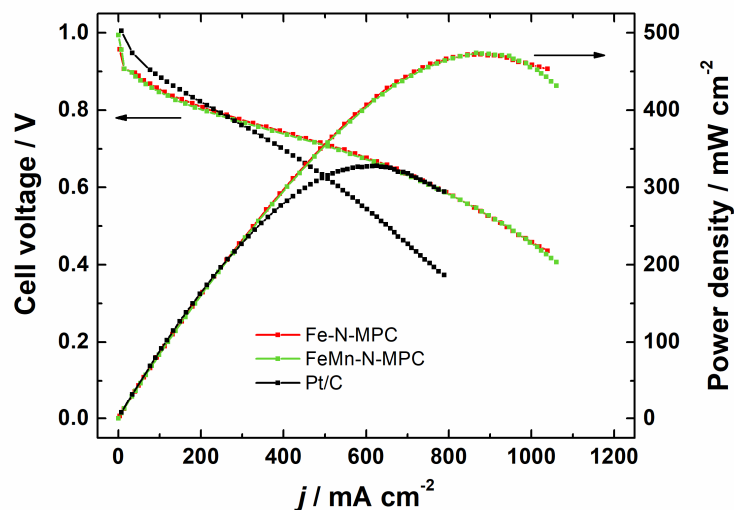


Figure 31. Polarisation and power density curves for H_2/O_2 AEMFCs. Cathode catalyst: Fe-N-MPC, FeMn-N-MPC or Pt/C; anode catalyst: PtRu/C and AEM: HMT-PMBI. $T=60^\circ\text{C}$.

In comparison to the performances of AEMFC employing the HMT-PMBI membrane (Table 1), the results obtained in this study are very good. Such AEMFC performance with Fe-N-MPC and FeMn-N-MPC cathode catalysts could be due to the combination of mesoporous structure and presence of ORR-active sites, including the Fe-N_4 moieties. The mesoporous nature (pore dia-

meters of 7–8 nm and 25–35 nm) of these catalysts is beneficial for the transport of reactants, making the embedded active sites accessible during the AEMFC operation. Such larger pores, especially those in range of 25–35 nm, are less likely to be blocked by ionomer or liquid water, thus mesopores are responsible for the mass-transport of reactants and products through the catalyst layer [101, 177, 178]. As active sites, the Fe-N-MPC and FeMn-N-MPC materials both contain a mixture of different nitrogen moieties according to XPS, whose co-existence seems to be useful indeed. These iron-containing materials also have Fe-N_x active sites as XPS showed the presence of M-N_x moieties in both materials and no large metal agglomerates being visible from STEM studies, thus suggesting that transition metals might be atomically dispersed.

6.5 Cobalt-, iron- and nitrogen-doped ordered mesoporous carbon-based catalysts

As mesoporous carbon-based catalysts described in subsection 6.4 showed very good performance both in half-cell tests as well as in the AEMFC, then the work was continued on such carbons. Herein, ordered mesoporous carbon (OMC) was synthesised via rather environmentally friendly and simple soft-templating approach (details in subsection 5.1) [VI]. To assess the effect of porous structure, composites of OMC/CDC and OMC/CNT were also employed as support materials. Doping was done similarly to the materials described in subsections 6.3 and 6.4 with 1,10-phenanthroline, iron- and cobalt acetate as precursors, resulting in three bimetallic catalysts: CoFe-N-OMC, CoFe-N-OMC/CDC and CoFe-N-OMC/CNT.

6.5.1 Physico-chemical characterisation of OMC-based materials

The results of N₂ physisorption studies together with textural properties of the OMC and M-N-C catalysts are given in Figure 32 and Table 14. According to this, the synthesised OMC material has pores predominantly with diameter of *ca* 7 nm and a rather high SSA of 714 m² g⁻¹, thus meaning that the preparation of mesoporous carbon has been a success.

The shape of the N₂ physisorption isotherm on OMC-based materials corresponds to a combination of type I and III with H2 hysteresis according to IUPAC [171], which is characteristic of micro-mesoporous materials with a small proportion of micropores. H2 hysteresis also refers to the presence of complexly structured pores in ordered mesoporous materials. The N₂ adsorption-desorption isotherm of CoFe-N-OMC/CNT sample also exhibits H3 hysteresis, indicating the presence of larger pores in the material. From the results (Figure 32, Table 14) it is evident that the doping has changed the textural properties of OMC material, as the SSA of CoFe-N-OMC is lower at 486 m² g⁻¹ and that almost all the micropores present in OMC have been replaced with smaller mesopores (width *ca.* 2–3 nm), suggesting pore widening

during the process. Whilst comparing the three carbon supports used, namely OMC, OMC/CDC and OMC/CNT, then the CoFe-N-OMC/CNT has the lowest SSA. From the three catalyst materials, the CoFe-N-OMC sample has the highest total pore volume, which is almost identical to that of non-doped OMC's. While the doped OMC material is almost entirely mesoporous, the addition of CDC causes a significant increase of micropores and SSA_{micro} is taking up slightly more than SSA_{meso} . The OMC/CNT composite possesses ca 30% of SSA corresponding to micropores and 70% to mesopores. From the pore size distributions (Figure 32b) it is clear that all catalyst materials exhibit average pores with width of 7 nm, originating from the OMC. In case of CoFe-N-OMC/CDC there are more pores in less than 2 nm range and in CoFe-N-OMC/CNT there are also larger mesopores present with width in the range of 15–40 nm. This confirms that indeed three CoFe-N-C materials with varying porous structure have been prepared: CoFe-N-OMC with narrow distribution of mesopores, CoFe-N-OMC/CDC combining meso- and micropores, and CoFe-N-OMC/CNT combining smaller (*ca.* 7 nm) and larger (*ca.* 15–40 nm) mesopores.

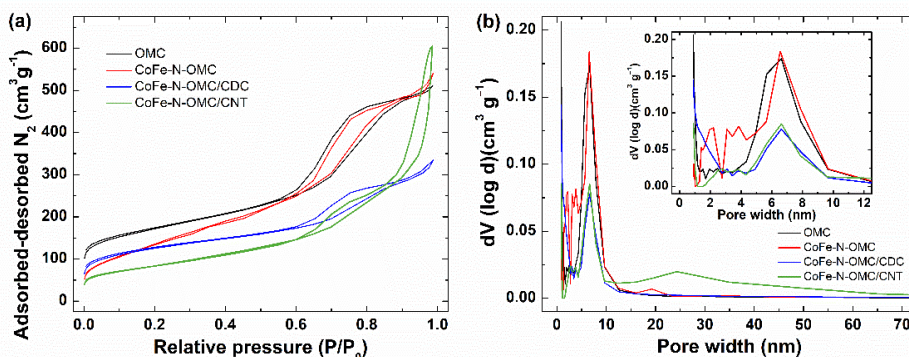


Figure 32. (a) N_2 adsorption-desorption isotherms and (b) pore size distributions for OMC and CoFe-N-C materials.

Table 14. Textural properties of OMC and CoFe-N-C materials: specific surface area (SSA), micro- and mesoporous SSA (SSA_{micro} , SSA_{meso}), total pore volume (V_{tot}) and micro-pore volume (V_{micro}).

Catalyst	SSA ($\text{m}^2 \text{g}^{-1}$)	SSA_{micro} ($\text{m}^2 \text{g}^{-1}$)	SSA_{meso} ($\text{m}^2 \text{g}^{-1}$)	V_{tot} ($\text{cm}^3 \text{g}^{-1}$)	V_{micro} ($\text{cm}^3 \text{g}^{-1}$)
OMC	714	413	301	0.77	0.12
CoFe-N-OMC	414	32	382	0.78	0.02
CoFe-N-OMC/CDC	438	250	188	0.48	0.10
CoFe-N-OMC/CNT	312	88	224	0.64	0.02

The OMC material (Figure 33a–c) has quite homogeneous morphology with high roughness and uniform pore size. The size of OMC particles is around 1 μm , however, both smaller and larger particles are visible. After doping (Figure 33d) no noticeable differences in the morphology can be seen as CoFe-N-OMC exhibits the same properties as OMC. In the CoFe-N-OMC/CDC material (Figure 33e), both CDC and OMC particles are in the same size range and well mixed together. The CNTs and OMC are also well dispersed in the CoFe-N-OMC/CNT material with the CNTs forming a continuous network surrounding and covering the OMC particles (Figure 33f). While the OMC material seems to keep its textural properties during doping, then the three prepared M-N-C materials exhibit very different morphologies according to SEM images, which is interesting to study in the AEMFC application.

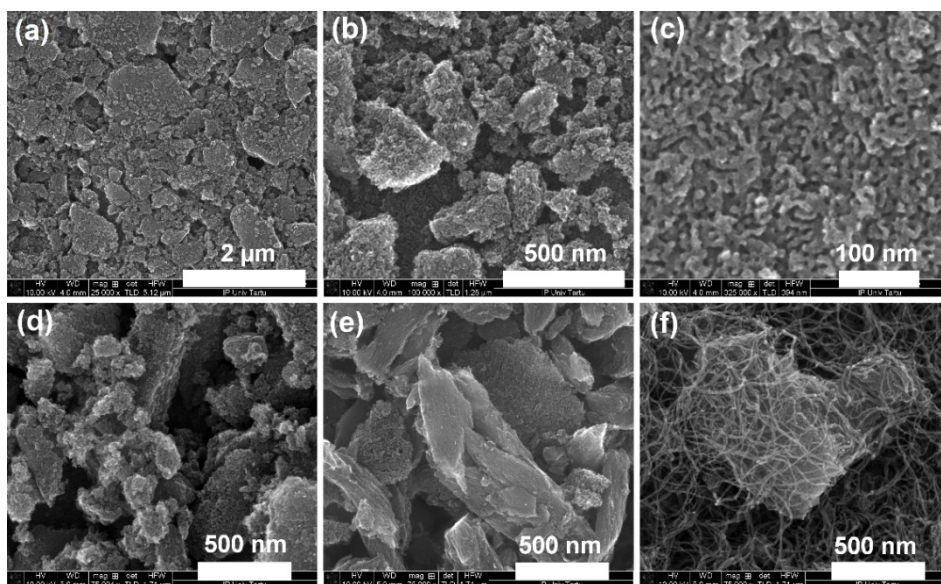


Figure 33. (a–c) SEM micrographs of OMC material at various magnifications. (d–f) SEM micrographs at same magnification for (d) CoFe-N-OMC, (e) CoFe-N-OMC/CDC and (f) CoFe-N-OMC/CNT catalysts.

Low-magnification bright-field (BF) STEM image of the CoFe-N-OMC catalyst (Figure 34a) shows that this material has a well-ordered porous structure. The size of the visible pores is rather uniform and agrees well with the results of N_2 physisorption analysis. At higher magnification, the formation of graphitic carbon layers is also visible that indicates some degree of graphitization, which is beneficial for electrical conductivity and corrosion resistance of the catalyst material. High-angle annular dark field imaging was used to see the distribution of the doping metals inside the OMC catalyst. The bright spots visible in the Figure 34c correspond to individual metal atoms, indicating ultrafine dispersion

of the Co and Fe in the catalyst material. The STEM-EDX mapping (Figure 34d–g) also reveals a noticeable increase in Co and Fe signal in the OMC region, indicating the presence of these metals in the catalyst. According to the EDX maps, both metals and nitrogen are uniformly distributed in the CoFe-N-OMC material.

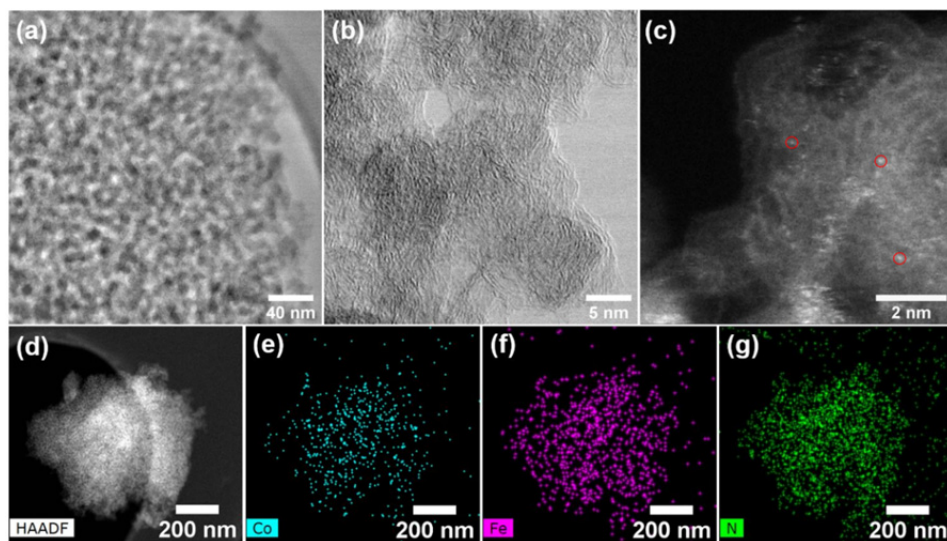


Figure 34. (a, b) BF-STEM images of the as-prepared CoFe-N-OMC catalyst material; (c) HAADF-STEM images of CoFe-N-OMC with red rings encircling some of the single metal atoms inside the catalyst. (d) Lower magnification HAADF-STEM image and the corresponding EDX maps of (e) cobalt, (f) iron, and (g) nitrogen.

The Raman spectra of OMC-based materials shown in Figure 35a exhibit broadened graphitic carbon (G, $\sim 1590\text{ cm}^{-1}$) and disordered carbon (D1, $\sim 1350\text{ cm}^{-1}$) peaks, which are characteristic to carbon materials. To assess the degree of structural disordering in the prepared OMC and catalyst materials, the full width at half-maximum of the D1 and G-bands as well as I_{D1}/I_G ratio were determined [VI] and according to that the structural disorder increases slightly in the sequence of CoFe-N-OMC/CNT, CoFe-N-OMC/CDC, OMC, CoFe-N-OMC. This indicates that the prepared OMC has quite defect rich nature and doping did not change that much, however, by making a composite with CNTs, a catalyst with less disorder is obtained, likely due to the CNTs covering the OMC particles as was evident from SEM images (Figure 33f).

According to MP-AES, all three M-N-C materials contain around 0.5 wt% of iron and *ca.* 0.5 wt% of cobalt. The nitrogen content was *ca.* 4 wt% in doped materials as per SEM-EDX analysis. This suggests that doping has worked similarly and successfully with different carbon substrates employed.

The XPS survey spectra for the OMC and M-N-C materials are shown in Figure 35b. The spectrum of OMC sample has peaks corresponding to oxygen and carbon present, while in M-N-C materials the N1s peak appears at around 400 eV. From the deconvolution of this N1s peak (example in Figure 35c) it is evident that in all three catalyst materials pyridinic-N and pyrrolic-N are most prominent nitrogen types (relative content 24 to 35%), followed by M-N_x (13 to 20%) and, around 10% of graphitic nitrogen. These results indicate that doping indeed has been rather similar with all carbon substrates and that all these M-N-C catalysts contain a mix of different active sites.

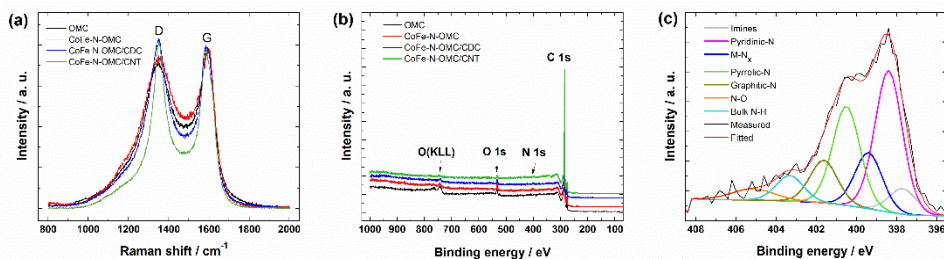


Figure 35. (a) Raman and (b) XPS survey spectra of OMC, CoFe-N-OMC, CoFe-N-OMC/CDC and CoFe-N-OMC/CNT materials. (c) N1s high-resolution XPS spectra for CoFe-N-OMC sample.

6.5.2 Oxygen reduction reaction on OMC-based catalysts

The ORR activity of OMC-based materials was assessed using the RDE method with the polarisation curves at 1900 rpm in 0.1 M KOH solution shown in Figure 36. As expected, the OMC material showed the lowest ORR electrocatalytic activity with the onset potential of O₂ reduction being 0.82 V, while the polarisation curve exhibits two reduction waves. A significant improvement of electrocatalytic activity was observed with Co, Fe and N-doped materials and all three have polarisation curves with a single reduction wave, suggesting a four-electron reduction of oxygen. The overall ORR activity of CoFe-N-OMC, CoFe-N-OMC/CDC and CoFe-N-OMC/CNT materials was almost identical as all of them had onset potential of 1.0 V and half-wave potential of 0.84 V. For comparison, slightly higher values ($E_{\text{onset}}=1.01$ V and $E_{1/2}=0.87$ V) were observed for commercial Pt/C catalyst.

Additionally, for all CoFeN-C materials, the intercept of K-L lines is close to zero at $E < 0.7$ V and the number of electrons transferred was close to 4 [VI], which means that the ORR proceeds either via 4e⁻ or 2-step 2e⁻ pathway.

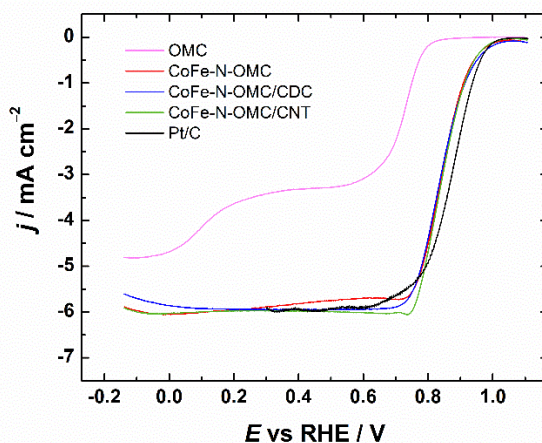


Figure 36. RDE voltammety curves for ORR on OMC-based catalysts in O_2 -saturated 0.1 M KOH solution ($\omega=1900$ rpm, $\nu=10$ $mV s^{-1}$).

As all three CoFe-N-C materials showed high and identical ORR activity, then all these were subjected to the short-time stability tests with the results presented in Figure 37. For all the three electrocatalysts, the shape of the ORR polarisation curve remains the same, suggesting that the catalysts are highly stable in the alkaline medium. After 10,000 potential cycles, the half-wave potential shifted by 16, 18 and 14 mV in case of CoFe-N-OMC, CoFe-N-OMC/CDC and CoFe-N-OMC/CNT, respectively.

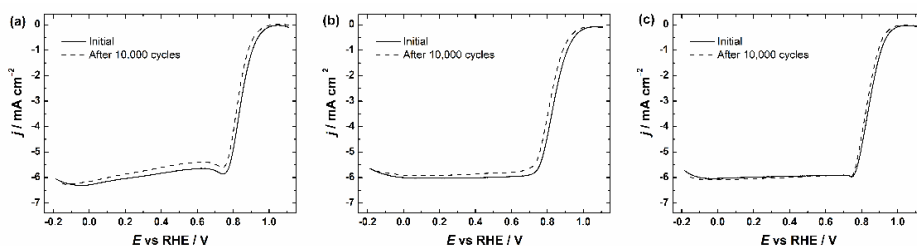


Figure 37. RDE voltammety curves for ORR on (a) CoFe-N-OMC, (b) CoFe-N-OMC/CDC and (c) CoFe-N-OMC/CNT catalyst in O_2 -saturated 0.1 M KOH solution before and after 10,000 potential cycles ($\omega=1900$ rpm, $\nu=10$ $mV s^{-1}$).

6.5.3 Anion exchange membrane fuel cell test with OMC-based catalysts

The AEMFC testing was performed using CoFe-N-OMC, CoFe-N-OMC/CDC, or CoFe-N-OMC/CNT as cathode catalyst with AEMION+ (10 μm) anion exchange membrane and PtRu/C as anode catalyst (Figure 38). In the higher current density regions of ohmic loss and mass transport loss (>400 $mA cm^{-2}$),

the influence of different carbon composite supports in the CoFe-N-C catalysts seems to play a significant role on the AEMFC performance. The CoFe-N-OMC and CoFe-N-OMC/CDC cathodes show a rather similar behaviour with P_{\max} of 254 and 268 mW cm^{-2} , respectively. However, the incorporation of CNTs with OMC in the carbon support seems to be considerably more advantageous as higher P_{\max} value of 336 mW cm^{-2} at 900 mA cm^{-2} was reached, which indicates that the porous structure of materials is important in the AEMFC application and that the presence of larger mesopores (15 to 40 nm herein) is beneficial.

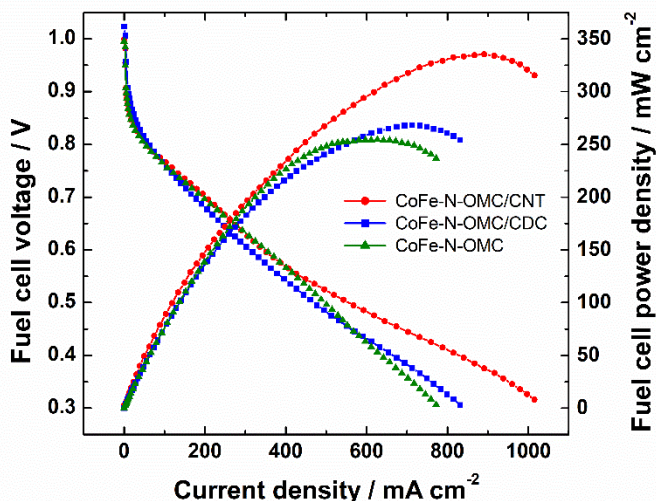


Figure 38. Power density and polarisation curves for H_2/O_2 single-cell AEMFC with the AEMION+ (10 μm) anion exchange membrane, CoFe-N-C as a cathode catalyst (loading 1 mg cm^{-2}) and PtRu/C as the anode catalyst (loading 0.4 $\text{mg}_{\text{PtRu}} \text{cm}^{-2}$). $T=65^\circ\text{C}$.

The AEMFC results described in this subsection are inferior to those shown in previous subsections, however, it should be noted that herein [VI] the catalyst loadings on anode and cathode were significantly reduced to have lower PGM loading and thinner cathode layer to be compatible with the specific AEM. Additionally, the differences in the AEMs and operating conditions, which are optimised to specific catalysts, make the comparison of AEMFC performances with the literature (*e.g.* Table 1) as well as within this doctoral thesis rather difficult. Considering these aspects, the self-made OMC material could still be a suitable support for M-N-C cathode catalysts for the AEMFCs.

7. SUMMARY

The aim of this doctoral thesis was to prepare nanocarbon-based non-precious metal catalysts for electrochemical oxygen reduction reaction (ORR) and test their applicability in the anion exchange membrane fuel cell (AEMFC). The transition metal and nitrogen doped catalysts were prepared by high-temperature pyrolysis, using various nitrogen precursors and transition metal sources as well as different nanocarbon supports. The preliminary evaluation of the prepared electrocatalysts was carried out in alkaline medium by rotating disc electrode (RDE) and rotating ring-disc electrode (RRDE) methods, to study the effect of the support materials and precursors on the electrocatalytic performance of the resulting catalysts. The better-performing catalysts were employed on the cathode in the single-cell AEMFC. The catalyst materials were thoroughly characterised via several physico-chemical methods.

In the first part of the thesis, a composite of carbide-derived carbon (CDC) and carbon nanotubes (CNTs) was doped with either just nitrogen [I] or nitrogen and cobalt [II]. Dicyandiamide, cyanamide, urea and melamine were used as nitrogen sources. The prepared CDC/CNT-based materials have high specific surface area with the presence of both micro- and mesopores. All nitrogen precursors were proven to be suitable for doping via pyrolysis, as the nitrogen moieties present in the catalysts were rather similar according to the X-ray photoelectron spectroscopy (XPS) results. This also resulted in comparable ORR performance. While metal-free N-doped CDC/CNT catalysts showed quite high ORR activity, then a noticeable improvement was obtained when cobalt was also incorporated into the catalyst materials, suggesting that transition metal coordinated to nitrogen ($M-N_x$) species are needed as active sites for the ORR to reach the electrocatalytic activity of Pt/C. The need for transition metal incorporation was also evident from the AEMFC results, as almost twice higher peak power density (P_{max}) was obtained with Co-N-CDC/CNT material than with N-CDC/CNT used as a cathode catalyst.

In the second part, a composite of graphene-like material (Gra) and CNTs was utilised as a carbon support. Melamine was chosen as N source and three transition metal additives, namely iron, cobalt, or both of them, were used and compared. The Gra/CNT composite offered similar textural properties as CDC/CNT, which was not influenced much by varying metal additives. In the RRDE experiment all three catalysts showed rather similar ORR activity, which was comparable to that of Pt/C. However, the HO_2^- yield depended on the metal additive, with Co-N-Gra/CNT producing the most, Fe-N-Gra/CNT the least and bimetallic CoFe-N-Gra/CNT intermediate amounts of peroxide. In the AEMFC conditions they also performed differently, with CoFe-N-Gra/CNT showing the superior performance, virtually the same with Pt/C tested under the same conditions, which suggests that synergistic effects in bimetallic materials are beneficial.

In the third part, the CDC/CNT composite was used again, but this time 1,10-phenanthroline was the N source, which was combined with transition

metal (Co, Fe or both) acetates, with the overall metal content being lowered to *ca.* 1 wt%. The physical properties of catalysts were rather similar to those obtained in part one, and the same tendencies for ORR performance were seen with different metal additives as in part two of the work. This time ETFE-based anion exchange membrane was used in the AEMFC tests. CoFe-N-CDC/CNT was superior to iron- and cobalt-based catalysts in AEMFC test, by reaching P_{\max} of 1.12 W cm^{-2} and 0.80 W cm^{-2} in H_2/O_2 and H_2/air fed systems, respectively.

In part four, commercially available mesoporous carbon-based (MPC) support material was doped again with nitrogen (1,10-phenanthroline) and transition metals (Fe, Co, Mn). Five catalysts with the following metal compositions were prepared: Fe, Co, CoFe, CoMn, FeMn. These MPC-based catalysts had predominantly bimodal mesoporous structure with pores at *ca.* 7 and 25–35 nm. In the RRDE measurements, iron-based materials (Fe-N-MPC, CoFe-N-MPC and FeMn-N-MPC) possessed similar electrocatalytic properties and high ORR activity. The HO_2^- yield was higher on Co-containing materials, and lower (less than 10%) on Fe- and FeMn-based catalysts. Due to this reason, the Fe-N-MPC and FeMn-N-MPC were chosen to be tested in the AEMFC, where they showed virtually the same fuel cell performance by obtaining P_{\max} of $\sim 470 \text{ mW cm}^{-2}$.

In part five, ordered mesoporous carbon (OMC) was synthesised and employed as a catalyst support. This OMC material had mesopores mostly with 7 nm in diameter. To study the effect of porous structure of the catalysts on their ORR and AEMFC performance, the OMC was combined with CDC and CNTs and doped with nitrogen (1,10-phenanthroline), cobalt and iron. Three bimetallic catalysts with varying porous structure were obtained: mesoporous CoFe-N-OMC, micro- and mesoporous CoFe-N-OMC/CDC, and CoFe-N-OMC/CNT with smaller (7 nm) and larger (15–40 nm) mesopores. These catalysts showed virtually the same and high ORR activity in the RDE test. The effect of porous structure became evident in the AEMFC, where the CoFe-N-OMC/CNT performed the best, indicating that larger mesopores are beneficial.

The findings of this doctoral thesis offer more insight to the effect of different transition metal additives and the porous structure of the catalysts on their ORR activity and AEMFC performance, thereby adding a valuable contribution to the field of ORR electrocatalysis on non-precious metal catalysts.

8. REFERENCES

- [1] J.O. Abe, A.P.I. Popoola, E. Ajenifuja, O.M. Popoola, Hydrogen energy, economy and storage: Review and recommendation, *International Journal of Hydrogen Energy* 44 (2019) 15072–15086.
- [2] H. Nazir, C. Louis, S. Jose, J. Prakash, N. Muthuswamy, M.E.M. Buan, C. Flox, S. Chavan, X. Shi, P. Kauranen, T. Kallio, G. Maia, K. Tammeveski, N. Lymperopoulos, E. Carcadea, E. Veziroglu, A. Iranzo, A.M. Kannan, Is the H₂ economy realizable in the foreseeable future? Part I: H₂ production methods, *International Journal of Hydrogen Energy* 45 (2020) 13777–13788.
- [3] I. Staffell, D. Scamman, A.V. Abad, P. Balcombe, P.E. Dodds, P. Ekins, N. Shah, K.R. Ward, The role of hydrogen and fuel cells in the global energy system, *Energy & Environmental Science* 12 (2019) 463–491.
- [4] B.G. Pollet, S.S. Kocha, I. Staffell, Current Status of Automotive Fuel Cells for Sustainable Transport, *Current Opinion in Electrochemistry* 16 (2019) 90–95.
- [5] H. Nazir, N. Muthuswamy, C. Louis, S. Jose, J. Prakash, M.E.M. Buan, C. Flox, S. Chavan, X. Shi, P. Kauranen, T. Kallio, G. Maia, K. Tammeveski, N. Lymperopoulos, E. Carcadea, E. Veziroglu, A. Iranzo, A.M. Kannan, Is the H₂ economy realizable in the foreseeable future? Part III: H₂ usage technologies, applications, and challenges and opportunities, *International Journal of Hydrogen Energy* 45 (2020) 28217–28239.
- [6] M.K. Debe, Electrocatalyst approaches and challenges for automotive fuel cells, *Nature* 486 (2012) 43–51.
- [7] B. Tanc, H.T. Arat, E. Baltacioglu, K. Aydin, Overview of the next quarter century vision of hydrogen fuel cell electric vehicles, *International Journal of Hydrogen Energy* 44 (2019) 10120–10128.
- [8] S. Gottesfeld, D.R. Dekel, M. Page, C. Bae, Y.S. Yan, P. Zelenay, Y.S. Kim, Anion exchange membrane fuel cells: Current status and remaining challenges, *Journal of Power Sources* 375 (2018) 170–184.
- [9] A. Sarapuu, E. Kibena-Pöldsepp, M. Borghei, K. Tammeveski, Electrocatalysis of oxygen reduction on heteroatom-doped nanocarbons and transition metal–nitrogen–carbon catalysts for alkaline membrane fuel cells, *Journal of Materials Chemistry A* 6 (2018) 776–804.
- [10] G. Wu, A. Santandreu, W. Kellogg, S. Gupta, O. Ogoke, H.G. Zhang, H.L. Wang, L.M. Dai, Carbon nanocomposite catalysts for oxygen reduction and evolution reactions: From nitrogen doping to transition-metal addition, *Nano Energy* 29 (2016) 83–110.
- [11] S. Mekhilef, R. Saidur, A. Safari, Comparative study of different fuel cell technologies, *Renewable & Sustainable Energy Reviews* 16 (2012) 981–989.
- [12] M.L. Perry, T.F. Fuller, A historical perspective of fuel cell technology in the 20th century, *Journal of the Electrochemical Society* 149 (2002) S59–S67.
- [13] Y. Wang, H. Yuan, A. Martinez, P. Hong, H. Xu, F.R. Bockmiller, Polymer electrolyte membrane fuel cell and hydrogen station networks for automobiles: Status, technology, and perspectives, *Advances in Applied Energy* 2 (2021) 100011.
- [14] L. Wang, X. Wan, S.Y. Liu, L. Xu, J.L. Shui, Fe-N-C catalysts for PEMFC: Progress towards the commercial application under DOE reference, *Journal of Energy Chemistry* 39 (2019) 77–87.

- [15] Y. Deng, J. Luo, B. Chi, H. Tang, J. Li, X. Qiao, Y. Shen, Y. Yang, C. Jia, P. Rao, S. Liao, X. Tian, Advanced Atomically Dispersed Metal-Nitrogen-Carbon Catalysts Toward Cathodic Oxygen Reduction in PEM Fuel Cells, *Advanced Energy Materials* 11 (2021) 2101222.
- [16] S. Hussain, H. Erikson, N. Kongi, A. Sarapuu, J. Solla-Gullón, G. Maia, A.M. Kannan, N. Alonso-Vante, K. Tammeveski, Oxygen reduction reaction on nanostructured Pt-based electrocatalysts: A review, *International Journal of Hydrogen Energy* 45 (2020) 31775–31797.
- [17] N. Ramaswamy, S. Mukerjee, Alkaline Anion-Exchange Membrane Fuel Cells: Challenges in Electrocatalysis and Interfacial Charge Transfer, *Chemical Reviews* 119 (2019) 11945–11979.
- [18] D.R. Dekel, Review of cell performance in anion exchange membrane fuel cells, *Journal of Power Sources* 375 (2018) 158–169.
- [19] Z.F. Pan, L. An, T.S. Zhao, Z.K. Tang, Advances and challenges in alkaline anion exchange membrane fuel cells, *Progress in Energy and Combustion Science* 66 (2018) 141–175.
- [20] W.E. Mustain, Understanding how high-performance anion exchange membrane fuel cells were achieved: Component, interfacial, and cell-level factors, *Current Opinion in Electrochemistry* 12 (2018) 233–239.
- [21] M.R. Tarasevich, A. Sadkowski, E. Yeager, Oxygen Electrochemistry, in: B.E. Conway, J.O'M. Bockris, E. Yeager, S.U.M. Khan, R.E. White (Eds.), *Comprehensive Treatise of Electrochemistry*, Plenum Press, New York, vol. 7, 1983, pp. 301–398.
- [22] Y. Yang, C. R. Peltier, R. Zeng, R. Schimmenti, Q. Li, X. Huang, Z. Yan, G. Potsi, R. Selhorst, X. Lu, W. Xu, M. Tader, A. V. Soudackov, H. Zhang, M. Krumov, E. Murray, P. Xu, J. Hitt, L. Xu, H.-Y. Ko, B. G. Ernst, C. Bundschu, A. Luo, D. Markovich, M. Hu, C. He, H. Wang, J. Fang, R. A. DiStasio Jr., L. F. Kourkoutis, A. Singer, K. J. T. Noonan, L. Xiao, L. Zhuang, B. S. Pivovar, P. Zelenay, E. Herrero, J. M. Feliu, J. Suntivich, E. P. Giannelis, S. Hammes-Schiffer, T. Arias, M. Mavrikakis, T. E. Mallouk, J. D. Brock, D.A. Muller, F. J. DiSalvo, G. W. Coates, H. D. Abruña, *Electrocatalysis in Alkaline Media and Alkaline Membrane-Based Energy Technologies*, *Chemical Reviews* 122 (2022) 6117–6321.
- [23] J. Lilloja, E. Kibena-Pöldsepp, M. Merisalu, P. Rauwel, L. Matisen, A. Niilisk, E.S.F. Cardoso, G. Maia, V. Sammelseg, K. Tammeveski, An Oxygen Reduction Study of Graphene-Based Nanomaterials of Different Origin, *Catalysts* 6 (2016) 108.
- [24] I. Kruusenberg, J. Leis, M. Arulepp, K. Tammeveski, Oxygen reduction on carbon nanomaterial-modified glassy carbon electrodes in alkaline solution, *Journal of Solid State Electrochemistry* 14 (2010) 1269–1277.
- [25] R. Jäger, P.E. Kasatkin, E. Härk, E. Lust, Oxygen reduction on molybdenum carbide derived micromesoporous carbon electrode in alkaline solution, *Electrochemistry Communications* 35 (2013) 97–99.
- [26] G. Jürmann, K. Tammeveski, Electroreduction of oxygen on multi-walled carbon nanotubes modified highly oriented pyrolytic graphite electrodes in alkaline solution, *Journal of Electroanalytical Chemistry* 597 (2006) 119–126.
- [27] I. Palm, E. Kibena-Pöldsepp, J. Lilloja, M. Käärik, A. Kikas, V. Kisand, M. Merisalu, A. Treshchalov, P. Paiste, J. Leis, A. Tamm, V. Sammelseg, K. Tammeveski, Impact of ball-milling of carbide-derived carbons on the

- generation of hydrogen peroxide via electroreduction of oxygen in alkaline media, *Journal of Electroanalytical Chemistry* 878 (2020) 114690.
- [28] L.J. Yang, J.L. Shui, L. Du, Y.Y. Shao, J. Liu, L.M. Dai, Z. Hu, Carbon-Based Metal-Free ORR Electrocatalysts for Fuel Cells: Past, Present, and Future, *Advanced Materials* 31 (2019).
- [29] M. Vikkisk, I. Kruusenberg, S. Ratso, U. Joost, E. Shulga, I. Kink, P. Rauwel, K. Tammeveski, Enhanced electrocatalytic activity of nitrogen-doped multi-walled carbon nanotubes towards the oxygen reduction reaction in alkaline media, *RSC Advances* 5 (2015) 59495–59505.
- [30] S. Ratso, I. Kruusenberg, M. Vikkisk, U. Joost, E. Shulga, I. Kink, T. Kallio, K. Tammeveski, Highly active nitrogen-doped few-layer graphene/carbon nanotube composite electrocatalyst for oxygen reduction reaction in alkaline media, *Carbon* 73 (2014) 361–370.
- [31] S. Ratso, I. Kruusenberg, M. Käärik, M. Kook, R. Saar, M. Pärs, J. Leis, K. Tammeveski, Highly efficient nitrogen-doped carbide-derived carbon materials for oxygen reduction reaction in alkaline media, *Carbon* 113 (2017) 159–169.
- [32] L.T. Qu, Y. Liu, J.B. Baek, L.M. Dai, Nitrogen-Doped Graphene as Efficient Metal-Free Electrocatalyst for Oxygen Reduction in Fuel Cells, *ACS Nano* 4 (2010) 1321–1326.
- [33] Q.C. Wang, Y.J. Ji, Y.P. Lei, Y.B. Wang, Y.D. Wang, Y.Y. Li, S.Y. Wang, Pyridinic-N-Dominated Doped Defective Graphene as a Superior Oxygen Electrocatalyst for Ultrahigh-Energy-Density Zn-Air Batteries, *ACS Energy Letters* 3 (2018) 1183–1191.
- [34] K.P. Gong, F. Du, Z.H. Xia, M. Durstock, L.M. Dai, Nitrogen-Doped Carbon Nanotube Arrays with High Electrocatalytic Activity for Oxygen Reduction, *Science* 323 (2009) 760–764.
- [35] R. Sibul, E. Kibena-Pöldsepp, S. Ratso, M. Kook, M. Käärik, M. Merisalu, P. Paiste, J. Leis, V. Sammelselg, K. Tammeveski, Nitrogen-doped carbon-based electrocatalysts synthesised by ball-milling, *Electrochemistry Communications* 93 (2018) 39–43.
- [36] Z. Yang, Z. Yao, G.F. Li, G.Y. Fang, H.G. Nie, Z. Liu, X.M. Zhou, X. Chen, S.M. Huang, Sulfur-Doped Graphene as an Efficient Metal-free Cathode Catalyst for Oxygen Reduction, *ACS Nano* 6 (2012) 205–211.
- [37] A.M. El-Sawy, I.M. Mosa, D. Su, C.J. Guild, S. Khalid, R. Joesten, J.F. Rusling, S.L. Suib, Controlling the Active Sites of Sulfur-Doped Carbon Nanotube-Graphene Nanolobes for Highly Efficient Oxygen Evolution and Reduction Catalysis, *Advanced Energy Materials* 6 (2016) 1501966.
- [38] W.Q. Li, D.G. Yang, H.B. Chen, Y. Gao, H.M. Li, Sulfur-doped carbon nanotubes as catalysts for the oxygen reduction reaction in alkaline medium, *Electrochimica Acta* 165 (2015) 191–197.
- [39] R. Li, Z.D. Wei, X.L. Gou, W. Xu, Phosphorus-doped graphene nanosheets as efficient metal-free oxygen reduction electrocatalysts, *RSC Advances* 3 (2013) 9978–9984.
- [40] D.S. Yang, D. Bhattacharjya, S. Inamdar, J. Park, J.S. Yu, Phosphorus-Doped Ordered Mesoporous Carbons with Different Lengths as Efficient Metal-Free Electrocatalysts for Oxygen Reduction Reaction in Alkaline Media, *Journal of the American Chemical Society* 134(2012) 16127–16130.

- [41] Z.H. Sheng, H.L. Gao, W.J. Bao, F.B. Wang, X.H. Xia, Synthesis of boron doped graphene for oxygen reduction reaction in fuel cells, *Journal of Materials Chemistry* 22 (2012) 390–395.
- [42] X.J. Sun, Y.W. Zhang, P. Song, J. Pan, L. Zhuang, W.L. Xu, W. Xing, Fluorine-Doped Carbon Blacks: Highly Efficient Metal-Free Electrocatalysts for Oxygen Reduction Reaction, *ACS Catalysis* 3 (2013) 1726–1729.
- [43] Z. Yao, H.G. Nie, Z. Yang, X.M. Zhou, Z. Liu, S.M. Huang, Catalyst-free synthesis of iodine-doped graphene via a facile thermal annealing process and its use for electrocatalytic oxygen reduction in an alkaline medium, *Chemical Communications* 48 (2012) 1027–1029.
- [44] R. Sibul, E. Kibena-Pöldsepp, U. Mäeorg, M. Merisalu, A. Kikas, V. Kisand, A. Treshchalov, V. Sammelseg, K. Tammeveski, Sulphur and nitrogen co-doped graphene-based electrocatalysts for oxygen reduction reaction in alkaline medium, *Electrochemistry Communications* 109 (2019) 106603.
- [45] M. Borghei, N. Laocharoen, E. Kibena-Pöldsepp, L.S. Johansson, J. Campbell, E. Kauppinen, K. Tammeveski, O.J. Rojas, Porous N,P-doped carbon from coconut shells with high electrocatalytic activity for oxygen reduction: Alternative to Pt-C for alkaline fuel cells, *Applied Catalysis B: Environmental* 204 (2017) 394–402.
- [46] S.Y. Wang, E. Iyyamperumal, A. Roy, Y.H. Xue, D.S. Yu, L.M. Dai, Vertically Aligned BCN Nanotubes as Efficient Metal-Free Electrocatalysts for the Oxygen Reduction Reaction: A Synergetic Effect by Co-Doping with Boron and Nitrogen, *Angewandte Chemie-International Edition* 50 (2011) 11756–11760.
- [47] I. Palm, E. Kibena-Pöldsepp, M. Mooste, J. Kozlova, M. Käärrik, A. Kikas, A. Treshchalov, J. Leis, V. Kisand, A. Tamm, Nitrogen and Phosphorus Dual-Doped Silicon Carbide-Derived Carbon/Carbon Nanotube Composite for the Anion-Exchange Membrane Fuel Cell Cathode, *ACS Applied Energy Materials* 5 (2022) 2949–2958.
- [48] C.Z. Zhu, H. Li, S.F. Fu, D. Du, Y.H. Lin, Highly efficient nonprecious metal catalysts towards oxygen reduction reaction based on three-dimensional porous carbon nanostructures, *Chemical Society Reviews* 45 (2016) 517–531.
- [49] M. Zhou, H.L. Wang, S.J. Guo, Towards high-efficiency nanoelectrocatalysts for oxygen reduction through engineering advanced carbon nanomaterials, *Chemical Society Reviews* 45 (2016) 1273–1307.
- [50] Z. Shi, J.J. Zhang, Z.S. Liu, H.J. Wang, D.P. Wilkinson, Current status of ab initio quantum chemistry study for oxygen electroreduction on fuel cell catalysts, *Electrochimica Acta* 51 (2006) 1905–1916.
- [51] Z.Q. Luo, S.H. Lim, Z.Q. Tian, J.Z. Shang, L.F. Lai, B. MacDonald, C. Fu, Z.X. Shen, T. Yu, J.Y. Lin, Pyridinic N doped graphene: synthesis, electronic structure, and electrocatalytic property, *Journal of Materials Chemistry* 21 (2011) 8038–8044.
- [52] S.K. Singh, K. Takeyasu, J. Nakamura, Active Sites and Mechanism of Oxygen Reduction Reaction Electrocatalysis on Nitrogen-Doped Carbon Materials, *Advanced Materials* 31 (2019) 1804297.
- [53] X. Liu, L.M. Dai, Carbon-based metal-free catalysts, *Nature Reviews Materials* 1 (2016) 16064.
- [54] P. Zhang, F. Sun, Z.H. Xiang, Z.G. Shen, J. Yun, D.P. Cao, ZIF-derived in situ nitrogen-doped porous carbons as efficient metal-free electrocatalysts for oxygen reduction reaction, *Energy & Environmental Science* 7 (2014) 442–450.

- [55] D.H. Guo, R. Shibuya, C. Akiba, S. Saji, T. Kondo, J. Nakamura, Active sites of nitrogen-doped carbon materials for oxygen reduction reaction clarified using model catalysts, *Science* 351 (2016) 361–365.
- [56] D.S. Geng, Y. Chen, Y.G. Chen, Y.L. Li, R.Y. Li, X.L. Sun, S.Y. Ye, S. Knights, High oxygen-reduction activity and durability of nitrogen-doped graphene, *Energy & Environmental Science* 4 (2011) 760–764.
- [57] Z.Y. Lin, G.H. Waller, Y. Liu, M.L. Liu, C.P. Wong, Simple preparation of nanoporous few-layer nitrogen-doped graphene for use as an efficient electrocatalyst for oxygen reduction and oxygen evolution reactions, *Carbon* 53 (2013) 130–136.
- [58] W.H. He, C.H. Jiang, J.B. Wang, L.H. Lu, High-Rate Oxygen Electroreduction over Graphitic-N Species Exposed on 3D Hierarchically Porous Nitrogen-Doped Carbons, *Angewandte Chemie-International Edition* 53 (2014) 9503–9507.
- [59] T. Sharifi, G. Hu, X.E. Jia, T. Wagberg, Formation of Active Sites for Oxygen Reduction Reactions by Transformation of Nitrogen Functionalities in Nitrogen-Doped Carbon Nanotubes, *ACS Nano* 6 (2012) 8904–8912.
- [60] S. Kabir, K. Artyushkova, A. Serov, P. Atanassov, Role of Nitrogen Moieties in N-Doped 3D-Graphene Nanosheets for Oxygen Electroreduction in Acidic and Alkaline Media, *ACS Applied Materials & Interfaces* 10 (2018) 11623–11632.
- [61] L.F. Lai, J.R. Potts, D. Zhan, L. Wang, C.K. Poh, C.H. Tang, H. Gong, Z.X. Shen, L.Y. Jianyi, R.S. Ruoff, Exploration of the active center structure of nitrogen-doped graphene-based catalysts for oxygen reduction reaction, *Energy & Environmental Science* 5 (2012) 7936–7942.
- [62] D.C. Wei, Y.Q. Liu, Y. Wang, H.L. Zhang, L.P. Huang, G. Yu, Synthesis of N-Doped Graphene by Chemical Vapor Deposition and Its Electrical Properties, *Nano Letters* 9 (2009) 1752–1758.
- [63] Z.X. Wu, M. Song, J. Wang, X. Liu, Recent Progress in Nitrogen-Doped Metal-Free Electrocatalysts for Oxygen Reduction Reaction, *Catalysts* 8 (2018) 196.
- [64] S. Ratso, A. Zitolo, M. Käärrik, M. Merisalu, A. Kikas, V. Kisand, M. Rähn, P. Paiste, J. Leis, V. Sammelseig, S. Holdcroft, F. Jaouen, K. Tammeveski, Non-precious metal cathodes for anion exchange membrane fuel cells from ball-milled iron and nitrogen doped carbide-derived carbons, *Renewable Energy* 167 (2021) 800–810.
- [65] K. Kisand, A. Sarapuu, D. Danilian, A. Kikas, V. Kisand, M. Rähn, A. Treshchakov, M. Käärrik, M. Merisalu, P. Paiste, J. Aruväli, J. Leis, V. Sammelseig, S. Holdcroft, K. Tammeveski, Transition metal-containing nitrogen-doped nano-carbon catalysts derived from 5-methylresorcinol for anion exchange membrane fuel cell application, *Journal of Colloid and Interface Science* 584 (2021) 263–274.
- [66] O.Y. Bisen, R. Nandan, A.K. Yadav, B. Pavithra, K.K. Nanda, In situ self-organization of uniformly dispersed Co-N-C centers at moderate temperature without a sacrificial subsidiary metal, *Green Chemistry* 23 (2021) 3115–3126.
- [67] S. Kattel, P. Atanassov, B. Kiefer, Catalytic activity of Co-N-x/C electrocatalysts for oxygen reduction reaction: a density functional theory study, *Physical Chemistry Chemical Physics* 15 (2013) 148–153.
- [68] K. Artyushkova, A. Serov, S. Rojas-Carbonell, P. Atanassov, Chemistry of Multitudinous Active Sites for Oxygen Reduction Reaction in Transition Metal-Nitrogen-Carbon Electrocatalysts, *Journal of Physical Chemistry C* 119 (2015) 25917–25928.

- [69] I. Matanovic, K. Artyushkova, P. Atanassov, Understanding PGM-free catalysts by linking density functional theory calculations and structural analysis: Perspectives and challenges, *Current Opinion in Electrochemistry* 9 (2018) 137–144.
- [70] K. Strickland, M.W. Elise, Q.Y. Jia, U. Tylus, N. Ramaswamy, W.T. Liang, M.T. Sougrati, F. Jaouen, S. Mukerjee, Highly active oxygen reduction non-platinum group metal electrocatalyst without direct metal-nitrogen coordination, *Nature Communications* 6 (2015) 7343.
- [71] Q. Jia, N. Ramaswamy, H. Hafiz, U. Tylus, K. Strickland, G. Wu, B. Barbiellini, A. Bansil, E.F. Holby, P. Zelenay, S. Mukerjee, Experimental Observation of Redox-Induced Fe-N Switching Behavior as a Determinant Role for Oxygen Reduction Activity, *ACS Nano* 9 (2015) 12496–12505.
- [72] N. Ramaswamy, U. Tylus, Q.Y. Jia, S. Mukerjee, Activity Descriptor Identification for Oxygen Reduction on Nonprecious Electrocatalysts: Linking Surface Science to Coordination Chemistry, *Journal of the American Chemical Society* 135 (2013) 15443–15449.
- [73] K. Tammeveski, J.H. Zagal, Electrocatalytic oxygen reduction on transition metal macrocyclic complexes for anion exchange membrane fuel cell application, *Current Opinion in Electrochemistry* 9 (2018) 207–213.
- [74] C.Z. Loyola, G. Abarca, S. Ureta-Zanartu, C. Aliaga, J.H. Zagal, M.T. Sougrati, F. Jaouen, W. Orellana, F. Tasca, Insights into the electronic structure of Fe penta-coordinated complexes. Spectroscopic examination and electrochemical analysis for the oxygen reduction and oxygen evolution reactions, *Journal of Materials Chemistry A* 9 (2021) 23802–23816.
- [75] Y. Kumar, E. Kibena-Pöldsepp, J. Kozlova, M. Rähn, A. Treshchalov, A. Kikas, V. Kisand, J. Aruväli, A. Tamm, J.C. Douglin, S.J. Folkman, I. Gelmetti, F.A. Garces-Pineda, J.R. Galan-Mascaros, D.R. Dekel, K. Tammeveski, Bifunctional Oxygen Electrocatalysis on Mixed Metal Phthalocyanine-Modified Carbon Nanotubes Prepared via Pyrolysis, *ACS Applied Materials & Interfaces* 13 (2021) 41507–41516.
- [76] M.P. Oyarzun, N. Silva, D. Cortes-Arriagada, J.F. Silva, I.O. Ponce, M. Flores, K. Tammeveski, D. Belanger, A. Zitolo, F. Jaouen, J.H. Zagal, Enhancing the electrocatalytic activity of Fe phthalocyanines for the oxygen reduction reaction by the presence of axial ligands: Pyridine-functionalized single-walled carbon nanotubes, *Electrochimica Acta* 398 (2021) 139263.
- [77] F.A. Westerhaus, R.V. Jagadeesh, G. Wienhofer, M.M. Pohl, J. Radnik, A.E. Surkus, J. Rabeah, K. Junge, H. Junge, M. Nielsen, A. Bruckner, M. Beller, Heterogenized cobalt oxide catalysts for nitroarene reduction by pyrolysis of molecularly defined complexes, *Nature Chemistry* 5 (2013) 537–543.
- [78] H.Z. Yang, L. Shang, Q.H. Zhang, R. Shi, G.I.N. Waterhouse, L. Gu, T.R. Zhang, A universal ligand mediated method for large scale synthesis of transition metal single atom catalysts, *Nature Communications* 10 (2019) 4585.
- [79] R. Praats, M. Käärrik, A. Kikas, V. Kisand, J. Aruväli, P. Paiste, M. Merisalu, A. Sarapuu, J. Leis, V. Sammelselg, J.C. Douglin, D.R. Dekel, K. Tammeveski, Electroreduction of oxygen on cobalt phthalocyanine-modified carbide-derived carbon/carbon nanotube composite catalysts, *Journal of Solid State Electrochemistry* 25 (2021) 57–71.

- [80] M. Mamlouk, S.M.S. Kumar, P. Gouerec, K. Scott, Electrochemical and fuel cell evaluation of Co based catalyst for oxygen reduction in anion exchange polymer membrane fuel cells, *Journal of Power Sources* 196 (2011) 7594–7600.
- [81] K. Li, Y. Li, W.C. Peng, G.L. Zhang, F.B. Zhang, X.B. Fan, Bimetallic Iron-Cobalt Catalysts and Their Applications in Energy-Related Electrochemical Reactions, *Catalysts* 9 (2019) 762.
- [82] R. Sibul, E. Kibena-Pöldsepp, S. Ratso, M. Kook, M.T. Sougrati, M. Käärik, M. Merisalu, J. Aruväli, P. Paiste, A. Treshchalov, J. Leis, V. Kisand, V. Sammelselg, S. Holdcroft, F. Jaouen, K. Tammeveski, Iron- and Nitrogen-Doped Graphene-Based Catalysts for Fuel Cell Applications, *ChemElectroChem* 7 (2020) 1739–1747.
- [83] H. Lee, M.J. Kim, T. Lim, Y.E. Sung, H.J. Kim, H.N. Lee, O.J. Kwon, Y.H. Cho, A facile synthetic strategy for iron, aniline-based non-precious metal catalysts for polymer electrolyte membrane fuel cells, *Scientific Reports* 7 (2017) 5396.
- [84] X.G. Fu, Y.R. Liu, X.P. Cao, J.T. Jin, Q. Liu, J.Y. Zhang, FeCo-N-x embedded graphene as high performance catalysts for oxygen reduction reaction, *Applied Catalysis B: Environmental* 130 (2013) 143–151.
- [85] M. Mooste, E. Kibena-Pöldsepp, V. Vassiljeva, A. Kikas, M. Käärik, J. Kozlova, V. Kisand, M. Kõlaviir, S. Cavaliere, J. Leis, A. Krumme, V. Sammelselg, S. Holdcroft, K. Tammeveski, Electrospun Polyacrylonitrile-Derived Co or Fe Containing Nanofibre Catalysts for Oxygen Reduction Reaction at the Alkaline Membrane Fuel Cell Cathode, *ChemCatChem* 12 (2020) 4568–4581.
- [86] Y.Y. Sun, L. Silviali, N.R. Sahraie, W. Ju, J.K. Li, A. Zitolo, S. Li, A. Bagger, L. Arnarson, X.L. Wang, T. Moeller, D. Bernsmeier, J. Rossmesl, F. Jaouen, P. Strasser, Activity-Selectivity Trends in the Electrochemical Production of Hydrogen Peroxide over Single-Site Metal-Nitrogen-Carbon Catalysts, *Journal of the American Chemical Society* 141 (2019) 12372–12381.
- [87] K. Artyushkova, S. Rojas-Carbonell, C. Santoro, E. Weiler, A. Serov, R. Awais, R.R. Gokhale, P. Atanassov, Correlations between Synthesis and Performance of Fe-Based PGM-Free Catalysts in Acidic and Alkaline Media: Evolution of Surface Chemistry and Morphology, *ACS Applied Energy Materials* 2 (2019) 5406–5418.
- [88] P.G. Santori, F.D. Speck, S. Cherevko, H.A. Firouzjaie, X. Peng, W.E. Mustain, F. Jaouen, High Performance FeNC and Mn-oxide/FeNC Layers for AEMFC Cathodes, *Journal of the Electrochemical Society* 167 (2020) 134505.
- [89] F.Z. Li, P. Shi, J.T. Wu, X.M. Qi, Y. Liu, G.L. Li, Trace Bimetallic Iron/Manganese Co-Doped N-Ketjenblack Carbon Electrocatalyst for Robust Oxygen Reduction Reaction, *Journal of the Electrochemical Society* 168 (2021) 060502.
- [90] W.K. Zhu, Y.B. Pei, J.C. Douglin, J.F. Zhang, H.Y. Zhao, J.D. Xue, Q.F. Wang, R. Li, Y.Z. Qin, Y. Yin, D.R. Dekel, M.D. Guiver, Multi-scale study on bifunctional Co/Fe-N-C cathode catalyst layers with high active site density for the oxygen reduction reaction, *Applied Catalysis B: Environmental* 299 (2021) 120656.
- [91] T.T. Gao, Z.Y. Jin, Y.J. Zhang, G.Q. Tan, H.Y. Yuan, D. Xiao, Coupling cobalt-iron bimetallic nitrides and N-doped multi-walled carbon nanotubes as high-performance bifunctional catalysts for oxygen evolution and reduction reaction, *Electrochimica Acta* 258 (2017) 51–60.

- [92] L.L. Chen, Y.L. Zhang, L.L. Dong, W.X. Yang, X.J. Liu, L. Long, C.Y. Liu, S.J. Dong, J.B. Jia, Synergistic effect between atomically dispersed Fe and Co metal sites for enhanced oxygen reduction reaction, *Journal of Materials Chemistry A* 8 (2020) 4369–4375.
- [93] M. Zhang, J.P. Gao, W. Hong, X.X. Wang, Q. Tian, Z.L. An, L.Y. Wang, H.D. Yao, Y. Liu, X.X. Zhao, H.X. Qiu, Bimetallic Mn and Co encased within bamboo-like N-doped carbon nanotubes as efficient oxygen reduction reaction electrocatalysts, *Journal of Colloid and Interface Science* 537 (2019) 238–246.
- [94] K.Q. Zhong, Y. Wang, Q.K. Wu, H.H. You, H.G. Zhang, M.H. Su, R.Y. Liang, J.L. Zuo, S.R. Yang, J.F. Tang, Highly conductive skeleton Graphitic-C₃N₄ assisted Fe-based metal-organic frameworks derived porous bimetallic carbon nanofiber for enhanced oxygen-reduction performance in microbial fuel cells, *Journal of Power Sources* 467 (2020) 228313.
- [95] Z. Yan, H. Qi, X. Bai, K. Huang, Y.R. Chen, Q. Wang, Mn doping of cobalt oxynitride coupled with N-rGO nanosheets hybrid as a highly efficient electrocatalyst for oxygen reduction and oxygen evolution reaction, *Electrochimica Acta* 283 (2018) 548–559.
- [96] J. Masa, W. Xia, M. Muhler, W. Schuhmann, On the Role of Metals in Nitrogen-Doped Carbon Electrocatalysts for Oxygen Reduction, *Angewandte Chemie-International Edition* 54 (2015) 10102–10120.
- [97] L. Li, B. Huang, X. Tang, Y. Hong, W. Zhai, T. Hu, K. Yuan, Y. Chen, Recent Developments of Microenvironment Engineering of Single-Atom Catalysts for Oxygen Reduction toward Desired Activity and Selectivity, *Advanced Functional Materials* 31 (2021) 2103857.
- [98] W. Xu, H. Tang, H. Gu, H. Xi, P.F. Wu, B. Liang, Q. Liu, W. Chen, Research Progress of Asymmetrically Coordinated Single-Atom Catalysts for Electrocatalytic Reactions, *Journal of Materials Chemistry A* (2022), *in press*, DOI: 10.1039/D2TA03034A.
- [99] H.B. Tan, J. Tang, J. Kim, Y.V. Kaneti, Y.M. Kang, Y. Sugahara, Y. Yamauchi, Rational design and construction of nanoporous iron- and nitrogen-doped carbon electrocatalysts for oxygen reduction reaction, *Journal of Materials Chemistry A* 7 (2019) 1380–1393.
- [100] P. Trogadas, T.F. Fuller, P. Strasser, Carbon as catalyst and support for electrochemical energy conversion, *Carbon* 75 (2014) 5–42.
- [101] T. Soboleva, X.S. Zhao, K. Mallek, Z. Xie, T. Navessin, S. Holdcroft, On the Micro-, Meso- and Macroporous Structures of Polymer Electrolyte Membrane Fuel Cell Catalyst Layers, *ACS Applied Materials & Interfaces* 2 (2010) 375–384.
- [102] L. Borchardt, M. Oschatz, S. Kaskel, Tailoring porosity in carbon materials for supercapacitor applications, *Materials Horizons* 1 (2014) 157–168.
- [103] W.T. Gu, G. Yushin, Review of nanostructured carbon materials for electrochemical capacitor applications: advantages and limitations of activated carbon, carbide-derived carbon, zeolite-templated carbon, carbon aerogels, carbon nanotubes, onion-like carbon, and graphene, *Wiley Interdisciplinary Reviews-Energy and Environment* 3(2014) 424–473.
- [104] C. Largeot, C. Portet, J. Chmiola, P.L. Taberna, Y. Gogotsi, P. Simon, Relation between the ion size and pore size for an electric double-layer capacitor, *Journal of the American Chemical Society* 130 (2008) 2730–2731.

- [105] M. Arulepp, J. Leis, M. Lätt, F. Miller, K. Rumma, E. Lust, A.F. Burke, The advanced carbide-derived carbon based supercapacitor, *Journal of Power Sources* 162 (2006) 1460–1466.
- [106] S. Urbonaite, J.M. Juarez-Galan, J. Leis, F. Rodriguez-Reinoso, G. Svensson, Porosity development along the synthesis of carbons from metal carbides, *Microporous and Mesoporous Materials* 113 (2008) 14–21.
- [107] A. Jänes, T. Thomberg, H. Kurig, E. Lust, Nanoscale fine-tuning of porosity of carbide-derived carbon prepared from molybdenum carbide, *Carbon* 47 (2009) 23–29.
- [108] H.J. Dai, Carbon nanotubes: opportunities and challenges, *Surface Science* 500 (2002) 218–241.
- [109] S. Ratso, I. Kruusenberg, A. Sarapuu, P. Rauwel, R. Saar, U. Joost, J. Aruväli, P. Kanninen, T. Kallio, K. Tammeveski, Enhanced oxygen reduction reaction activity of iron-containing nitrogen-doped carbon nanotubes for alkaline direct methanol fuel cell application, *Journal of Power Sources* 332 (2016) 129–138.
- [110] K.S. Novoselov, A.K. Geim, S.V. Morozov, D. Jiang, Y. Zhang, S.V. Dubonos, I.V. Grigorieva, A.A. Firsov, Electric field effect in atomically thin carbon films, *Science* 306 (2004) 666–669.
- [111] W.W. Liu, S.P. Chai, A.R. Mohamed, U. Hashim, Synthesis and characterization of graphene and carbon nanotubes: A review on the past and recent developments, *Journal of Industrial and Engineering Chemistry* 20 (2014) 1171–1185.
- [112] A. Martin, A. Escarpa, Graphene: The cutting-edge interaction between chemistry and electrochemistry, *Trac-Trends in Analytical Chemistry* 56 (2014) 13–26.
- [113] M.M. Liu, R.Z. Zhang, W. Chen, Graphene-Supported Nanoelectrocatalysts for Fuel Cells: Synthesis, Properties, and Applications, *Chemical Reviews* 114 (2014) 5117–5160.
- [114] P.F. Zhang, H.Y. Zhu, S. Dai, Porous Carbon Supports: Recent Advances with Various Morphologies and Compositions, *ChemCatChem* 7 (2015) 2788–2805.
- [115] C.M. Ghimbeu, L. Vidal, L. Delmotte, J.M. Le Meins, C. Vix-Guterl, Catalyst-free soft-template synthesis of ordered mesoporous carbon tailored using phloroglucinol/glyoxylic acid environmentally friendly precursors, *Green Chemistry* 16 (2014) 3079–3088.
- [116] A. Eftekhari, Z.Y. Fan, Ordered mesoporous carbon and its applications for electrochemical energy storage and conversion, *Materials Chemistry Frontiers* 1 (2017) 1001–1027.
- [117] C. Li, Q. Li, Y.V. Kaneti, D. Hou, Y. Yamauchi, Y.Y. Mai, Self-assembly of block copolymers towards mesoporous materials for energy storage and conversion systems, *Chemical Society Reviews* 49 (2020) 4681–4736.
- [118] L. Chuenchom, R. Kraehnert, B.M. Smarsly, Recent progress in soft-templating of porous carbon materials, *Soft Matter* 8 (2012) 10801–10812.
- [119] R.T. Mayes, C. Tsouris, J.O. Kiggans, S.M. Mahurin, D.W. DePaoli, S. Dai, Hierarchical ordered mesoporous carbon from phloroglucinol-glyoxal and its application in capacitive deionization of brackish water, *Journal of Materials Chemistry* 20 (2010) 8674–8678.
- [120] M. Hren, M. Bozic, D. Fakin, K.S. Kleinschek, S. Gorgieva, Alkaline membrane fuel cells: anion exchange membranes and fuels, *Sustainable Energy & Fuels* 5 (2021) 604–637.

- [121] R. Gutru, Z. Turtayeva, F.N. Xu, G. Maranzana, B. Vigolo, A. Desforges, A comprehensive review on water management strategies and developments in anion exchange membrane fuel cells, *International Journal of Hydrogen Energy* 45 (2020) 19642–19663.
- [122] J.R. Varcoe, R.C.T. Slade, E.L.H. Yee, S.D. Poynton, D.J. Driscoll, D.C. Apperley, Poly(ethylene-co-tetrafluoroethylene)-derived radiation-grafted anion-exchange membrane with properties specifically tailored for application in metal-cation-free alkaline polymer electrolyte fuel cells, *Chemistry of Materials* 19 (2007) 2686–2693.
- [123] S. Gu, R. Cai, T. Luo, K. Jensen, C. Contreras, Y.S. Yan, Quaternary Phosphonium-Based Polymers as Hydroxide Exchange Membranes, *ChemSusChem* 3 (2010) 555–558.
- [124] D.S. Kim, C.H. Fujimoto, M.R. Hibbs, A. Labouriau, Y.K. Choe, Y.S. Kim, Resonance Stabilized Perfluorinated Ionomers for Alkaline Membrane Fuel Cells, *Macromolecules* 46 (2013) 7826–7833.
- [125] Y. Wang, G.W. Wang, G.W. Li, B. Huang, J. Pan, Q. Liu, J.J. Han, L. Xiao, J.T. Lu, L. Zhuang, Pt-Ru catalyzed hydrogen oxidation in alkaline media: oxophilic effect or electronic effect?, *Energy & Environmental Science* 8 (2015) 177–181.
- [126] R.B. Kaspar, M.P. Letterio, J.A. Wittkopf, K. Gong, S. Gu, Y.S. Yan, Manipulating Water in High-Performance Hydroxide Exchange Membrane Fuel Cells through Asymmetric Humidification and Wetproofing, *Journal of the Electrochemical Society* 162 (2015) F483-F488.
- [127] C.E. Diesendruck, D.R. Dekel, Water - A key parameter in the stability of anion exchange membrane fuel cells, *Current Opinion in Electrochemistry* 9 (2018) 173–178.
- [128] T.J. Omasta, L. Wang, X. Peng, C.A. Lewis, J.R. Varcoe, W.E. Mustain, Importance of balancing membrane and electrode water in anion exchange membrane fuel cells, *Journal of Power Sources* 375 (2018) 205–213.
- [129] T.J. Omasta, A.M. Park, J.M. LaManna, Y.F. Zhang, X. Peng, L.Q. Wang, D.L. Jacobson, J.R. Varcoe, D.S. Hussey, B.S. Pivovar, W.E. Mustain, Beyond catalysis and membranes: visualizing and solving the challenge of electrode water accumulation and flooding in AEMFCs, *Energy & Environmental Science* 11 (2018) 551–558.
- [130] D. Strmcnik, M. Uchimura, C. Wang, R. Subbaraman, N. Danilovic, D. van der Vliet, A.P. Paulikas, V.R. Stamenkovic, N.M. Markovic, Improving the hydrogen oxidation reaction rate by promotion of hydroxyl adsorption, *Nature Chemistry* 5 (2013) 300–306.
- [131] J. Zheng, W.C. Sheng, Z.B. Zhuang, B.J. Xu, Y.S. Yan, Universal dependence of hydrogen oxidation and evolution reaction activity of platinum-group metals on pH and hydrogen binding energy, *Science Advances* 2 (2016) e150160.
- [132] L.Q. Wang, E. Magliocca, E.L. Cunningham, W.E. Mustain, S.D. Poynton, R. Escudero-Cid, M.M. Nasef, J. Ponce-Gonzalez, R. Bance-Souahli, R.C.T. Slade, D.K. Whelligan, J.R. Varcoe, An optimised synthesis of high performance radiation-grafted anion-exchange membranes, *Green Chemistry* 19 (2017) 831–843.
- [133] A.G. Wright, J.T. Fan, B. Britton, T. Weissbach, H.F. Lee, E.A. Kitching, T.J. Peckham, S. Holdcroft, Hexamethyl-p-terphenyl poly(benzimidazolium): a universal hydroxide-conducting polymer for energy conversion devices, *Energy & Environmental Science* 9 (2016) 2130–2142.

- [134] L. Osmieri, L. Pezzolato, S. Specchia, Recent trends on the application of PGM-free catalysts at the cathode of anion exchange membrane fuel cells, *Current Opinion in Electrochemistry* 9 (2018) 240–256.
- [135] F. Xiao, Y.C. Wang, Z.P. Wu, G.Y. Chen, F. Yang, S.Q. Zhu, K. Siddharth, Z.J. Kong, A.L. Lu, J.C. Li, C.J. Zhong, Z.Y. Zhou, M.H. Shao, Recent Advances in Electrocatalysts for Proton Exchange Membrane Fuel Cells and Alkaline Membrane Fuel Cells, *Advanced Materials* 33 (2021) 2006292.
- [136] K. Artyushkova, A. Serova, H. Doan, N. Danilovic, C.B. Capuano, T. Sakamoto, H. Kishi, S. Yamaguchi, S. Mukerjee, P. Atanassov, Application of X-ray photoelectron spectroscopy to studies of electrodes in fuel cells and electrolyzers, *Journal of Electron Spectroscopy and Related Phenomena* 231 (2019) 127–139.
- [137] A. Carlson, P. Shapturenka, B. Eriksson, G. Lindbergh, C. Lagergren, R.W. Lindström, Electrode parameters and operating conditions influencing the performance of anion exchange membrane fuel cells, *Electrochimica Acta* 277 (2018) 151–160.
- [138] C. Van Pham, M. Klingele, B. Britton, K.R. Vuyyuru, T. Unmuessig, S. Holdcroft, A. Fischer, S. Thiele, Tridoped Reduced Graphene Oxide as a Metal-Free Catalyst for Oxygen Reduction Reaction Demonstrated in Acidic and Alkaline Polymer Electrolyte Fuel Cells, *Advanced Sustainable Systems* 1 (2017) 1600038.
- [139] C.V. Rao, Y. Ishikawa, Activity, Selectivity, and Anion-Exchange Membrane Fuel Cell Performance of Virtually Metal-Free Nitrogen-Doped Carbon Nanotube Electrodes for Oxygen Reduction Reaction, *Journal of Physical Chemistry C* 116 (2012) 4340–4346.
- [140] J. Tong, W. Ma, L. Bo, T. Li, W. Li, Y. Li, Q. Zhang, Nitrogen-doped hollow carbon spheres as highly effective multifunctional electrocatalysts for fuel cells, Zn–air batteries, and water-splitting electrolyzers, *Journal of Power Sources* 441 (2019) 227166.
- [141] Y.J. Sa, C. Park, H.Y. Jeong, S.H. Park, Z. Lee, K.T. Kim, G.G. Park, S.H. Joo, Carbon Nanotubes/Heteroatom-Doped Carbon Core-Sheath Nanostructures as Highly Active, Metal-Free Oxygen Reduction Electrocatalysts for Alkaline Fuel Cells, *Angewandte Chemie-International Edition* 53 (2014) 4102–4106.
- [142] J.W.F. To, J.W.D. Ng, S. Siahrostami, A.L. Koh, Y.J. Lee, Z.H. Chen, K.D. Fong, S.C. Chen, J.J. He, W.G. Bae, J. Wilcox, H.Y. Jeong, K. Kim, F. Studt, J.K. Nørskov, T.F. Jaramillo, Z.N. Bao, High-performance oxygen reduction and evolution carbon catalysis: From mechanistic studies to device integration, *Nano Research* 10 (2017) 1163–1177.
- [143] I. Kruusenberg, D. Ramani, S. Ratso, U. Joost, R. Saar, P. Rauwel, A.M. Kannan, K. Tammeveski, Cobalt-Nitrogen Co-doped Carbon Nanotube Cathode Catalyst for Alkaline Membrane Fuel Cells, *ChemElectroChem* 3 (2016) 1455–1465.
- [144] S. Ratso, I. Kruusenberg, M. Käärrik, M. Kook, L. Puust, R. Saar, J. Leis, K. Tammeveski, Highly efficient transition metal and nitrogen co-doped carbide-derived carbon electrocatalysts for anion exchange membrane fuel cells, *Journal of Power Sources* 375 (2018) 233–243.
- [145] X. Peng, T.J. Omasta, E. Magliocca, L.Q. Wang, J.R. Varcoe, W.E. Mustain, Nitrogen-doped Carbon-CoO_x Nanohybrids: A Precious Metal Free Cathode that Exceeds 1.0 W cm⁻² Peak Power and 100 h Life in Anion-Exchange Membrane Fuel Cells, *Angewandte Chemie-International Edition* 58 (2019) 1046–1051.

- [146] M. Sharma, J.H. Jang, D.Y. Shin, J.A. Kwon, D.H. Lim, D. Choi, H. Sung, J. Jang, S.Y. Lee, K.Y. Lee, H.Y. Park, N. Jung, S.J. Yoo, Work function-tailored graphene via transition metal encapsulation as a highly active and durable catalyst for the oxygen reduction reaction, *Energy & Environmental Science* 12 (2019) 2200–2211.
- [147] Y. Wang, Y. Yang, S.F. Jia, X.M. Wang, K.J. Lyu, Y.Q. Peng, H. Zheng, X. Wei, H. Ren, L. Xiao, J.B. Wang, D.A. Muller, H.D. Abruna, B.O.E. Hwang, J.T. Lu, L. Zhuang, Synergistic Mn-Co catalyst outperforms Pt on high-rate oxygen reduction for alkaline polymer electrolyte fuel cells, *Nature Communications* 10 (2019) 1506.
- [148] A. Sokka, M. Mooste, M. Käärrik, V. Gudkova, J. Kozlova, A. Kikas, V. Kisand, A. Treshchalov, A. Tamm, P. Paiste, J. Aruväli, J. Leis, A. Krumme, S. Holdcroft, S. Cavaliere, F. Jaouen, K. Tammeveski, Iron and cobalt containing electrospun carbon nanofibre-based cathode catalysts for anion exchange membrane fuel cell, *International Journal of Hydrogen Energy* 46 (2021) 31275–31287.
- [149] H. Ren, Y. Wang, Y. Yang, X. Tang, Y.Q. Peng, H.Q. Peng, L. Xiao, J.T. Lu, H.D. Abruna, L. Zhuang, Fe/N/C Nanotubes with Atomic Fe Sites: A Highly Active Cathode Catalyst for Alkaline Polymer Electrolyte Fuel Cells, *ACS Catalysis* 7 (2017) 6485–6492.
- [150] X. Peng, V. Kashyap, B. Ng, S. Kurungot, L.Q. Wang, J.R. Varcoe, W.E. Mustain, High-Performing PGM-Free AEMFC Cathodes from Carbon-Supported Cobalt Ferrite Nanoparticles, *Catalysts* 9 (2019) 264.
- [151] J. Lilloja, M. Mooste, E. Kibena-Pöldsepp, A. Sarapuu, B. Zulevi, A. Kikas, H.M. Piirsoo, A. Tamm, V. Kisand, S. Holdcroft, A. Serov, K. Tammeveski, Mesoporous iron-nitrogen co-doped carbon material as cathode catalyst for the anion exchange membrane fuel cell, *Journal of Power Sources Advances* 8 (2021) 100052.
- [152] S.T. Thompson, D. Peterson, D. Ho, D. Papageorgopoulos, Perspective-The Next Decade of AEMFCs: Near-Term Targets to Accelerate Applied R&D, *Journal of the Electrochemical Society* 167 (2020) 084514.
- [153] H. Adabi, P.G. Santori, A. Shakouri, X. Peng, K. Yassin, I.G. Rasin, S. Brandon, D.R. Dekel, N.U. Hassan, M.-T. Sougrati, A. Zitolo, J.R. Varcoe, J.R. Regalbuto, F. Jaouen, W.E. Mustain, Understanding how single-atom site density drives the performance and durability of PGM-free Fe–N–C cathodes in anion exchange membrane fuel cells, *Materials Today Advances* 12 (2021) 100179.
- [154] W.E. Mustain, M. Chatenet, M. Page, Y.S. Kim, Durability challenges of anion exchange membrane fuel cells, *Energy & Environmental Science* 13 (2020) 2805–2838.
- [155] T.B. Ferriday, P.H. Middleton, Alkaline fuel cell technology-A review, *International Journal of Hydrogen Energy* 46 (2021) 18489–18510.
- [156] G. Das, J.H. Choi, P.K.T. Nguyen, D.J. Kim, Y.S. Yoon, Anion Exchange Membranes for Fuel Cell Application: A Review, *Polymers* 14 (2022) 1197.
- [157] A. Sadezky, H. Muckenhuber, H. Grothe, R. Niessner, U. Pöschl, Raman microspectroscopy of soot and related carbonaceous materials: spectral analysis and structural information, *Carbon* 43 (2005) 1731–1742.
- [158] A.J. Bard, L.R. Faulkner, *Electrochemical Methods*, 2nd ed., Wiley, New York, 2001.

- [159] R.E. Davis, G.L. Horvath, C.W. Tobias, The solubility and diffusion coefficient of oxygen in potassium hydroxide solutions, *Electrochimica Acta* 12 (1967) 287–297.
- [160] D.R. Lide, *CRC Handbook of Chemistry and Physics*, 82nd ed., CRC Press, Boca Raton, 2001.
- [161] U.A. Paulus, T.J. Schmidt, H.A. Gasteiger, R.J. Behm, Oxygen reduction on a high-surface area Pt/Vulcan carbon catalyst: a thin-film rotating ring-disk electrode study, *Journal of Electroanalytical Chemistry* 495 (2001) 134–145.
- [162] M. Groenewolt, M. Antonietti, Synthesis of g-C₃N₄ nanoparticles in mesoporous silica host matrices, *Advanced Materials* 17 (2005) 1789–1792.
- [163] A. Thomas, A. Fischer, F. Goettmann, M. Antonietti, J.O. Muller, R. Schlogl, J.M. Carlsson, Graphitic carbon nitride materials: variation of structure and morphology and their use as metal-free catalysts, *Journal of Materials Chemistry* 18 (2008) 4893–4908.
- [164] J.H. Liu, T.K. Zhang, Z.C. Wang, G. Dawson, W. Chen, Simple pyrolysis of urea into graphitic carbon nitride with recyclable adsorption and photocatalytic activity, *Journal of Materials Chemistry* 21 (2011) 14398–14401.
- [165] F.P. Pan, J.T. Jin, X.G. Fu, Q. Liu, J.Y. Zhang, Advanced Oxygen Reduction Electrocatalyst Based on Nitrogen-Doped Graphene Derived from Edible Sugar and Urea, *ACS Applied Materials & Interfaces* 5 (2013) 11108–11114.
- [166] A.C. Ferrari, J. Robertson, Interpretation of Raman spectra of disordered and amorphous carbon, *Physical Review B* 61 (2000) 14095–14107.
- [167] I.V. Stankevich, M.V. Nikerov, D.A. Bochvar, The structural chemistry of crystalline carbon: geometry, stability, and electronic spectrum, *Russian Chemical Reviews* 53 (1984) 640.
- [168] M. Zoraghi, J. Barzola-Quiquia, M. Stiller, A. Setzer, P. Esquinazi, G.H. Kloess, T. Muenster, T. Luhmann, I. Estrela-Lopis, Influence of rhombohedral stacking order in the electrical resistance of bulk and mesoscopic graphite, *Physical Review B* 95 (2017) 045308.
- [169] P. Scherrer, Estimation of the size and internal structure of colloidal particles by means of röntgen, *Nachr. Ges. Wiss. Göttingen* 2 (1918) 96–100.
- [170] B. Britton, S. Holdcroft, The Control and Effect of Pore Size Distribution in AEMFC Catalyst Layers, *Journal of the Electrochemical Society* 163 (2016) F353-F358.
- [171] M. Thommes, K. Kaneko, A.V. Neimark, J.P. Olivier, F. Rodriguez-Reinoso, J. Rouquerol, K.S.W. Sing, Physisorption of gases, with special reference to the evaluation of surface area and pore size distribution (IUPAC Technical Report), *Pure and Applied Chemistry* 87 (2015) 1051–1069.
- [172] Y. Kouketsu, T. Mizukami, H. Mori, S. Endo, M. Aoya, H. Hara, D. Nakamura, S. Wallis, A new approach to develop the Raman carbonaceous material geothermometer for low-grade metamorphism using peak width, *Island Arc* 23 (2014) 33–50.
- [173] B. Sljukic, C.E. Banks, R.G. Compton, An overview of the electrochemical reduction of oxygen at carbon-based modified electrodes, *Journal of the Iranian Chemical Society* 2 (2005) 1–25.
- [174] S. Martens, L. Asen, G. Ercolano, F. Dionigi, C. Zalitis, A. Hawkins, A.M. Bonastre, L. Seidl, A.C. Knoll, J. Sharman, P. Strasser, D. Jones, O. Schneider, A comparison of rotating disc electrode, floating electrode technique and

- membrane electrode assembly measurements for catalyst testing, *Journal of Power Sources* 392 (2018) 274–284.
- [175] X. Peng, D. Kulkarni, Y. Huang, T.J. Omasta, B. Ng, Y.W. Zheng, L.Q. Wang, J.M. LaManna, D.S. Hussey, J.R. Varcoe, I.V. Zenyuk, W.E. Mustain, Using operando techniques to understand and design high performance and stable alkaline membrane fuel cells, *Nature Communications* 11 (2020) 3561.
- [176] N. Ul Hassan, M. Mandal, G.R. Huang, H.A. Firouzjaie, P.A. Kohl, W.E. Mustain, Achieving High-Performance and 2000 h Stability in Anion Exchange Membrane Fuel Cells by Manipulating Ionomer Properties and Electrode Optimization, *Advanced Energy Materials* 10 (2020) 2001986.
- [177] H. Adabi, A. Shakouri, N. Ul Hassan, J.R. Varcoe, B. Zulevi, A. Serov, J.R. Regalbuto, W.E. Mustain, High-performing commercial Fe-N-C cathode electrocatalyst for anion-exchange membrane fuel cells, *Nature Energy* 6 (2021) 834–843.
- [178] S. Specchia, P. Atanassov, J.H. Zagal, Mapping transition metal-nitrogen-carbon catalyst performance on the critical descriptor diagram, *Current Opinion in Electrochemistry* 27 (2021) 100687.

9. SUMMARY IN ESTONIAN

Siirdemetallide ja lämmastikuga dopeeritud süsiniknanomaterjalid kui anioonvahetusmembraaniga kütuseelemendi katoodkatalüsaatorid

Doktoritöö eesmärk oli valmistada nanostruktuursetel süsinikmaterjalidel põhinevaid mitteväärismetallkatalüsaatoreid, uurida nende elektrokatalüütilisi omadusi hapniku redutseerumisreaktsioonil ning rakendusvõimalusi anioonvahetusmembraaniga kütuseelemendis (AEMFC). Lämmastiku ja siirdemetallidega dopeeritud katalüsaatorid valmistati kõrgtemperatuurisel pürolüüsil, kasutades erinevaid süsinikul põhinevaid alusmaterjale ning mitmesuguseid lämmastiku ja siirdemetallide lähteaineid. Valmistatud elektrokatalüsaatoreid testiti aluselises keskkonnas pöörleva ketaselektroodi (RDE) või pöörleva rõngas-ketaselektroodi (RRDE) meetodil, et uurida nii alusmaterjali kui ka dopeerimisel kasutatud lähteainete mõju saadud katalüsaatorite elektrokatalüütilisele aktiivsusele. Aktiivseimaid katalüsaatoreid rakendati AEMFC katoodil. Materjale karakteriseeriti põhjalikult, kasutades erinevaid füüsikalisi-keemilisi meetodeid.

Doktoritöö esimeses osas dopeeriti karbiidset päritolu süsiniku (CDC) ja süsiniknanotorude (CNT) segu lämmastiku [I] või lämmastiku ja koobaltiga [II]. Lämmastikuallikadena kasutati ditsüaaniamiidi, tsüaaniamiidi, ureat või melamiini. Valmistatud CDC/CNT komposiitmaterjalidel oli kõrge eripind ning mikro- ja mesoporsus. Röntgenfotoelektron-spektroskoopia (XPS) tulemuste kohaselt sisaldasid valmistatud materjalid sarnaseid lämmastikurühmasid, seega sobivad dopeerimiseks kõik kasutatud lämmastikuallikad. Sellest tulenevalt olid materjalid ka sarnase elektrokatalüütilise aktiivsusega hapniku redutseerumisel. Ehkki metallivabade lämmastikuga dopeeritud CDC/CNT materjalide aktiivsus oli üsna kõrge, paranes see koobaltit lisades veelgi, millest võib järeldada, et plaatinal põhinevate materjalidega võrreldava aktiivsuse saavutamiseks on vaja metall-lämmastik koordinatsiooniga (M-N_x) aktiivtsentreid. Siirdemetallide lisamise vajalikkus ilmnes ka AEMFC testis, kus Co-N-CDC/CNT katoodkatalüsaatoriga saavutati pea kaks korda kõrgem võimsustihedus kui N-CDC/CNT materjaliga.

Teises osas kasutati alusmaterjalidena grafeenilaadse (Gra) süsinikmaterjali ja CNT-de segu. Lämmastikuallikaks oli melamiin ning siirdemetallidena lisati rauda, koobaltit või neid mõlemat. Saadud Gra/CNT komposiidi morfoloogia oli sarnane CDC/CNT materjaliga ning dopeerimisel see oluliselt ei muutunud. RRDE katsed näitasid, et kõik kolm materjali olid väga aktiivsed ning Pt/C materjaliga võrreldavad katalüsaatorid hapniku elektroredutseerumise jaoks. Siirdemetallide erinev mõju selgus aga vesinikperoksiidiooni tekkeprotsendi määramisest, kus kõige rohkem peroksiidi moodustus koobaltit sisaldaval, vähim rauda sisaldaval ning vahepealne tekkeprotsent saadi bimetalse materjaliga. Erinevad tulemused saadi ka AEMFC testimisel, kus bimetalne CoFe-N-

Gra/CNT materjal oli parim ning samaväärne Pt/C katalüsaatoriga, millest võib järeldada, et kahe siirdemetalli koosmõju on tõhus.

Kolmandas osas kasutati taas CDC/CNT segu, kuid dopeerimisel kombineeriti 1,10-fenantroliin kui lämmastikuallikas siirdemetallide (Fe, Co või mõlemad) atsetaatidega ning vähendati metallisisaldust ühe massiprotsendini. Saadud materjalid olid morfoloogia poolest üsna sarnased nendega, mis valmistati töö esimeses osas. Erinevaid metalle sisaldavate materjalide hapniku redutseerumise elektrokatalüütiliste omaduste võrdlus oli kooskõlas töö teises osas saadud tulemustega. AEMFC katsetes kasutati selles töös ainsana ETFE-l baseeruvat membraani ning CoFe-N-CDC/CNT katoodkatalüsaatoriga saavutati kõrgeim maksimaalne võimsustihedus (P_{\max}) $1,12 \text{ W cm}^{-2}$.

Neljandas osas dopeeriti kommertsiaalset mesopoorset süsinikmaterjali (MPC) lämmastikuga, kasutades selleks 1,10-fenantroliini, ning siirdemetallidega (Fe, Co, Mn), saades järgmisi metallikombinatsioone sisaldavad katalüsaatorid: Fe, Co, CoFe, CoMn ja FeMn. Saadud MPC-l põhinevatel materjalidel oli bimodaalne mesopoorne struktuur pooride diameetritega ~ 7 ja 25–35 nm. RRDE katses näitasid parimat ja omavahel võrreldavat hapniku elektroredutseerumise aktiivsust raual põhinevad katalüsaatorid (Fe-N-MPC, CoFe-N-MPC ja FeMn-N-MPC). Enam peroksiidi moodustus koobaltit sisaldavatel materjalidel ning vähem ($<10\%$) Fe- ja FeMn-materjalidel. Sellest lähtudes kasutati Fe-N-MPC ja FeMn-N-MPC materjale kütuseelemendis, kus mõlemaga saavutati sarnane võimsustihedus $\sim 470 \text{ mW cm}^{-2}$.

Töö viiendas osas valmistati ise mesopoorne süsinikmaterjal (OMC), mida kasutati alusmaterjalina. OMC materjal oli kitsa pooride suuruse jaotusega, sisaldades peamiselt poore keskmise diameetriga 7 nm. Selleks, et uurida katalüsaatormaterjalide poorsuse mõju AEMFC tulemustele, kombineeriti OMC materjali CDC või CNT-ga. Kõik kolm alusmaterjali dopeeriti lämmastikuga (lähteaineks 1,10-fenantroliin), koobalti ja rauaga. Seega saadi järgnevad katalüsaatormaterjalid: mesopoorne CoFe-N-OMC, mikro- ja mesopoorne CoFe-N-OMC/CDC ning nii väiksemate (~ 7 nm) kui suuremate (15–40 nm) mesopooridega CoFe-N-OMC/CNT. RDE testides olid kõik kolm materjali sarnaselt kõrge hapniku elektroredutseerumise aktiivsusega. AEMFC tulemused aga näitasid, et seal on katalüsaatori poorsel struktuuril suurem mõju, sest CoFe-N-OMC/CNT materjal andis parema tulemuse kui teised kaks, millest võib järeldada, et kütuseelemendi katalüsaatorikihi omadusi parandavad suuremad mesopoorid.

Doktoritöös saadud tulemused aitavad selgitada katalüsaatorite poorse struktuuri ja materjalides sisalduvate siirdemetallide mõju nende elektrokatalüütilisele aktiivsusele hapniku redutseerimisel ning AEMFC jõudlusele, andes seeläbi olulise panuse mitteväärismetallkatalüsaatorite hapniku redutseerumise elektrokatalüüsi valdkonda.

10. ACKNOWLEDGEMENTS

My deepest gratitude goes to by supervisors, Dr. Ave Sarapuu, Dr. Elo Kibena-Pöldsepp and Professor Kaido Tammeveski for their invaluable assistance, scientific guidance and moral support throughout these years.

I would like to sincerely thank everyone in our working group who have provided me with advice, inspiration, or simply with kind words and encouragement. Special thanks to Dr. Heiki Erikson and Dr. Marek Mooste for all their technical assistance.

My gratitude goes out to the co-authors of the publications this thesis is based on: Dr. Arvo Kikas, Dr. Vambola Kisand, Dr. Maike Käärrik, Maida Merisalu, Dr. Alexey Treshchalov, Dr. Jaan Leis, Prof. Väino Sammelselg, Qiliang Wei, Mounika Kodali, Yechuan Chen, Dr. Tristan Asset, Dr. Päärn Paiste, Jaan Aruväli, Dr. Mihkel Rähn, Dr. Aile Tamm, Dr. Jekaterina Kozlova, Dr. Marek Mooste, John C. Douglin, Dr. Anastasiia Konovalova, Prof. Dario R. Dekel, Prof. Plamen Atanassov, and Prof. Steven Holdcroft.

Additionally, I would like to thank my friends and family for all their support and motivation. Special thank you goes to my mother, Juta Vaher, for all her hard work and support throughout my studies and life leading to it. Special gratitude also goes to Martin Lensment for his patience and limitless support even at most stressful times.

This work was financially supported by the EU through the European Regional Development Fund (TK141 “Advanced materials and high technology devices for energy recuperation systems”), by Estonian Research Council (grant PRG723), the Smart specialisation scholarship for Jaana Lilloja, and the Graduate School of Functional Materials and Technologies.

PUBLICATIONS

CURRICULUM VITAE

Name: Jaana Lilloja
Date of birth: August 20, 1994
Citizenship: Estonian (EST)
Address: Ravila 14a, 50411 Tartu, Estonia
Phone: +372 5903 5189
E-mail: jaana.lilloja@ut.ee

Education:

2018–... University of Tartu, PhD studies, Chemistry
2016–2018 Tallinn University of Technology, MSc.Eng (*cum laude*),
Technology of Wood, Plastics and Textiles
2013–2016 University of Tartu, BSc, Materials Science
2010–2013 Nõo Realgümnaasium, secondary education

Professional experience:

1.09.2020–... University of Tartu, Institute of Chemistry, chemist
1.09.2019–31.12.2019 University of Tartu, Institute of Chemistry, chemist

Major scientific publications:

1. **J. Lilloja**, E. Kibena-Põldsepp, M. Merisalu, P. Rauwel, L. Matisen, A. Niilisk, E.S.F. Cardoso, G. Maia, V. Sammelseg, K. Tammeveski, An Oxygen Reduction Study of Graphene-Based Nanomaterials of Different Origin, *Catalysts* 6 (2016) 108.
2. **J. Lilloja**, E. Kibena-Põldsepp, A. Sarapuu, A. Kikas, V. Kisand, M. Käärik, M. Merisalu, A. Treshchalov, J. Leis, V. Sammelseg, Q. Wei, S. Holdcroft, K. Tammeveski, Nitrogen-doped carbide-derived carbon/carbon nanotube composites as cathode catalysts for anion exchange membrane fuel cell application, *Applied Catalysis B: Environmental* 272 (2020) 119012
3. **J. Lilloja**, E. Kibena-Põldsepp, A. Sarapuu, M. Kodali, Y. Chen, T. Asset, M. Käärik, M. Merisalu, P. Paiste, J. Aruväli, A. Treshchalov, M. Rähn, J. Leis, V. Sammelseg, S. Holdcroft, P. Atanassov, K. Tammeveski, Cathode Catalysts Based on Cobalt- and Nitrogen-Doped Nanocarbon Composites for Anion Exchange Membrane Fuel Cells, *ACS Applied Energy Materials* 3 (2020) 5375–5384
4. I. Palm, E. Kibena-Põldsepp, **J. Lilloja**, M. Käärik, A. Kisand, M. Merisalu, A. Treshchalov, P. Paiste, J. Leis, A. Tamm, V. Sammelseg, K. Tammeveski, Impact of ball-milling of carbide-derived carbons on the generation of hydrogen peroxide via electroreduction of oxygen in alkaline media, *Journal of Electroanalytical Chemistry* 878 (2020) 114690.
5. **J. Lilloja**, E. Kibena-Põldsepp, A. Sarapuu, J.C. Douglin, M. Käärik, J. Kozlova, P. Paiste, A. Kikas, J. Aruväli, J. Leis, V. Sammelseg, D.R. Dekel, K. Tammeveski, Transition-Metal- and Nitrogen-Doped Carbide-Derived

- Carbon/Carbon Nanotube Composites as Cathode Catalysts for Anion-Exchange Membrane Fuel Cells, *ACS Catalysis* 11 (2021) 1920–1931.
6. **J. Lilloja**, M. Mooste, E. Kibena-Põldsepp, A. Sarapuu, B. Zulevi, A. Kikas, H.-M. Piirsoo, A. Tamm, V. Kisand, S. Holdcroft, A. Serov, K. Tammeveski, Mesoporous iron-nitrogen co-doped carbon material as cathode catalyst for the anion exchange membrane fuel cell, *Journal of Power Sources Advances* 8 (2021) 100052.
 7. **J. Lilloja**, E. Kibena-Põldsepp, A. Sarapuu, M. Käärrik, J. Kozlova, P. Paiste, A. Kikas, A. Treshchalov, J. Leis, A. Tamm, V. Kisand, S. Holdcroft, K. Tammeveski, Transition metal and nitrogen-doped mesoporous carbons as cathode catalysts for anion-exchange membrane fuel cells, *Applied Catalysis B: Environmental* 306 (2022) 121113.

ELULOOKIRJELDUS

Nimi: Jaana Lilloja
Sünniaeg: 20.08.1994
Kodakondsus: Eesti (EST)
Aadress: Ravila 14a, 50411 Tartu, Eesti
Kontakttelefon: +372 59035189
E-mail: jaana.lilloja@ut.ee

Hariduskäik:

2018–... Tartu Ülikool, doktoriõpingud, keemia
2016–2018 Tallinna Tehnikaülikool, tehnikateaduse magister (*cum laude*),
puidu- ja plastitehnoloogia
2013–2016 Tartu Ülikool, loodusteaduse bakalaureus, materjaliteadus
2010–2013 Nõo Reaalgümnaasium, keskharidus

Töökogemus:

1.09.2020–... Tartu Ülikool, Keemia instituut, keemik
1.09.2019–31.12.2019 Tartu Ülikool, Keemia instituut, keemik

Publikatsioonide loetelu:

1. **J. Lilloja**, E. Kibena-Pöldsepp, M. Merisalu, P. Rauwel, L. Matisen, A. Niilisk, E.S.F. Cardoso, G. Maia, V. Sammelselg, K. Tammeveski, An Oxygen Reduction Study of Graphene-Based Nanomaterials of Different Origin, *Catalysts* 6 (2016) 108.
2. **J. Lilloja**, E. Kibena-Pöldsepp, A. Sarapuu, A. Kikas, V. Kisand, M. Käärrik, M. Merisalu, A. Treshchalov, J. Leis, V. Sammelselg, Q. Wei, S. Holdcroft, K. Tammeveski, Nitrogen-doped carbide-derived carbon/carbon nanotube composites as cathode catalysts for anion exchange membrane fuel cell application, *Applied Catalysis B: Environmental* 272 (2020) 119012
3. **J. Lilloja**, E. Kibena-Pöldsepp, A. Sarapuu, M. Kodali, Y. Chen, T. Asset, M. Käärrik, M. Merisalu, P. Paiste, J. Aruväli, A. Treshchalov, M. Rähn, J. Leis, V. Sammelselg, S. Holdcroft, P. Atanassov, K. Tammeveski, Cathode Catalysts Based on Cobalt- and Nitrogen-Doped Nanocarbon Composites for Anion Exchange Membrane Fuel Cells, *ACS Applied Energy Materials* 3 (2020) 5375–5384
4. Palm, E. Kibena-Pöldsepp, **J. Lilloja**, M. Käärrik, A. Kisand, M. Merisalu, A. Treshchalov, P. Paiste, J. Leis, A. Tamm, V. Sammelselg, K. Tammeveski, Impact of ball-milling of carbide-derived carbons on the generation of hydrogen peroxide via electroreduction of oxygen in alkaline media, *Journal of Electroanalytical Chemistry* 878 (2020) 114690.
5. **J. Lilloja**, E. Kibena-Pöldsepp, A. Sarapuu, J.C. Douglin, M. Käärrik, J. Kozlova, P. Paiste, A. Kikas, J. Aruväli, J. Leis, V. Sammelselg, D.R. Dekel, K. Tammeveski, Transition-Metal- and Nitrogen-Doped Carbide-Derived

- Carbon/Carbon Nanotube Composites as Cathode Catalysts for Anion-Exchange Membrane Fuel Cells, *ACS Catalysis* 11 (2021) 1920–1931.
6. **J. Lilloja**, M. Mooste, E. Kibena-Põldsepp, A. Sarapuu, B. Zulevi, A. Kikas, H.-M. Piirsoo, A. Tamm, V. Kisand, S. Holdcroft, A. Serov, K. Tammeveski, Mesoporous iron-nitrogen co-doped carbon material as cathode catalyst for the anion exchange membrane fuel cell, *Journal of Power Sources Advances* 8 (2021) 100052.
 7. **J. Lilloja**, E. Kibena-Põldsepp, A. Sarapuu, M. Käärrik, J. Kozlova, P. Paiste, A. Kikas, A. Treshchalov, J. Leis, A. Tamm, V. Kisand, S. Holdcroft, K. Tammeveski, Transition metal and nitrogen-doped mesoporous carbons as cathode catalysts for anion-exchange membrane fuel cells, *Applied Catalysis B: Environmental* 306 (2022) 121113.

DISSERTATIONES CHIMICAE UNIVERSITATIS TARTUENSIS

1. **Toomas Tamm.** Quantum-chemical simulation of solvent effects. Tartu, 1993, 110 p.
2. **Peeter Burk.** Theoretical study of gas-phase acid-base equilibria. Tartu, 1994, 96 p.
3. **Victor Lobanov.** Quantitative structure-property relationships in large descriptor spaces. Tartu, 1995, 135 p.
4. **Vahur Mäemets.** The ^{17}O and ^1H nuclear magnetic resonance study of H_2O in individual solvents and its charged clusters in aqueous solutions of electrolytes. Tartu, 1997, 140 p.
5. **Andrus Metsala.** Microcanonical rate constant in nonequilibrium distribution of vibrational energy and in restricted intramolecular vibrational energy redistribution on the basis of slater's theory of unimolecular reactions. Tartu, 1997, 150 p.
6. **Uko Maran.** Quantum-mechanical study of potential energy surfaces in different environments. Tartu, 1997, 137 p.
7. **Alar Jänes.** Adsorption of organic compounds on antimony, bismuth and cadmium electrodes. Tartu, 1998, 219 p.
8. **Kaido Tammeveski.** Oxygen electroreduction on thin platinum films and the electrochemical detection of superoxide anion. Tartu, 1998, 139 p.
9. **Ivo Leito.** Studies of Brønsted acid-base equilibria in water and non-aqueous media. Tartu, 1998, 101 p.
10. **Jaan Leis.** Conformational dynamics and equilibria in amides. Tartu, 1998, 131 p.
11. **Toonika Rinke.** The modelling of amperometric biosensors based on oxidoreductases. Tartu, 2000, 108 p.
12. **Dmitri Panov.** Partially solvated Grignard reagents. Tartu, 2000, 64 p.
13. **Kaja Orupõld.** Treatment and analysis of phenolic wastewater with microorganisms. Tartu, 2000, 123 p.
14. **Jüri Ivask.** Ion Chromatographic determination of major anions and cations in polar ice core. Tartu, 2000, 85 p.
15. **Lauri Vares.** Stereoselective Synthesis of Tetrahydrofuran and Tetrahydropyran Derivatives by Use of Asymmetric Horner-Wadsworth-Emmons and Ring Closure Reactions. Tartu, 2000, 184 p.
16. **Martin Lepiku.** Kinetic aspects of dopamine D_2 receptor interactions with specific ligands. Tartu, 2000, 81 p.
17. **Katrin Sak.** Some aspects of ligand specificity of P2Y receptors. Tartu, 2000, 106 p.
18. **Vello Pällin.** The role of solvation in the formation of iotsitch complexes. Tartu, 2001, 95 p.
19. **Katrin Kollist.** Interactions between polycyclic aromatic compounds and humic substances. Tartu, 2001, 93 p.

20. **Ivar Koppel.** Quantum chemical study of acidity of strong and superstrong Brønsted acids. Tartu, 2001, 104 p.
21. **Viljar Pihl.** The study of the substituent and solvent effects on the acidity of OH and CH acids. Tartu, 2001, 132 p.
22. **Natalia Palm.** Specification of the minimum, sufficient and significant set of descriptors for general description of solvent effects. Tartu, 2001, 134 p.
23. **Sulev Sild.** QSPR/QSAR approaches for complex molecular systems. Tartu, 2001, 134 p.
24. **Ruslan Petrukhin.** Industrial applications of the quantitative structure-property relationships. Tartu, 2001, 162 p.
25. **Boris V. Rogovoy.** Synthesis of (benzotriazolyl)carboximidamides and their application in relations with *N*- and *S*-nucleophiles. Tartu, 2002, 84 p.
26. **Koit Herodes.** Solvent effects on UV-vis absorption spectra of some solvatochromic substances in binary solvent mixtures: the preferential solvation model. Tartu, 2002, 102 p.
27. **Anti Perkson.** Synthesis and characterisation of nanostructured carbon. Tartu, 2002, 152 p.
28. **Ivari Kaljurand.** Self-consistent acidity scales of neutral and cationic Brønsted acids in acetonitrile and tetrahydrofuran. Tartu, 2003, 108 p.
29. **Karmen Lust.** Adsorption of anions on bismuth single crystal electrodes. Tartu, 2003, 128 p.
30. **Mare Piirsalu.** Substituent, temperature and solvent effects on the alkaline hydrolysis of substituted phenyl and alkyl esters of benzoic acid. Tartu, 2003, 156 p.
31. **Meeri Sassian.** Reactions of partially solvated Grignard reagents. Tartu, 2003, 78 p.
32. **Tarmo Tamm.** Quantum chemical modelling of polypyrrole. Tartu, 2003. 100 p.
33. **Erik Teinmaa.** The environmental fate of the particulate matter and organic pollutants from an oil shale power plant. Tartu, 2003. 102 p.
34. **Jaana Tammiku-Taul.** Quantum chemical study of the properties of Grignard reagents. Tartu, 2003. 120 p.
35. **Andre Lomaka.** Biomedical applications of predictive computational chemistry. Tartu, 2003. 132 p.
36. **Kostyantyn Kirichenko.** Benzotriazole – Mediated Carbon–Carbon Bond Formation. Tartu, 2003. 132 p.
37. **Gunnar Nurk.** Adsorption kinetics of some organic compounds on bismuth single crystal electrodes. Tartu, 2003, 170 p.
38. **Mati Arulepp.** Electrochemical characteristics of porous carbon materials and electrical double layer capacitors. Tartu, 2003, 196 p.
39. **Dan Cornel Fara.** QSPR modeling of complexation and distribution of organic compounds. Tartu, 2004, 126 p.
40. **Riina Mahlapuu.** Signalling of galanin and amyloid precursor protein through adenylate cyclase. Tartu, 2004, 124 p.

41. **Mihkel Kerikmäe.** Some luminescent materials for dosimetric applications and physical research. Tartu, 2004, 143 p.
42. **Jaanus Kruusma.** Determination of some important trace metal ions in human blood. Tartu, 2004, 115 p.
43. **Urmas Johanson.** Investigations of the electrochemical properties of polypyrrole modified electrodes. Tartu, 2004, 91 p.
44. **Kaido Sillar.** Computational study of the acid sites in zeolite ZSM-5. Tartu, 2004, 80 p.
45. **Aldo Oras.** Kinetic aspects of dATP α S interaction with P2Y₁ receptor. Tartu, 2004, 75 p.
46. **Erik Mölder.** Measurement of the oxygen mass transfer through the air-water interface. Tartu, 2005, 73 p.
47. **Thomas Thomborg.** The kinetics of electroreduction of peroxodisulfate anion on cadmium (0001) single crystal electrode. Tartu, 2005, 95 p.
48. **Olavi Loog.** Aspects of condensations of carbonyl compounds and their imine analogues. Tartu, 2005, 83 p.
49. **Siim Salmar.** Effect of ultrasound on ester hydrolysis in aqueous ethanol. Tartu, 2006, 73 p.
50. **Ain Uustare.** Modulation of signal transduction of heptahelical receptors by other receptors and G proteins. Tartu, 2006, 121 p.
51. **Sergei Yurchenko.** Determination of some carcinogenic contaminants in food. Tartu, 2006, 143 p.
52. **Kaido Tämm.** QSPR modeling of some properties of organic compounds. Tartu, 2006, 67 p.
53. **Olga Tšubrik.** New methods in the synthesis of multisubstituted hydrazines. Tartu, 2006, 183 p.
54. **Lilli Sooväli.** Spectrophotometric measurements and their uncertainty in chemical analysis and dissociation constant measurements. Tartu, 2006, 125 p.
55. **Eve Koort.** Uncertainty estimation of potentiometrically measured pH and pK_a values. Tartu, 2006, 139 p.
56. **Sergei Kopanchuk.** Regulation of ligand binding to melanocortin receptor subtypes. Tartu, 2006, 119 p.
57. **Silvar Kallip.** Surface structure of some bismuth and antimony single crystal electrodes. Tartu, 2006, 107 p.
58. **Kristjan Saal.** Surface silanization and its application in biomolecule coupling. Tartu, 2006, 77 p.
59. **Tanel Tätte.** High viscosity Sn(OBu)₄ oligomeric concentrates and their applications in technology. Tartu, 2006, 91 p.
60. **Dimitar Atanasov Dobchev.** Robust QSAR methods for the prediction of properties from molecular structure. Tartu, 2006, 118 p.
61. **Hannes Hagu.** Impact of ultrasound on hydrophobic interactions in solutions. Tartu, 2007, 81 p.
62. **Rutha Jäger.** Electroreduction of peroxodisulfate anion on bismuth electrodes. Tartu, 2007, 142 p.

63. **Kaido Viht.** Immobilizable bisubstrate-analogue inhibitors of basophilic protein kinases: development and application in biosensors. Tartu, 2007, 88 p.
64. **Eva-Ingrid Rõõm.** Acid-base equilibria in nonpolar media. Tartu, 2007, 156 p.
65. **Sven Tamp.** DFT study of the cesium cation containing complexes relevant to the cesium cation binding by the humic acids. Tartu, 2007, 102 p.
66. **Jaak Nerut.** Electroreduction of hexacyanoferrate(III) anion on Cadmium (0001) single crystal electrode. Tartu, 2007, 180 p.
67. **Lauri Jalukse.** Measurement uncertainty estimation in amperometric dissolved oxygen concentration measurement. Tartu, 2007, 112 p.
68. **Aime Lust.** Charge state of dopants and ordered clusters formation in CaF₂:Mn and CaF₂:Eu luminophors. Tartu, 2007, 100 p.
69. **Iiris Kahn.** Quantitative Structure-Activity Relationships of environmentally relevant properties. Tartu, 2007, 98 p.
70. **Mari Reinik.** Nitrates, nitrites, N-nitrosamines and polycyclic aromatic hydrocarbons in food: analytical methods, occurrence and dietary intake. Tartu, 2007, 172 p.
71. **Heili Kasuk.** Thermodynamic parameters and adsorption kinetics of organic compounds forming the compact adsorption layer at Bi single crystal electrodes. Tartu, 2007, 212 p.
72. **Erki Enkvist.** Synthesis of adenosine-peptide conjugates for biological applications. Tartu, 2007, 114 p.
73. **Svetoslav Hristov Slavov.** Biomedical applications of the QSAR approach. Tartu, 2007, 146 p.
74. **Eneli Härk.** Electroreduction of complex cations on electrochemically polished Bi(*hkl*) single crystal electrodes. Tartu, 2008, 158 p.
75. **Priit Möller.** Electrochemical characteristics of some cathodes for medium temperature solid oxide fuel cells, synthesized by solid state reaction technique. Tartu, 2008, 90 p.
76. **Signe Viggor.** Impact of biochemical parameters of genetically different pseudomonads at the degradation of phenolic compounds. Tartu, 2008, 122 p.
77. **Ave Sarapuu.** Electrochemical reduction of oxygen on quinone-modified carbon electrodes and on thin films of platinum and gold. Tartu, 2008, 134 p.
78. **Agnes Kütt.** Studies of acid-base equilibria in non-aqueous media. Tartu, 2008, 198 p.
79. **Rouvim Kadis.** Evaluation of measurement uncertainty in analytical chemistry: related concepts and some points of misinterpretation. Tartu, 2008, 118 p.
80. **Valter Reedo.** Elaboration of IVB group metal oxide structures and their possible applications. Tartu, 2008, 98 p.
81. **Aleksei Kuznetsov.** Allosteric effects in reactions catalyzed by the cAMP-dependent protein kinase catalytic subunit. Tartu, 2009, 133 p.

82. **Aleksei Bredihhin.** Use of mono- and polyanions in the synthesis of multisubstituted hydrazine derivatives. Tartu, 2009, 105 p.
83. **Anu Ploom.** Quantitative structure-reactivity analysis in organosilicon chemistry. Tartu, 2009, 99 p.
84. **Argo Vonk.** Determination of adenosine A_{2A}- and dopamine D₁ receptor-specific modulation of adenylate cyclase activity in rat striatum. Tartu, 2009, 129 p.
85. **Indrek Kivi.** Synthesis and electrochemical characterization of porous cathode materials for intermediate temperature solid oxide fuel cells. Tartu, 2009, 177 p.
86. **Jaanus Eskusson.** Synthesis and characterisation of diamond-like carbon thin films prepared by pulsed laser deposition method. Tartu, 2009, 117 p.
87. **Marko Lätt.** Carbide derived microporous carbon and electrical double layer capacitors. Tartu, 2009, 107 p.
88. **Vladimir Stepanov.** Slow conformational changes in dopamine transporter interaction with its ligands. Tartu, 2009, 103 p.
89. **Aleksander Trummal.** Computational Study of Structural and Solvent Effects on Acidities of Some Brønsted Acids. Tartu, 2009, 103 p.
90. **Eerold Vellemäe.** Applications of mischmetal in organic synthesis. Tartu, 2009, 93 p.
91. **Sven Parkel.** Ligand binding to 5-HT_{1A} receptors and its regulation by Mg²⁺ and Mn²⁺. Tartu, 2010, 99 p.
92. **Signe Vahur.** Expanding the possibilities of ATR-FT-IR spectroscopy in determination of inorganic pigments. Tartu, 2010, 184 p.
93. **Tavo Romann.** Preparation and surface modification of bismuth thin film, porous, and microelectrodes. Tartu, 2010, 155 p.
94. **Nadežda Aleksejeva.** Electrocatalytic reduction of oxygen on carbon nanotube-based nanocomposite materials. Tartu, 2010, 147 p.
95. **Marko Kullapere.** Electrochemical properties of glassy carbon, nickel and gold electrodes modified with aryl groups. Tartu, 2010, 233 p.
96. **Liis Siinor.** Adsorption kinetics of ions at Bi single crystal planes from aqueous electrolyte solutions and room-temperature ionic liquids. Tartu, 2010, 101 p.
97. **Angela Vaasa.** Development of fluorescence-based kinetic and binding assays for characterization of protein kinases and their inhibitors. Tartu 2010, 101 p.
98. **Indrek Tulp.** Multivariate analysis of chemical and biological properties. Tartu 2010, 105 p.
99. **Aare Selberg.** Evaluation of environmental quality in Northern Estonia by the analysis of leachate. Tartu 2010, 117 p.
100. **Darja Lavõgina.** Development of protein kinase inhibitors based on adenosine analogue-oligoarginine conjugates. Tartu 2010, 248 p.
101. **Laura Herm.** Biochemistry of dopamine D₂ receptors and its association with motivated behaviour. Tartu 2010, 156 p.

102. **Terje Raudsepp.** Influence of dopant anions on the electrochemical properties of polypyrrole films. Tartu 2010, 112 p.
103. **Margus Marandi.** Electroformation of Polypyrrole Films: *In-situ* AFM and STM Study. Tartu 2011, 116 p.
104. **Kairi Kivirand.** Diamine oxidase-based biosensors: construction and working principles. Tartu, 2011, 140 p.
105. **Anneli Kruve.** Matrix effects in liquid-chromatography electrospray mass-spectrometry. Tartu, 2011, 156 p.
106. **Gary Urb.** Assessment of environmental impact of oil shale fly ash from PF and CFB combustion. Tartu, 2011, 108 p.
107. **Nikita Oskolkov.** A novel strategy for peptide-mediated cellular delivery and induction of endosomal escape. Tartu, 2011, 106 p.
108. **Dana Martin.** The QSPR/QSAR approach for the prediction of properties of fullerene derivatives. Tartu, 2011, 98 p.
109. **Säde Viirlaid.** Novel glutathione analogues and their antioxidant activity. Tartu, 2011, 106 p.
110. **Ülis Sõukand.** Simultaneous adsorption of Cd²⁺, Ni²⁺, and Pb²⁺ on peat. Tartu, 2011, 124 p.
111. **Lauri Lipping.** The acidity of strong and superstrong Brønsted acids, an outreach for the “limits of growth”: a quantum chemical study. Tartu, 2011, 124 p.
112. **Heisi Kurig.** Electrical double-layer capacitors based on ionic liquids as electrolytes. Tartu, 2011, 146 p.
113. **Marje Kasari.** Bisubstrate luminescent probes, optical sensors and affinity adsorbents for measurement of active protein kinases in biological samples. Tartu, 2012, 126 p.
114. **Kalev Takkis.** Virtual screening of chemical databases for bioactive molecules. Tartu, 2012, 122 p.
115. **Ksenija Kisseljova.** Synthesis of aza-β³-amino acid containing peptides and kinetic study of their phosphorylation by protein kinase A. Tartu, 2012, 104 p.
116. **Riin Rebane.** Advanced method development strategy for derivatization LC/ESI/MS. Tartu, 2012, 184 p.
117. **Vladislav Ivaništšev.** Double layer structure and adsorption kinetics of ions at metal electrodes in room temperature ionic liquids. Tartu, 2012, 128 p.
118. **Irja Helm.** High accuracy gravimetric Winkler method for determination of dissolved oxygen. Tartu, 2012, 139 p.
119. **Karin Kipper.** Fluoroalcohols as Components of LC-ESI-MS Eluents: Usage and Applications. Tartu, 2012, 164 p.
120. **Arno Ratas.** Energy storage and transfer in dosimetric luminescent materials. Tartu, 2012, 163 p.
121. **Reet Reinart-Okugbeni.** Assay systems for characterisation of subtype-selective binding and functional activity of ligands on dopamine receptors. Tartu, 2012, 159 p.

122. **Lauri Sikk.** Computational study of the Sonogashira cross-coupling reaction. Tartu, 2012, 81 p.
123. **Karita Raudkivi.** Neurochemical studies on inter-individual differences in affect-related behaviour of the laboratory rat. Tartu, 2012, 161 p.
124. **Indrek Saar.** Design of GalR2 subtype specific ligands: their role in depression-like behavior and feeding regulation. Tartu, 2013, 126 p.
125. **Ann Laheäär.** Electrochemical characterization of alkali metal salt based non-aqueous electrolytes for supercapacitors. Tartu, 2013, 127 p.
126. **Kerli Tõnurist.** Influence of electrospun separator materials properties on electrochemical performance of electrical double-layer capacitors. Tartu, 2013, 147 p.
127. **Kaija Põhako-Esko.** Novel organic and inorganic ionogels: preparation and characterization. Tartu, 2013, 124 p.
128. **Ivar Kruusenberg.** Electroreduction of oxygen on carbon nanomaterial-based catalysts. Tartu, 2013, 191 p.
129. **Sander Piiskop.** Kinetic effects of ultrasound in aqueous acetonitrile solutions. Tartu, 2013, 95 p.
130. **Ilona Faustova.** Regulatory role of L-type pyruvate kinase N-terminal domain. Tartu, 2013, 109 p.
131. **Kadi Tamm.** Synthesis and characterization of the micro-mesoporous anode materials and testing of the medium temperature solid oxide fuel cell single cells. Tartu, 2013, 138 p.
132. **Iva Bozhidarova Stoyanova-Slavova.** Validation of QSAR/QSPR for regulatory purposes. Tartu, 2013, 109 p.
133. **Vitali Grozovski.** Adsorption of organic molecules at single crystal electrodes studied by *in situ* STM method. Tartu, 2014, 146 p.
134. **Santa Veikšina.** Development of assay systems for characterisation of ligand binding properties to melanocortin 4 receptors. Tartu, 2014, 151 p.
135. **Jüri Liiv.** PVDF (polyvinylidene difluoride) as material for active element of twisting-ball displays. Tartu, 2014, 111 p.
136. **Kersti Vaarmets.** Electrochemical and physical characterization of pristine and activated molybdenum carbide-derived carbon electrodes for the oxygen electroreduction reaction. Tartu, 2014, 131 p.
137. **Lauri Tõntson.** Regulation of G-protein subtypes by receptors, guanine nucleotides and Mn²⁺. Tartu, 2014, 105 p.
138. **Aiko Adamson.** Properties of amine-boranes and phosphorus analogues in the gas phase. Tartu, 2014, 78 p.
139. **Elo Kibena.** Electrochemical grafting of glassy carbon, gold, highly oriented pyrolytic graphite and chemical vapour deposition-grown graphene electrodes by diazonium reduction method. Tartu, 2014, 184 p.
140. **Teemu Näykki.** Novel Tools for Water Quality Monitoring – From Field to Laboratory. Tartu, 2014, 202 p.
141. **Karl Kaupmees.** Acidity and basicity in non-aqueous media: importance of solvent properties and purity. Tartu, 2014, 128 p.

142. **Oleg Lebedev.** Hydrazine polyanions: different strategies in the synthesis of heterocycles. Tartu, 2015, 118 p.
143. **Geven Piir.** Environmental risk assessment of chemicals using QSAR methods. Tartu, 2015, 123 p.
144. **Olga Mazina.** Development and application of the biosensor assay for measurements of cyclic adenosine monophosphate in studies of G protein-coupled receptor signaling. Tartu, 2015, 116 p.
145. **Sandip Ashokrao Kadam.** Anion receptors: synthesis and accurate binding measurements. Tartu, 2015, 116 p.
146. **Indrek Tallo.** Synthesis and characterization of new micro-mesoporous carbide derived carbon materials for high energy and power density electrical double layer capacitors. Tartu, 2015, 148 p.
147. **Heiki Erikson.** Electrochemical reduction of oxygen on nanostructured palladium and gold catalysts. Tartu, 2015, 204 p.
148. **Erik Anderson.** *In situ* Scanning Tunnelling Microscopy studies of the interfacial structure between Bi(111) electrode and a room temperature ionic liquid. Tartu, 2015, 118 p.
149. **Girinath G. Pillai.** Computational Modelling of Diverse Chemical, Biochemical and Biomedical Properties. Tartu, 2015, 140 p.
150. **Piret Pikma.** Interfacial structure and adsorption of organic compounds at Cd(0001) and Sb(111) electrodes from ionic liquid and aqueous electrolytes: an *in situ* STM study. Tartu, 2015, 126 p.
151. **Ganesh babu Manoharan.** Combining chemical and genetic approaches for photoluminescence assays of protein kinases. Tartu, 2016, 126 p.
152. **Carolin Siimenson.** Electrochemical characterization of halide ion adsorption from liquid mixtures at Bi(111) and pyrolytic graphite electrode surface. Tartu, 2016, 110 p.
153. **Asko Laaniste.** Comparison and optimisation of novel mass spectrometry ionisation sources. Tartu, 2016, 156 p.
154. **Hanno Evard.** Estimating limit of detection for mass spectrometric analysis methods. Tartu, 2016, 224 p.
155. **Kadri Ligi.** Characterization and application of protein kinase-responsive organic probes with triplet-singlet energy transfer. Tartu, 2016, 122 p.
156. **Margarita Kagan.** Biosensing penicillins' residues in milk flows. Tartu, 2016, 130 p.
157. **Marie Kriisa.** Development of protein kinase-responsive photoluminescent probes and cellular regulators of protein phosphorylation. Tartu, 2016, 106 p.
158. **Mihkel Vestli.** Ultrasonic spray pyrolysis deposited electrolyte layers for intermediate temperature solid oxide fuel cells. Tartu, 2016, 156 p.
159. **Silver Sepp.** Influence of porosity of the carbide-derived carbon on the properties of the composite electrocatalysts and characteristics of polymer electrolyte fuel cells. Tartu, 2016, 137 p.
160. **Kristjan Haav.** Quantitative relative equilibrium constant measurements in supramolecular chemistry. Tartu, 2017, 158 p.

161. **Anu Teearu.** Development of MALDI-FT-ICR-MS methodology for the analysis of resinous materials. Tartu, 2017, 205 p.
162. **Taavi Ivan.** Bifunctional inhibitors and photoluminescent probes for studies on protein complexes. Tartu, 2017, 140 p.
163. **Maarja-Liisa Oldekop.** Characterization of amino acid derivatization reagents for LC-MS analysis. Tartu, 2017, 147 p.
164. **Kristel Jukk.** Electrochemical reduction of oxygen on platinum- and palladium-based nanocatalysts. Tartu, 2017, 250 p.
165. **Siim Kukk.** Kinetic aspects of interaction between dopamine transporter and *N*-substituted nortropine derivatives. Tartu, 2017, 107 p.
166. **Birgit Viira.** Design and modelling in early drug development in targeting HIV-1 reverse transcriptase and Malaria. Tartu, 2017, 172 p.
167. **Rait Kivi.** Allostery in cAMP dependent protein kinase catalytic subunit. Tartu, 2017, 115 p.
168. **Agnes Heering.** Experimental realization and applications of the unified acidity scale. Tartu, 2017, 123 p.
169. **Delia Juronen.** Biosensing system for the rapid multiplex detection of mastitis-causing pathogens in milk. Tartu, 2018, 85 p.
170. **Hedi Rahnel.** ARC-inhibitors: from reliable biochemical assays to regulators of physiology of cells. Tartu, 2018, 176 p.
171. **Anton Ruzanov.** Computational investigation of the electrical double layer at metal–aqueous solution and metal–ionic liquid interfaces. Tartu, 2018, 129 p.
172. **Katrin Kestav.** Crystal Structure-Guided Development of Bisubstrate-Analogue Inhibitors of Mitotic Protein Kinase Haspin. Tartu, 2018, 166 p.
173. **Mihkel Ilisson.** Synthesis of novel heterocyclic hydrazine derivatives and their conjugates. Tartu, 2018, 101 p.
174. **Anni Allikalt.** Development of assay systems for studying ligand binding to dopamine receptors. Tartu, 2018, 160 p.
175. **Ove Oil.** Electrical double layer structure and energy storage characteristics of ionic liquid based capacitors. Tartu, 2018, 187 p.
176. **Rasmus Palm.** Carbon materials for energy storage applications. Tartu, 2018, 114 p.
177. **Jürgen Metsik.** Preparation and stability of poly(3,4-ethylenedioxythiophene) thin films for transparent electrode applications. Tartu, 2018, 111 p.
178. **Sofja Tšepelevitš.** Experimental studies and modeling of solute-solvent interactions. Tartu, 2018, 109 p.
179. **Märt Lõkov.** Basicity of some nitrogen, phosphorus and carbon bases in acetonitrile. Tartu, 2018, 104 p.
180. **Anton Mastitski.** Preparation of α -aza-amino acid precursors and related compounds by novel methods of reductive one-pot alkylation and direct alkylation. Tartu, 2018, 155 p.
181. **Jürgen Vahter.** Development of bisubstrate inhibitors for protein kinase CK2. Tartu, 2019, 186 p.

182. **Piia Liigand.** Expanding and improving methodology and applications of ionization efficiency measurements. Tartu, 2019, 189 p.
183. **Sigrid Selberg.** Synthesis and properties of lipophilic phosphazene-based indicator molecules. Tartu, 2019, 74 p.
184. **Jaanus Liigand.** Standard substance free quantification for LC/ESI/MS analysis based on the predicted ionization efficiencies. Tartu, 2019, 254 p.
185. **Marek Mooste.** Surface and electrochemical characterisation of aryl film and nanocomposite material modified carbon and metal-based electrodes. Tartu, 2019, 304 p.
186. **Mare Oja.** Experimental investigation and modelling of pH profiles for effective membrane permeability of drug substances. Tartu, 2019, 306 p.
187. **Sajid Hussain.** Electrochemical reduction of oxygen on supported Pt catalysts. Tartu, 2019, 220 p.
188. **Ronald Väli.** Glucose-derived hard carbon electrode materials for sodium-ion batteries. Tartu, 2019, 180 p.
189. **Ester Tee.** Analysis and development of selective synthesis methods of hierarchical micro- and mesoporous carbons. Tartu, 2019, 210 p.
190. **Martin Maide.** Influence of the microstructure and chemical composition of the fuel electrode on the electrochemical performance of reversible solid oxide fuel cell. Tartu, 2020, 144 p.
191. **Edith Viirlaid.** Biosensing Pesticides in Water Samples. Tartu, 2020, 102 p.
192. **Maike Käärrik.** Nanoporous carbon: the controlled nanostructure, and structure-property relationships. Tartu, 2020, 162 p.
193. **Artur Gornischeff.** Study of ionization efficiencies for derivatized compounds in LC/ESI/MS and their application for targeted analysis. Tartu, 2020, 124 p.
194. **Reet Link.** Ligand binding, allosteric modulation and constitutive activity of melanocortin-4 receptors. Tartu, 2020, 108 p.
195. **Pilleriin Peets.** Development of instrumental methods for the analysis of textile fibres and dyes. Tartu, 2020, 150 p.
196. **Larisa Ivanova.** Design of active compounds against neurodegenerative diseases. Tartu, 2020, 152 p.
197. **Meelis Härmas.** Impact of activated carbon microstructure and porosity on electrochemical performance of electrical double-layer capacitors. Tartu, 2020, 122 p.
198. **Ruta Hecht.** Novel Eluent Additives for LC-MS Based Bioanalytical Methods. Tartu, 2020, 202 p.
199. **Max Hecht.** Advances in the Development of a Point-of-Care Mass Spectrometer Test. Tartu, 2020, 168 p.
200. **Ida Rahu.** Bromine formation in inorganic bromide/nitrate mixtures and its application for oxidative aromatic bromination. Tartu, 2020, 116 p.
201. **Sander Ratso.** Electrocatalysis of oxygen reduction on non-precious metal catalysts. Tartu, 2020, 371 p.
202. **Astrid Darnell.** Computational design of anion receptors and evaluation of host-guest binding. Tartu, 2021, 150 p.

203. **Ove Korjus.** The development of ceramic fuel electrode for solid oxide cells. Tartu, 2021, 150 p.
204. **Merit Oss.** Ionization efficiency in electrospray ionization source and its relations to compounds' physico-chemical properties. Tartu, 2021, 124 p.
205. **Madis Lüsi.** Electroreduction of oxygen on nanostructured palladium catalysts. Tartu, 2021, 180 p.
206. **Eliise Tammekivi.** Derivatization and quantitative gas-chromatographic analysis of oils. Tartu, 2021, 122 p.
207. **Simona Selberg.** Development of Small-Molecule Regulators of Epi-transcriptomic Processes. Tartu, 2021, 122 p.
208. **Olivier Etebe Nonga.** Inhibitors and photoluminescent probes for in vitro studies on protein kinases PKA and PIM. Tartu, 2021, 189 p.
209. **Riinu Härmas.** The structure and H₂ diffusion in porous carbide-derived carbon particles. Tartu, 2022, 123 p.
210. **Maarja Paalo.** Synthesis and characterization of novel carbon electrodes for high power density electrochemical capacitors. Tartu, 2022, 144 p.
211. **Jinfeng Zhao.** Electrochemical characteristics of Bi(hkl) and micro-mesoporous carbon electrodes in ionic liquid based electrolytes. Tartu, 2022, 134 p.
212. **Alar Heinsaar.** Investigation of oxygen electrode materials for high-temperature solid oxide cells in natural conditions. Tartu, 2022, 120 p.